CHARACTERIZATION AND MODELING OF IN SITU STRESS HETEROGENEITY

A DISSERTATION
SUBMITTED TO THE DEPARTMENT OF GEOPHYSICS
AND THE COMMITTEE ON GRADUATE STUDIES
OF STANFORD UNIVERSITY
IN PARTIAL FULFILLMENT OF THE REQUIREMENTS
FOR THE DEGREE OF
DOCTOR OF PHILOSOPHY

Amy D. F. Day-Lewis

December 2007

I certify that I have read this dissertation and that, in my opinion, it is fully adequate in scope and quality as dissertation for the degree of Doctor of Philosophy.

_____
(Mark D. Zoback) Principal Adviser

I certify that I have read this dissertation and that, in my opinion, it is fully adequate in scope and quality as dissertation for the degree of Doctor of Philosophy.

_____
(Gregory Beroza)

I certify that I have read this dissertation and that, in my opinion, it is fully adequate in scope and quality as dissertation for the degree of Doctor of Philosophy.

_____
(Stephen Hickman)

I certify that I have read this dissertation and that, in my opinion, it is fully adequate in scope and quality as dissertation for the degree of Doctor of Philosophy.

_____
(Norman Sleep)

Approved for the University Committee on Graduate Studies.

ABSTRACT

Through a series of related projects, the work described in this dissertation strives to better constrain, describe, and explain in situ stress heterogeneity. Although each project has specific goals, approaches, and outcomes, combined they represent important progress in the ongoing effort to understand stress heterogeneity at a variety of scales.

In the first study we analyze multi-scale variations in the direction of maximum horizontal compressive stress as a function of depth in four scientific research boreholes located in a variety of tectonic environments. Our results provide insight into the mechanisms controlling in situ crustal stress heterogeneity over scales from centimeters to kilometers. We show that the orientation of the maximum, horizontal compressive stress determined from stress-induced wellbore failures displays scale-invariant, fractal distributions with spectral exponents between 1 and 2. The scaling of the stress variations is remarkably similar to the spatial scaling of earthquakes as a function of fault size in the individual study areas. Consequently, we suggest that wellbore stress heterogeneity is controlled by slip on a fractal distribution of active faults in the surrounding crust. The observed correlation between the scaling of stress heterogeneity and local fault behavior may prove useful in models of dynamic earthquake rupture, where many of the key parameters including stress and fault strength appear to vary spatially.

In the second study we develop two models—a two-dimensional, analytical model and a three-dimensional, numerical model—to explain the rotation of in situ stresses resulting from a pore pressure change on one side of an impermeable boundary (for example, near an impermeable fault in a depleted reservoir). Our models show clearly that near the boundary depletion will induce the maximum horizontal compressive stress to become more parallel to the boundary, whereas injection will have the opposite effect. We find a strong interaction between in situ stress magnitudes, rock property contrasts, reservoir shape, and boundary orientations. While the analytical model provides a good match to the field observations, the numerical model shows that for certain ratios of pore pressure change to differential horizontal stress, the analytical model may overpredict the amount of expected stress rotation. Our results can help forecast changes in stress directions throughout the life of a reservoir, which is critical for practices such as hydraulic fracturing. Our work will have important implications for the frictional stability of faults and fractures both in and around the reservoir.

In the final study we utilize data from twenty-one borehole tensor strainmeters recently deployed as part of the NSF EarthScope Plate Boundary Observatory to show that relatively large-magnitude, long-term strain trends in the data result at least in part from poroelastic deformation driven by the wellbore stress concentration. Our results allow us to derive a model-based approach for removing the trends, offering a significant improvement over the traditional approach that uses mathematical regression on each gauge individually. In addition, from the long-term strain accumulation we can derive information about the physical properties of the rock surrounding the strainmeter as well as the local in situ stress state, which can be compared to independent stress indicators such as earthquake focal mechanisms and stress-induced wellbore failures nearby. In a general sense, this work provides insight into time-dependent borehole deformation that will have implications not only for the strainmeter community but also in wellbore engineering and other scientific applications.

ACKNOWLEDGMENTS

I have to start my acknowledgments by thanking my biggest fan. Nikko, your unwavering faith in me, your unconditional love, your devotion so deep that it borders on worship—they kept me going when things got rough. You were by my side constantly, always ready to distract me from my troubles with a walk or a game. But although you can be silly at times, your insistence on a strict regimen of diet and exercise set an important example of discipline. Out of everyone in our household, you no doubt suffered the most from my frequent absences. I'm really, really sorry I had to put you in the kennel so often. You'll get extra cookies when I get home this time, ok? I promise. And a belly rub.

Now on to those special people from my own species. Fred's faith, love, dedication, and support come in a very close second to Nikko's (and thankfully he can walk and feed himself even when I'm not home). Honestly, there is absolutely no way I could have succeeded at this without him. He disagrees, but I know it's true. I want to thank my sister, Pam, for paving the way for the first generation in our family to attend college. And I have my brother, Greg, to thank for convincing me (when I was a freshman advertising major), to take a geology course. Little did either of us know I'd still be studying rocks 18 years later. To Talley Kenyon and Art DeVault I extend my love and deepest thanks for providing a true home away from home. Finally, there are too many friends to thank for their support and for letting me crash on their couches and guest beds, but I want to single out Steve Gorelick for always looking out for me. I feel very fortunate to be able to say that I also consider my advisor and every member of my research group friends as well as colleagues, and I can't thank them enough for making me feel welcome and at home from the first time I walked into the office.

I certainly didn't take the fastest or most direct route to my Ph.D., and much of that had to do with a lack of confidence. I can remember the exact moment when I thought for the very first time that I could actually get here, and that was when my advisor, Mark Zoback, suggested I return to Stanford to work with him. That's not to say I didn't experience all the usual stress and anxiety that go along with graduate school, but something fundamental changed in my perception of myself that day, and I'll always be grateful. I also wish to thank all of the faculty in the Department of Geophysics for allowing me to come back and prove to everyone, but most of all myself, what I was capable of.

CONTENTS

LIST OF FIGURES AND TABLES

Chapter 2

Chapter 3

Chapter 4

CHAPTER 1. INTRODUCTION

More than a quarter century of in situ stress measurements confirm that tectonic stresses display consistency in orientation and relative magnitude over broad regions of the Earth's crust, reflecting large-scale tectonic processes and forces associated with plate movements and lithospheric buoyancy (Zoback and Zoback, 1980; Zoback et al., 1989; Zoback, 1992). At smaller scales, however, variations from these regional patterns are very common.

The work presented in this thesis represents an attempt to quantify some of the characteristics of and controlling mechanisms behind in situ stress heterogeneity. The three-part premise that has guided this research is:

- In situ stress heterogeneity is a ubiquitous, important characteristic of the lithospheric stress field at a wide range of scales,
- A better understanding of stress heterogeneity at smaller scales can provide insight into the mechanics of larger-scale processes at work in the earth's crust, and
- Stress heterogeneity must be considered in the analysis and interpretation of many types of geophysical data.

Chapters 2 through 4 present the results of three separate projects, each borne out of a combination of curiosity, data availability, and feasibility. Individually they provide important answers to some specific questions: Can we quantify stress heterogeneity, and what might that tell us? How do pore pressure changes in reservoirs affect in situ stresses both inside and outside the reservoir? Can we measure small-magnitude stress changes in the near-surface using sensitive borehole strainmeters? Together they provide a body of knowledge that will help us better understand stress heterogeneity in general.

1.1 Characterizing and Modeling Wellbore Stress Rotations

Analysis of stress-induced wellbore failure has become one of the most important and accurate ways to measure in situ stresses in small crustal volumes. In a great many cases, stress orientations in a single borehole will follow a well-defined mean azimuth, and it is this mean direction that is of primary interest to geologists and engineers. But ubiquitous small-scale variations in stress directions also contain important information, and this is our focus in Chapter 2. The data in our study come from four scientific drilling sites in different tectonic settings. We carefully determine the scaling characteristics of stress orientations using both

traditional and innovative spectral analysis techniques, then we compare our results to the scaling of both physical property heterogeneity and seismicity at each location.

The results of this work were presented in various, partially completed forms at the 2005 National EarthScope Meeting (Albuquerque, NM), the 2005 Fall Meeting of the American Geophysical Union (San Francisco, CA), the 2005 and 2006 Stanford Rock and Borehole Geophysics Meetings (Menlo Park, CA), the 2006 Stanford School of Earth Sciences Annual Research Review (Stanford, CA), and the 2006 Annual Discussion Meeting of the British Geophysical Association (London, UK).

1.2 Understanding the Effects of Pore Pressure Changes on Stress in and around Reservoirs

Observed and reported changes in pore pressure and in situ stress in hydrocarbon reservoirs include apparent changes in stress magnitudes and orientations, fault activity, and faulting regime. The effects of pore pressure reduction are also a serious concern in oil fields where stress changes can have important implications for hydrocarbon extraction in terms of both wellbore stability and recovery operations such as hydrofracturing and water or steam flooding.

While the effects of pore pressure changes on stress magnitudes are fairly well understood, little is known about the response of stress orientations. In Chapter 3 we derive an analytical solution for the stress response to pore pressure change on one side of an impermeable boundary. We then develop a three-dimensional numerical model to examine this so-called stress-depletion response in greater detail, allowing us to determine the effects of various reservoir shapes and physical properties. Upon applying both models to case studies in the North Sea and Gulf of Mexico, we find that the simple analytical model is accurate for some cases, but for certain ratios of pore pressure change to differential horizontal stress it may overpredict the amount of expected stress rotation.

The analytical portion of this work was presented at the 2006 Stanford Rock and Borehole Geophysics Meeting (Menlo Park, CA) and the 2007 American Association of Petroleum Geologists Annual Technical Conference and Exhibition (Long Beach, CA).

1.3 Interpreting Measurements of Wellbore Strain

As scientists develop new and more accurate methods for measuring deformation in the shallow crust, we continue to find ways in which in situ stresses affect these measurements,

adding to our understanding of the role of stress in tectonic processes. Chapter 4 explores the effect of in situ stress on relatively shallow wells in which borehole tensor strainmeters are being installed as part of the NSF EarthScope Plate Boundary Observatory. In particular, it explains how the poroelastic response of the borehole to drilling is, at least in some cases, responsible for the relatively large-magnitude, long-term trends observed in the borehole strain data. While in the past these trends have been qualitatively attributed to grout curing and "borehole relaxation," until now no quantitative, physical explanation for them has been offered. Proper understanding of these trends not only improves data interpretation, but also reveals important information about the rock physical properties and surrounding in situ stress state.

This work was presented at the 2007 Seismological Association of America Annual Meeting (Waikoloa, HI) and the 2007 Stanford Rock and Borehole Geophysics Meeting (Menlo Park, CA), as well as at a special workshop in 2007 organized by the EarthScope Plate Boundary Observatory borehole strainmeter group (Gallatin Gateway, MT).

1.4 Summary and Final Notes

All of the work described in this thesis strives to better constrain, describe, and explain in situ stress heterogeneity. Although each project has specific goals, approaches, and outcomes, combined they represent important progress in the ongoing effort to understand stress heterogeneity at a variety of scales.

The benefits of this research should find application in numerous fields, from geotechnical (e.g., mining and excavation, nuclear waste repository planning, hydroelectric plant design, and geothermal field engineering) and petroleum engineering to earthquake hazards. In particular, the results will have implications for a wide range of topics in geophysics, engineering, and geostatistics including, but not limited to:

- estimating, mapping, and predicting in situ stress, even where measurements are sparse
- designing and implementing stress measurement efforts
- utilizing highly variable stress data
- comparing stresses between areas
- identifying stress change mechanisms
- enabling more rigorous stress modeling
- utilizing stress data in energy exploration and production

1.5 References

Zoback, M. L. (1992), First- and second-order patterns of stress in the lithosphere: The World Stress Map project, *J. Geophys. Res., B, 97*, 11703–11728.

Zoback, M. L., and M. D. Zoback (1980), State of stress in the conterminous United States, *J. Geophys. Res., B, 85*, 6113–6156.

Zoback, M. L., M. D. Zoback, J. Adams, M. Assumpção, S. Bell, E. A. Bergman, P. Blümling, N. R. Brereton, D. Denham, J. Ding, K. Fuchs, N. Gay, S. Gregersen, H. K. Gupta, A. Gvishiani, K. Jacob, R. Klein, P. Knoll, M. Magee, J. L. Mercier, B. Müller, C. Paquin, K. Rajendran, O. Stephansson, G. Suarez, M. Suter, A. Udias, Z. H. Xu, and M. Zhizhin (1989), Global patterns of tectonic stress, *Nature, 341*, 291–298.

CHAPTER 2. SCALE-INVARIANT STRESS ORIENTATIONS IN MULTIPLE TECTONIC ENVIRONMENTS

2.1 Abstract

We analyze multi-scale variations in the direction of maximum horizontal compressive stress (S_{Hmax}) as a function of depth in four scientific research boreholes in order to investigate the mechanisms controlling in situ crustal stress heterogeneity. The wells studied represent different tectonic environments including a plate-bounding transform fault (the San Andreas fault in California) and stable craton (the Baltic Shield). We find that in all of the wells the orientation of the maximum, horizontal compressive stress determined from stress-induced wellbore failures displays scale-invariant, fractal distributions with spectral exponents between 1 and 2. The stress scaling differs significantly from the scaling of physical property heterogeneity as measured in well logs, which has a spectral exponent of approximately 1. The stress variations are, however, remarkably similar to the spatial scaling of earthquakes as a function of fault size in the study areas. Consequently, we suggest that wellbore stress heterogeneity over the range of scales examined is controlled by slip on a fractal distribution of active faults in the surrounding crust.

2.2 Introduction

Heterogeneous in situ stress orientations in a single region are commonly observed in both natural (e.g., Abers and Gephart, 2001; Castillo and Zoback, 1995) and induced (e.g., Cornet et al., 2007) earthquake data. Likewise, stresses measured within wells frequently reveal multi-scale variations in the direction of maximum horizontal compressive stress (S_{Hmax}) as a function of depth (e.g., Barton and Zoback, 1994; Brudy et. al., 1997; Mariucci et al., 2002; Shamir and Zoback, 1992). Similar variations are observed in many deep wellbores and, in most cases, reflect relatively small, local changes in the directions and/or magnitudes of the in situ principal stresses superimposed on a more uniform regional stress state. Despite its pervasiveness and bearing on applications from hydrocarbon recovery to fault mechanics, multi-scale wellbore stress heterogeneity is generally treated as noise, and its properties have not been well explored.

In this study we employ a statistical approach towards quantifying stress orientation variability in four scientific boreholes representing a variety of tectonic environments. We find that, like many other geophysical phenomena (e.g., Barton and La Pointe, 1995; Mandelbrot, 1967; Turcotte, 1997), the heterogeneity is fractal in nature. This information then guides us in trying to better understand the causes and significance of wellbore stress heterogeneity in general.

In their analysis of well log data from the KTB borehole in Germany, Leonardi and Kümpel (1998) concluded that "…small-scale heterogeneities in the Earth's crust, at least down to 9 km, cannot be ignored by means of a simple scale reduction. Fractal geometry and $1/f$ noise, instead, offer practical ways to more adequately model crustal heterogeneities." Under this paradigm, the goal of this study is to use scaling properties to help determine both relationships between processes and mechanisms behind observed phenomena.

2.2.1 Stress Measurement in Wells

As described in detail by Zoback et al. (2003), wellbores may fail in either tension or compression as a result of the stress concentration at the wellbore wall. This stress concentration is a function of the in situ stress state, drilling parameters such as drilling fluid density, and the orientation of the well with respect to the in situ stress tensor. For over two decades observations of stress-induced wellbore failures have been used extensively in both industry and academia to constrain in situ stress directions and magnitudes in the upper crust. In the oil and gas industry characterization of stress from wellbore failures has become an important tool throughout the life of a reservoir. Advancement of failure analysis techniques from using spring-loaded caliper tools (Jarosinski, 1998; Plumb and Hickman, 1985) to high-resolution wellbore imaging (Brudy and Zoback, 1999; Peška and Zoback, 1995; Zoback et al., 1985) has greatly increased the resolution at which we can detect failures and the detail with which we can characterize them. In thousands of wells worldwide, mean stress directions determined using these techniques agree with independent stress indicators such as earthquake focal mechanisms and young geologic data (Zoback et al., 1989).

In a well in which the borehole axis is in line with one of the principal in situ stresses, compressive wellbore failures, if they form, will occur on opposite sides of the wellbore, parallel to the direction of the minimum stress acting in the plane of the wellbore cross-section. If tensile failures form, they will be parallel to the maximum stress. Where a well is inclined to the principal stress state, the occurrence and locations of failures are more

complicated but still inform us about stress directions and magnitudes (Peška and Zoback, 1995). In the majority of cases, detailed stress measurements from a single well are used to find a mean stress state representing some region around the well. Variations in stress orientations and magnitudes are generally averaged out, unless they are significantly large and/or their cause is of particular interest (e.g., Barton and Zoback, 1994; Shamir and Zoback, 1992).

2.2.2 Causes of Stress Perturbations

On intermediate scales (that is, between tectonic and wellbore) stress directions are clearly influenced by such mechanisms as lithology, geologic structure, and topography (e.g., Martin and Chandler, 1993; Tingay et al., 2003). Variability of stress directions in a single well has in several cases been attributed to shear fractures intersecting the well, perturbing both the magnitude and the orientation of the wellbore stresses. Shamir and Zoback (1992) introduced a model based on dislocation theory by Okada (1992) to explain several types of wellbore failure heterogeneity in the Cajon Pass scientific wellbore in southern California. These included gradual rotations, changes in compressive failure width, discontinuous orientation shifts, and the intermittent cessation of failure. In the model, fault slip creates a local, induced stress field which when superimposed onto the more uniform, in situ stress field causes the wellbore stress concentration to change. The fracture is a planar dislocation in a semi-infinite, isotropic, linearly elastic medium, and the maximum shear stress resolved on the fracture plane by the remote stress field determines the slip vector. The resulting perturbation to the wellbore stress depends on the borehole and remote stress orientations, the depth at which the fault intersects the wellbore, fault size and orientation, and stress drop. In general the modeled stress orientation perturbation extends along an interval of the well approximately two times the length of the fault, and the stress magnitude perturbation extends for about twice that (Zoback and Healy, 1992). The model has some notable weaknesses including non-uniqueness in some combinations of model parameters, a fixed slip vector, and a restriction that the wellbore–fault intersection must be somewhere near the middle of the fault in order to avoid the influence of singularities at the fault edges. Nevertheless, the model can successfully reproduce observed wellbore failure heterogeneity in several locations around the world including Cajon Pass and the KTB well in Germany (Barton and Zoback, 1994), thus demonstrating that slip on faults does have an appreciable, measurable effect on wellbore stress.

2.3 Data Sets

The data examined in this study come from four deep boreholes drilled for scientific purposes. The advantage of this is that each is well-documented, the data are for the most part readily available, and many complementary studies have been done on data from each location.

2.3.1 Cajon Pass

The Cajon Pass borehole was the first scientific wellbore drilled in order to assess the strength of the San Andreas fault by measuring stress and heat flow at depth in proximity to the fault trace. It is located 4 km northeast of the fault, near San Bernadino, California, close to the southernmost extent of the last great earthquake rupture on that part of the fault (a magnitude 7.9 in 1857). The borehole was drilled vertically in granite to a depth of 3460 m. Both wellbore failure (Shamir and Zoback, 1992) and natural fractures (Barton and Zoback, 1992; Leary, 1991) were analyzed in detail using wellbore image data collected over the interval 503 m to 3460 m. Compressive failures were studied in detail below 1750 m, providing detailed stress orientations measured at a 4 cm spacing. Careful analysis showed no obvious correlation between wellbore failure azimuths and either lithology, slight changes in borehole orientation, or rate of penetration during drilling. Multiple logging runs over the same intervals confirm the observed failure orientations at multiple depths. The resulting mean S_{Hmax} azimuth is around 50°, which is rotated clockwise with respect to the regional north-northwest trend determined using both seismic anisotropy and earthquake focal mechanisms (Liu et al., 1997). It is hypothesized that this might be due to slip on the nearby Cleghorn Fault (Shamir and Zoback, 1992) and/or the presence of a local stress state that is different from the deeper stress state driving the San Andreas fault (Liu et al., 1991; Townend and Zoback, 2004). As described in Section 2.2.2, multi-scale stress orientation perturbations are superimposed on the mean in situ stress direction for the well, and several of these can be explained by slip on faults intersecting the well.

2.3.2 SAFOD Pilot Hole

The San Andreas Fault Observatory at Depth (SAFOD) consists of a pilot hole and a main hole drilled, like Cajon Pass, in order to study the San Andreas fault. Significantly deeper than Cajon Pass, SAFOD provides access to the fault at seismogenic depths, allowing for sampling of fault materials and long-term monitoring of fault behavior. The boreholes are

located approximately 1 km southwest of the San Andreas surface trace in Parkfield, California. They are at the southern end of a segment of the fault that is creeping at a rate of 35 to 50 mm per year and is characterized by numerous small earthquakes (Murray and Segall, 2005; Wyss et al., 2004). The pilot hole was drilled vertically to 2200 m depth in granite (see Hickman et al., 2004 and references therein). The main hole was drilled vertically through granite and sedimentary rocks to a depth of about 3000 m and then deviated approximately 50° to the northeast in order to penetrate the fault at depth.

Detailed analysis of stress-induced failure has been performed on high-quality electrical and acoustic image data collected in the SAFOD pilot hole (Hickman and Zoback, 2004), revealing a stress state that is transitional strike-slip to reverse. Similar to Cajon Pass, several types of stress heterogeneity were observed: 1) an overall ~25º clockwise rotation from 800 meters to 2200 meters depth, creating an increasing angle between S_{Hmax} and the local strike of the San Andreas fault, 2) significant step-like rotations over depth intervals of about 100–300 meters, and 3) smaller-scale fluctuations around the local mean within each of the 100–300 meter intervals. We reanalyzed the acoustic wellbore image data from the pilot hole in order to increase the depth resolution of the S_{Hmax} azimuth measurements. As a result, we have individual stress orientations every 5 cm.

Theoretical modeling showed that depth-dependent fault strength on the San Andreas fault may explain the large-scale clockwise stress rotation observed in the pilot hole wellbore image data (Chéry et al., 2004). As seen in other wells (see Section 2.2.2), intermediate scale rotations in the SAFOD pilot hole are commonly associated with faults or fractures. An example is shown in Figure 2–1 (after Hickman and Zoback, 2004). Figure 2–2 presents another example where, between 800 m and 1300 m depth in both the pilot hole and main hole, wellbore failures rotate approximately 30º counter-clockwise and then back again. Because the two boreholes are only about 10 m apart in this depth range, it is reasonable to assume that the same fracture or fracture zone might be causing the observed rotation in both. Using the forward-modeling approach of Shamir and Zoback (1992; see Section 2.2.2) and the background stress state determined for SAFOD by Hickman and Zoback (2004), we adjusted modeled fault parameters such as depth, orientation, fault size, and stress drop until the stress perturbation caused by the hypothetical fault matched the wellbore observations. With 100% of 36 MPa resolved shear stress relieved by over 1 m of slip on a fault intersecting the well at 1035 m depth and dipping 63º to the northeast or southwest, we can reproduce the observed failure rotations quite closely. Barton and Zoback (1994) provide evidence that a complete

stress drop is commonly required to match wellbore failure rotation observations in a variety of geologic contexts and faulting environments.

Examination of wellbore image data reveals a wide fracture zone intersecting the pilot hole from 1022 m to 1027 m and dipping 53º to the southwest (Fig. 2–2), confirming the results of our modeling. Several discrete fractures with similar orientations intersect the main hole at the same depth.

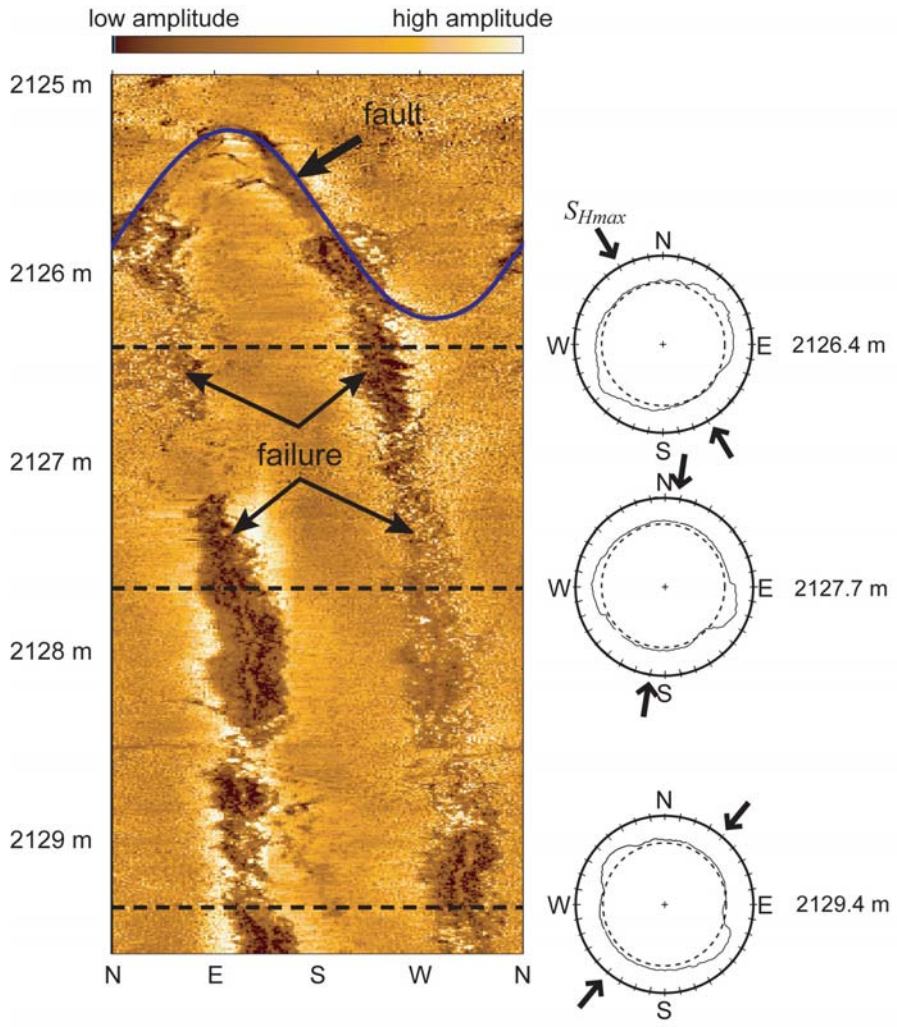

Figure 2–1. Compressive wellbore failures in image data from the SAFOD pilot hole. The amplitude of reflections collected in the well by an acoustic logging tool are used to construct a 360° image of the wellbore wall (left), while travel-time data provide information on borehole shape (cross-sections, right). Visible as low amplitudes and pockets of spalled wellbore material on opposite sides of the wellbore, the failures occur 90° from the orientation of the maximum horizontal stress (indicated by arrows, right). At 2129 meters depth, the northeast-southwest direction of maximum compression agrees with the regional stress direction, but approaching the fault at 2126 meters the compressive stress direction rotates counter-clockwise.

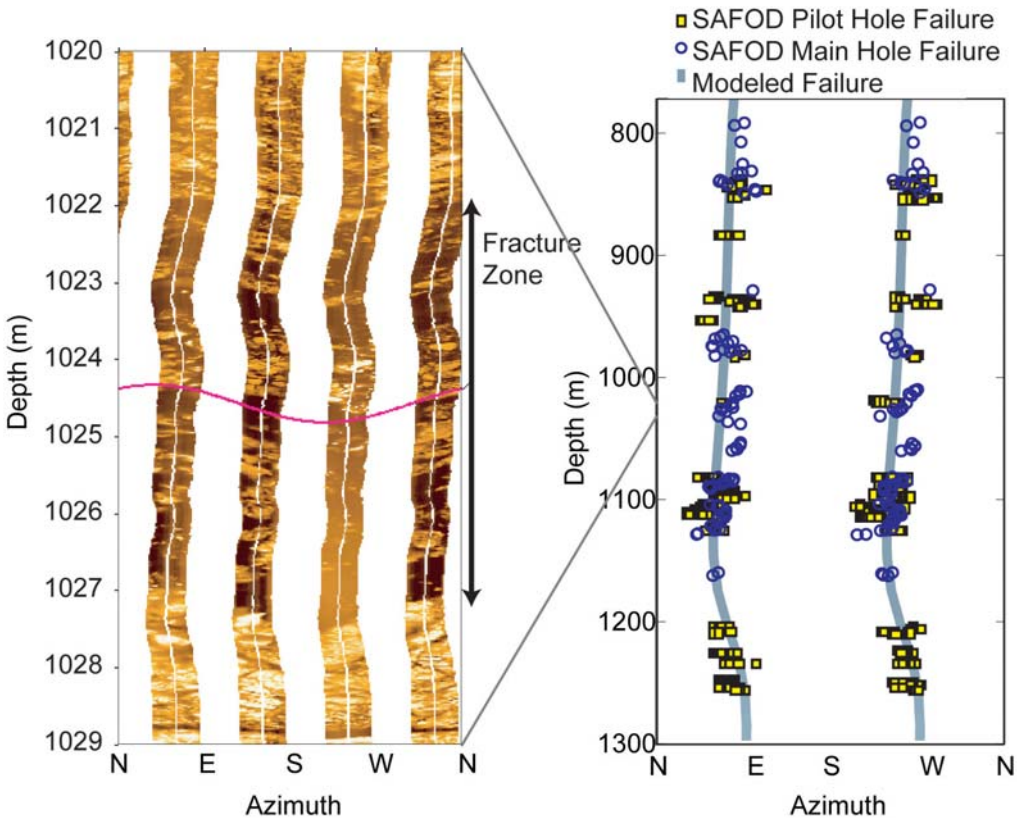

Figure 2–2. Stress rotation near a fault zone at 1025 m depth in the SAFOD pilot hole. Electrical image data from the pilot hole (left) reveals the presence of a 5-meter thick fracture zone centered at 1024.5 m and dipping 53° to the southwest (219° azimuth). Wellbore failures measured in both the pilot hole and the nearby main hole show that the direction of maximum compression is perturbed for hundreds of meters above and below the fault zone (right). Predicted failure orientations (grey) in a stress field perturbed by dislocation on a fault at the observed depth agree well with the observations.

2.3.3 Siljan

On the Baltic Shield in central Sweden, two research boreholes were drilled through 1.7 to 1.9 Ga granitic rocks in the 360 Ma Siljan Ring meteorite impact structure. Both wells, Gravberg-1 and Stenberg-1, are vertical or nearly vertical from the surface to a depth of nearly 6000 m and encounter several subhorizontal dolerite intrusions that are often associated with fracture zones.

Lund and Zoback (1999) constrained the state of stress in both Siljan boreholes using wellbore failure identified in electrical image logs and mechanical caliper data. The state of stress is strike-slip with a mean S_{Hmax} azimuth of 108°±7° in Gravberg-1 and 127°±9° in Stenberg-1. Data from Gravberg-1 provide detailed stress measurements every 15 cm, but above 1800 m these are sparse and highly scattered, and below 4850 m they are influenced by

the wellbore deviation. We analyze the original wellbore failure measurements between these two depths.

2.3.4 KTB

The KTB boreholes (Kontinentales Tiefbohrprogramm der Bundesrepublik Deutschland, now part of the GFZ Deep Crustal Laboratory) were drilled vertically to 4000 m (the pilot hole, KTB-VB) and 9100 m (the main hole, KTB-HB) through metamorphic rock in southeastern Germany. Detailed analysis of stress-induced wellbore failures (Brudy, 1995; Brudy et al., 1997; Brudy and Zoback, 1999) and induced microearthquake fault plane solutions (Bonhoff et al., 2004) reveal complex, often fault-related, heterogeneity in the local stress field at a wide range of scales. Overall, the local orientation of S_{Hmax} determined from wellbore failure, hydraulic fracturing, core disking, and strain relaxation is south-southeast–north-northwest (Brudy, 1995). Both local, natural seismicity and induced seismicity experiments at KTB reveal that the crust is strong but critically stressed, with many fractures and faults stressed close to the point of frictional failure (Dalheim et al., 1997; Zoback and Harjes, 1997).

Despite help from current and former KTB researchers, we unfortunately were not able to locate all of the wellbore stress measurements from the KTB boreholes. For the KTB pilot hole we have reliable stress orientations (that is, they match data in Brudy [1995]) from 3000 m to 3795 m only, with a spacing of 10 cm. In the main hole we have reliable data from 6027 m to 8386 m, also at a 10 cm spacing, and additional data of unknown origin and highly variable depth spacing from 3000 m to 8619 m. Due to its questionable nature, we have chosen not to include the latter data set in our analysis.

2.3.5 Data Summary

In summary, we have a total of over 13 kilometers of high-resolution wellbore stress measurements available for our analysis, covering scales from centimeters to kilometers. The actual, measured S_{Hmax} azimuths as a function of depth in each well are shown in Figure 2–3. The general characteristics of each data set are summarized in Table T2–1.

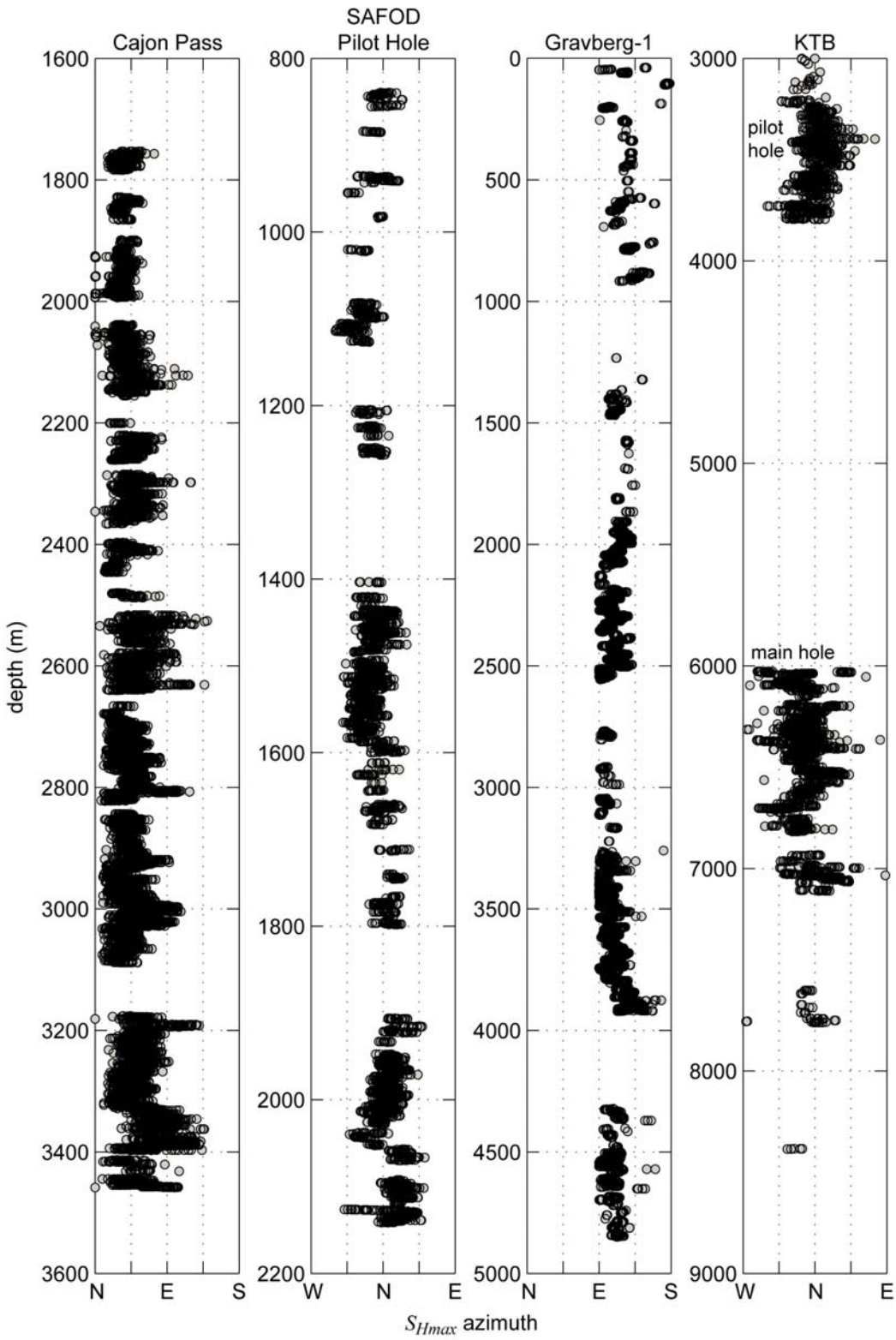

Figure 2–3. Detailed measurements of the maximum horizontal compressive stress azimuth in each of the boreholes analyzed. Gaps in the data represent intervals of missing or poor data and ambiguous or absent wellbore failure. See text and Table T2–1for data set details.

well	data type	depth interval	depth resolution	% complete	failure analysis from
Cajon Pass	acoustic image	1740 – 3460 m	0.04 m	39%	Shamir and Zoback (1992)
SAFOD Pilot Hole	acoustic and electrical images	840-2140 m	0.05 m	15%	Hickman and Zoback (2004) and this study
Siljan	4-arm caliper & electrical image	0 – 4850 m	0.15 m	22%	Lund and Zoback (1999)
KTB-VB	acoustic and electrical images	3000 – 3795 m	0.10 m	15%	Brudy (1995) and Brudy et al. (1997)
KTB-HB	caliper and acoustic and electrical images	6027 – 8386 m	0.10 m	11%	Brudy (1995) and Brudy et al. (1997)

Table T2–1. Data sets examined in this study. See text for explanations and additional details.

2.4 Quantifying Wellbore Stress Variability

Several time series analysis techniques have been applied successfully in the examination of heterogeneity in geophysical data. The goals of such analyses include determining dominant frequencies/wavelengths of periodic data and/or characterizing stochastic data (fractional Brownian motion, or colored noise). Some of the more common techniques are direct spectral analysis (e.g., the periodogram), indirect spectral analysis (e.g., the correlogram), geostatistics (e.g., the semi-variogram), autocorrelation, rescaled range, and more recently the wavelet transform (for some comparisons of techniques see Dolan et al., 1998, Constable and Johnson, 2005, and Ghil et al., 2002).

Spectral analysis is by far the most common technique applied to analyzing heterogeneity in well log data (see Section 2.5.1). We employ two different spectral analysis methods to analyze heterogeneity in our wellbore stress orientation measurements. The periodogram provides us with moderate success, but the interpolation required to create a continuous data set seems to have a significant influence on the results. A relatively new spectral analysis technique called auto-regressive, moving-average spectral analysis (ARMASA) provides a more robust result by operating only on the existing data, requiring no assumptions about missing observations.

2.4.1 Periodogram

Spectral analysis determines the periodic components of a signal, assuming that the signal is made up of superimposed sine waves of different frequencies. The power spectral density (PSD) is the power, or energy, of the signal per unit frequency and can be calculated directly from the signal by means of the periodogram,

$$\mathrm{PSD} = \frac{\left|X_L(f)\right|^2}{f_s L}, \qquad \text{(E2–1)}$$

where X_L is the discrete-time Fourier transform of the signal, f is frequency, f_s is the sampling frequency, and L is the length of the entire record (e.g., Davis, 2002). Valid results are obtained for frequencies between $1/L$ and the Nyquist (highest resolvable) frequency, $1/2l$, where l is the sampling resolution.

For a scale-invariant (i.e., fractal) phenomenon there are no dominant spatial frequencies, and spectral analysis will reveal a power-law relationship between the power spectral density and wavelength ($1/f$) such that

$$PSD \propto \lambda^{\beta}, \qquad \text{(E2–2)}$$

where β is called the spectral (or scaling) exponent. Power law behavior implies that the same process is operating at all scales—that is, that the signal is fractal. The fractal dimension, D, is related to the spectral exponent by

$$D = \frac{5-\beta}{2} \qquad \text{(E2–3)}$$

(e.g., Turcotte, 1997). In general, such scaling will hold only over a certain range of wavelengths. A change in scaling properties at a particular wavelength can be indicative of a change in the process responsible for the signal. In determining the spectral exponent or fractal dimension, it is important to indicate how it was calculated and over what range of wavelengths it is applicable.

The Welch periodogram is one of the most widely used periodogram methods. It divides the data series into segments, which may overlap, before a windowed periodogram of each segment is calculated. The segment estimates are then averaged to get the series PSD. Various types of windows can be used to optimize the calculations. This approach provides several advantages such as reducing the effects of sidelobes (also called spectral leakage), which can

mask weak signals, and providing tradeoff between the variance and resolution of the PSD estimate (Marple, 1987).

Because the periodogram requires a continuous, stationary series with a constant sample spacing, our data sets required several adjustments before we could apply the Welch periodogram. First, we subtracted the mean S_{Hmax} orientation for the entire well and removed extreme outliers (e.g., Holliger et al., 1996) in order to obtain a series of rotation values between -90° and +90º (clockwise positive). We did not try to remove any variation with depth because we are interested in detecting long-wavelength perturbations. In order to make the data continuous, we had to provide rotation magnitudes over intervals where they were lacking. Such intervals can occur because of either data acquisition effects or the nature of the in situ stress state; a wellbore image is essentially continuous in depth but may contain prohibitively low quality segments because of tool problems or wellbore conditions, and stress-induced failures, where they occur, can vary in length from a fraction of a meter to several meters or more.

We compared two different approaches for filling the gaps in our data, one in which we simply set the rotation values to 0º over these intervals, and another in which we performed a linear or cubic spline interpolation. A comparison of these approaches used on the SAFOD pilot hole data is shown in Figure 2–4. Clearly the two results display marked differences. The first approach shows high variability at small wavelengths and a distinct break in spectral slope. The interpolated data display a consistent, higher slope. We found little difference between using linear or cubic spline interpolation (the figure shows results using cubic spline). However, because an interpolator does not capture the high-frequency variation evident in intervals up to several hundred meters long in the raw data, the resulting power spectrum may have artificially low power at small wavelengths versus larger ones. Despite this drawback, we consider the interpolated approach to be better than simply replacing the missing data with a constant value.

The power spectra for interpolated data from all of the study wells are shown in Figure 2–5. Clearly, none of the spectra indicate that stress orientations fluctuate at distinct frequencies. Instead the PSD increases linearly with wavelength, indicating that the data series behave as power-law noise. Spectral exponents determined from linear least-squares regression of the spectra are also shown in the figure. They range from 1.36 in Cajon Pass to 1.93 in the KTB main hole.

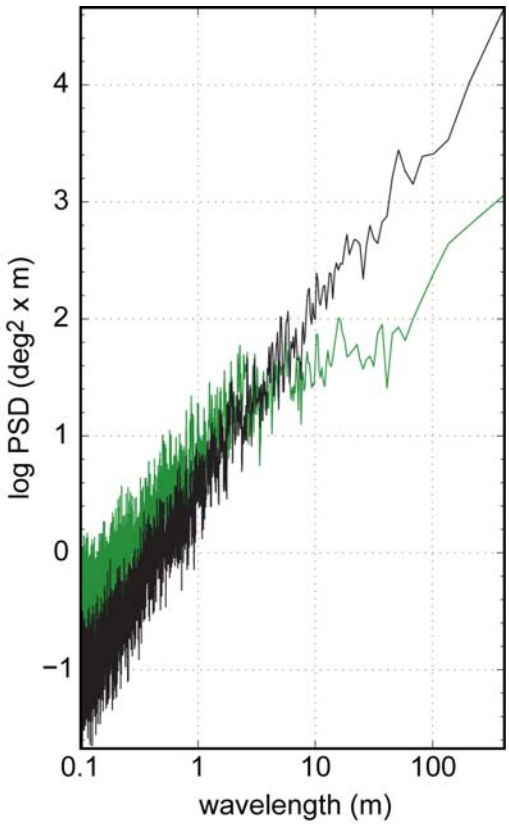

Figure 2–4. Comparison of Welch periodogram results for the SAFOD pilot hole using zero-filled (green) versus interpolated (black) data.

Shamir and Zoback (1992) performed a similar analysis on short intervals of stress orientations in the Cajon Pass well. As in our analysis, they used the periodogram approach on interpolated data (neither the type of periodogram nor the method of interpolation were specified). They found $\beta = 2.18$ in the interval 2891 to 2936 m, 1.9 in the interval 2962 to 3051m, and 1.38 in the interval 3275 to 3397 m. It is interesting to note that their β estimate decreased as the length of the analyzed interval increased, finally approaching a value in agreement with our findings.

2.4.2 ARMASA

As mentioned in the previous discussion, wellbore stress measurements are by their very nature intermittent and unevenly spaced. The Lomb-Scargle method (Lomb, 1976; Scargle, 1982) is a popular spectral analysis technique developed specifically for missing data problems. Unfortunately for our purposes, it has been demonstrated that while Lomb-Scargle is suitable for determining dominant frequencies, it can give highly inaccurate estimates of spectral slope for colored noise (Broersen et al., 2004).

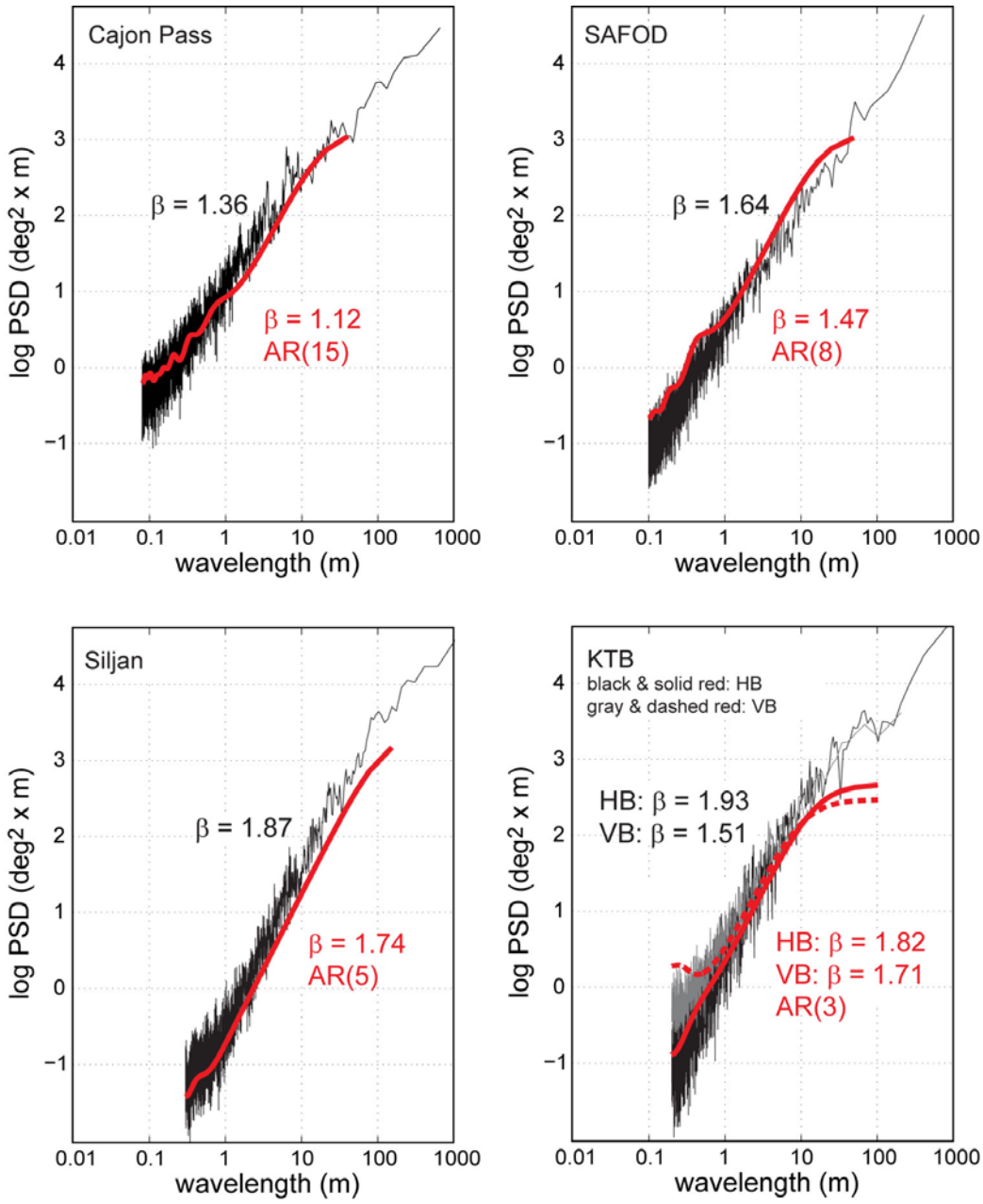

Figure 2–5. Power spectra calculated using the Welch periodogram (black) and ARMASA (red) on stress orientation data from each of the study wellbores.

The auto-regressive, moving average spectral analysis (ARMASA) method is an indirect, parametric approach to determining the power spectrum that, for the analysis of stochastic data, performs better than the best windowed periodogram (Broersen, 2000 and 2002). The technique first creates hundreds of AR (auto-regressive), MA (moving-average), and ARMA models based on the data. Using automatic statistical model selection criteria, it determines the best model from each category and then calculates the power spectrum of the one that has the

smallest expected prediction error. Bos et al. (2002) modified the approach to analyze segmented data sets, and de Waele (2003) further modified it to analyze data sets with missing observations. The latter is an approximate, finite-interval maximum likelihood estimator that works exceptionally well even when more than 90% of the observations are missing (Broersen et al., 2004). Codes for the basic (ARMASA_1_7.zip) and modified (AutomaticSpectra.zip) ARMASA approaches can be downloaded from the MATLAB™ Central File Exchange (www.mathworks.com).

We tested both Lomb-Scargle and ARMASA on synthetic colored noise, and our results agree with those of Broersen et al. (2004). For a series with $\beta = 2$ and 75% of an original 2000 data points randomly removed, the spectral slope determined using Lomb-Scargle was off by more than 75%. In contrast, the ARMASA approach gave a spectral slope within 2–3% of the correct value. To make sure ARMASA would compare directly with the periodogram approach on a continuous data set, we ran it on the interpolated data for Cajon Pass and Siljan as well as on an interpolated version of our synthetic, decimated data set. For all three, the spectral slopes from both methods were within 99% of each other. Importantly, however, both ARMASA and the Welch periodogram gave spectral slopes for the interpolated synthetic data that were greater than the real value by more than 30%.

The ARMASA-derived power spectrum (superimposed on the periodogram spectrum), spectral exponent, and AR model order for each data set are shown in Figure 2–5. The smoothness and smaller maximum wavelength of the ARMASA spectra are artifacts of the ARMASA algorithm. Fluctuations at the high-frequency/small-wavelength end of the spectrum increase with increasing AR model order. The only data set for which the ARMASA-derived spectrum did not show a linear slope over the entire wavelength range was KTB. In the KTB main hole, deviation from a linear slope at longer wavelengths did not significantly affect the linear regression. In the KTB pilot hole, however, deviations at both ends of the spectrum had a strong effect on the regression, resulting in a good linear fit only in the wavelength range 68 cm to 10 m.

Uncertainty in our spectral exponent values comes from several sources including the spectral estimator itself and the subsequent linear regression, so exact values are difficult to estimate. For the periodogram it is on the order of 0.03 to 0.05 in Cajon Pass, SAFOD, and Siljan and higher, 0.05 to 0.10, in KTB. For ARMASA, it is small (0.02 to 0.08) for Cajon Pass and SAFOD, a little higher (0.11) for Siljan, and because of the artifacts in the ARMASA spectra, uncertain for KTB. Given these estimates, the smaller spectral exponents determined

by ARMASA versus those from the periodogram (except for the KTB pilot hole) are meaningful. Differences range from 6% (KTB main hole) to 18% (Cajon Pass), confirming that interpolation of the data overestimates the spectral slope.

2.4.3 Summary

With spectral exponents between 1 and 2, stress orientation heterogeneity in the study wellbores behaves as fractional Brownian motion somewhere between 1/*f* noise (β = 1, pronounced "one over f noise," a.k.a. "pink" or "flicker" noise) and true Brownian motion (β = 2, a.k.a. "random walk") (Mandelbrot and Van Ness, 1968). Examples of these types of noises are shown in Figure 2–6. For comparison, white noise (β = 0) is also shown. White noise is completely uncorrelated, with equal fluctuations at all scales. A higher beta value indicates relatively larger long-wavelength variations and smaller short-wavelength variations. For 1/*f* noise, the increase in mean fluctuation scales on a one-to-one relationship with increase in wavelength. Although 1/*f* noise is now considered ubiquitous in geophysics and astronomy, its cause has yet to be determined (see, e.g., Bak, 1987).

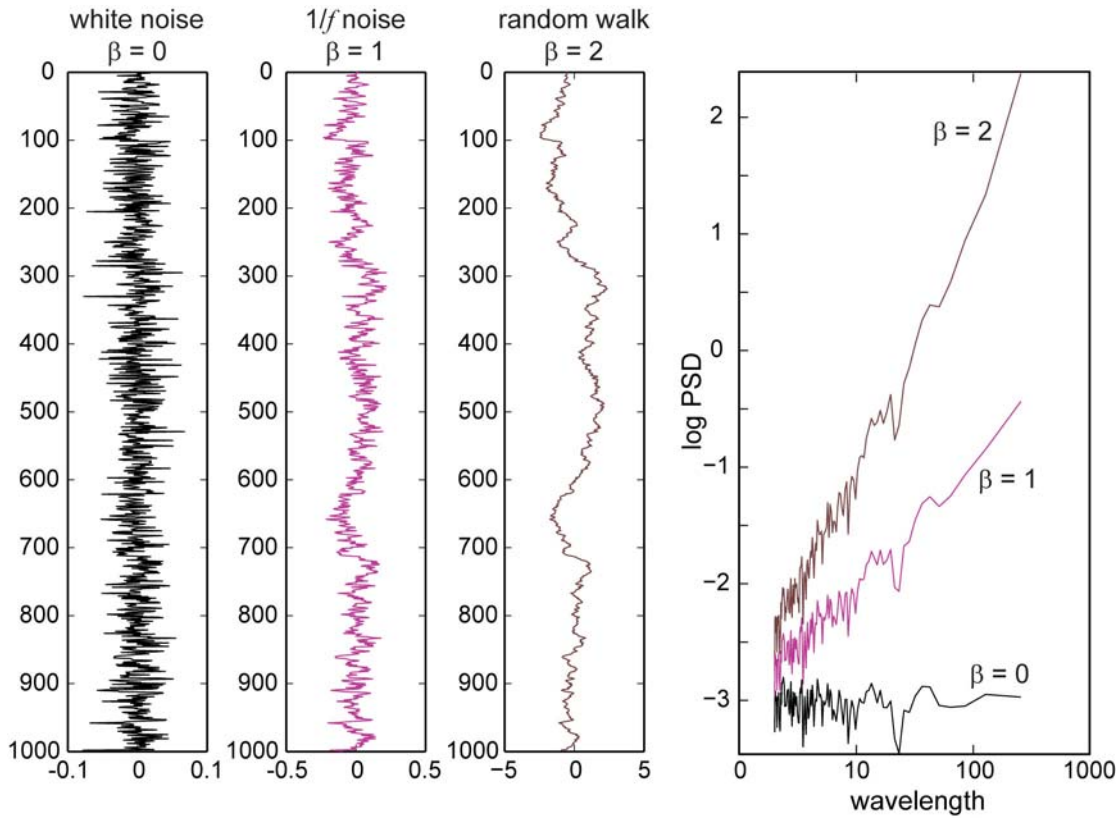

Figure 2–6. Examples of colored noises (three plots on left) and their power spectral densities (right-hand plot).

2.5 Discussion

Having shown that stress orientation heterogeneity in well logs can be characterized as power-law noise, our goal is to gain insight into its causes. It is not uncommon for scaling to be used to infer a cause and effect relationship between phenomena (e.g., Bean, 1996; Tessier et al., 1996). We use this premise to examine two of the leading candidates for factors which control stress heterogeneities at the wellbore scale: variations in lithology (or rock properties) and slip on pre-existing faults.

2.5.1 Physical Property Heterogeneity

As mentioned in the previous section, it has long been recognized that a variety of geophysical data exhibit fractal characteristics in both space and time (e.g., see reviews by Sornette, 2000 and Turcotte, 1997). Numerous studies have found that heterogeneity in well log data in particular (e.g., sonic velocities, gamma, bulk density, etc.), exhibits $1/f$ noise behavior. The $1/f$ scaling seems to be independent of factors such as lithology, structure, chemical composition, and tectonic history (Holliger, 1996), although the similarity in the exponents for different logs may to some degree be due to the interdependency of some physical properties (Dolan et al., 1998). Jones and Holliger (1997) actually examined several of these relationships at KTB, finding gamma sensitive to lithology and resistivity sensitive to pore fluid. Jones and Holliger (1997) tested the correlation between physical property variation and caliper logs, a proxy for wellbore failure, and found a lack of coherence indicating that compressive wellbore failure caused no predictable changes in physical properties or vice versa. Marsan and Bean's (1999) use of the structure function indicates that P-wave velocity and gamma might be multifractal in the KTB main hole. The physical property heterogeneity scaling seems to persist in the horizontal direction as well, although β might be slightly higher and/or anisotropic (Dolan et al, 1998; Jones and Holliger, 1997; Leary, 1997; Wu et al., 1994).

Spectral exponents for physical property log heterogeneity in each of the wellbores studied are summarized in Table T2–2. For Cajon Pass, Siljan and KTB, these values come from previous analyses, and uncertainties are listed when provided by the authors. Following the procedure outlined in the previous section and correcting for logging tool resolution (Bean, 1996; Holliger et al., 1996), we used the Welch periodogram to calculate the PSD of variability in sonic velocity, bulk density, neutron porosity, gamma-ray, and formation resistivity logs from the SAFOD pilot hole and then performed linear regression on the

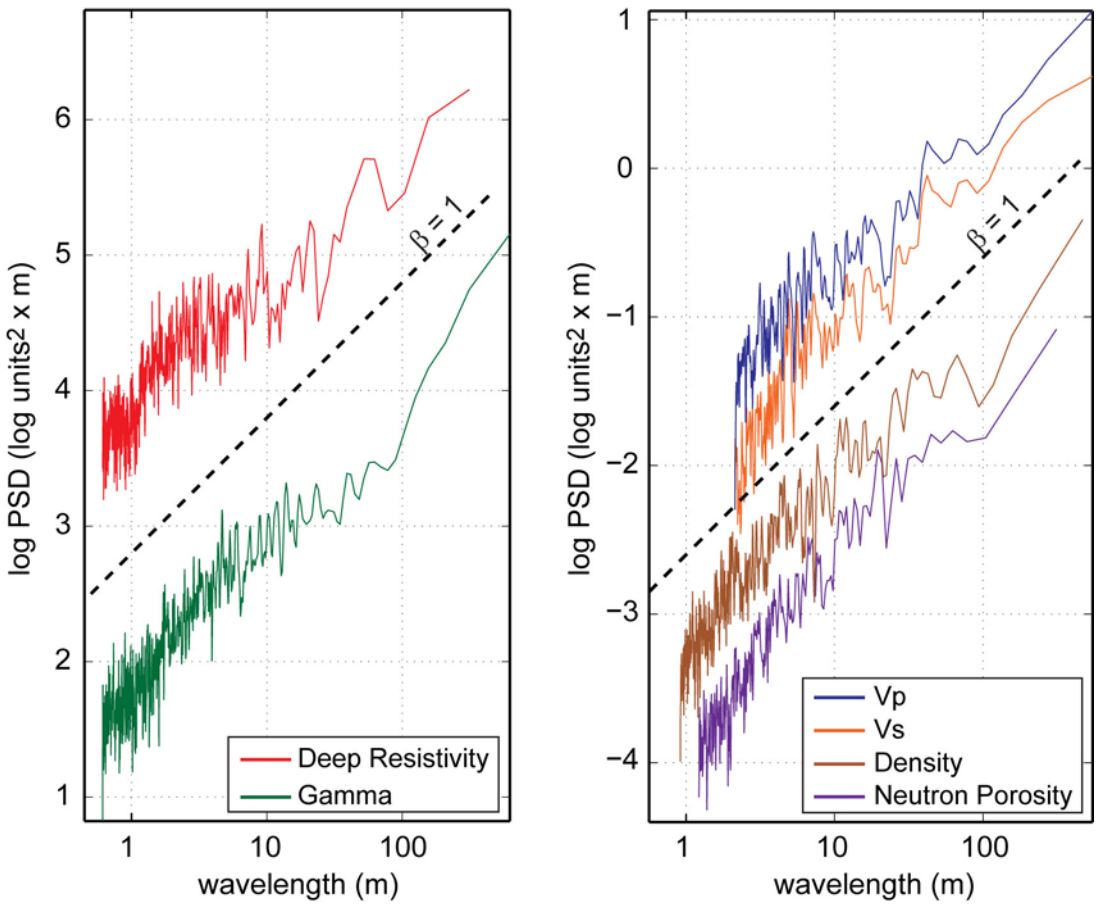

Figure 2–7. Power spectra (from Welch periodogram) of heterogeneity in some physical property logs from the SAFOD pilot hole, showing spectral slopes very close to β = 1.

resulting spectra. Four of the spectra are shown in Figure 2–7. Our results are also provided in Table T2–2.

Spectral exponent values in all of the wellbores are in general quite consistent and close to 1. These agree with values found in other locations such as Ireland (Bean 1996), Canada (Holliger et al., 1996; Todoeschuck et al., 1990), and the North Sea and Japan (Leary 1997). In all cases they are significantly lower than the spectral exponents we determined for the wellbore stress heterogeneity. This implies that different physical mechanisms are responsible for the two phenomena.

Well	Vp	Vs	deep resistivity	shallow resistivity	neutron porosity	gamma	density
Cajon Pass	1.05 [1]	0.94 [1]	no data	no data	no data	1 [1]	1.06 [1]
SAFOD	1.00 ± 0.06	no data	0.96 ± 0.04	0.88 ± 0.04	1.33 ± 0.06	1.11 ± 0.02	1.15 ± 0.04
Siljan	1.2 [2] ~ 1 [3] **(MEAN = 1.1)**	no data	no data	no data	no data	no data	no data
KTB-HB (main hole)	1 [4] 1.11 ± 0.04 [5] 1.0 [6] ~ 1 [7] 1.07 ± 0.1 [8] 1.132 ± 0.0075 [9] 0.97 ± 0.005 [10] **(MEAN = 1.04)**	1.18 ± 0.04 [5] 1.2 [6] ~ 1 [7] **(MEAN = 1.13)**	1.5 [6] ~ 1 [7]	1.9 [6] ~ 1 [7]	1.2 [6] ~ 1 [7]	2 [4] 1.4 [6] ~ 1 [7] 1.46 ± 0.13 [8] **(MEAN = 1.46)**	1.2 [6] ~ 1 [7] **(MEAN = 1.1)**
KTB-VB (pilot hole)	1.11 ± 0.04 [5] 0.9 [6] ~ 1 [7] 1.25 ± 0.004 [10] **(MEAN = 1.07)**	1.18 ± 0.04 [5] 1.0 [6] ~ 1 [7] **(MEAN = 1.06)**	1.1 [6] ~ 1 [7] **(MEAN = 1.05)**	0.9 [6] ~ 1 [7] **(MEAN = 0.95)**	1.1 [6] ~ 1 [7] **(MEAN = 1.05)**	1.7 [6] ~ 1 [7] **(MEAN = 1.35)**	0.6 [6] ~ 1 [7] **(MEAN = 0.8)**

Table T2–2. Spectral exponents for physical log heterogeneity in each of the study wellbores. [Sources: [1]Leary, 1997, power spectrum (periodogram); [2]Holliger et al., 1996, Stenberg-1, autocovariance; [3]Line et al., 1998, Gravberg-1, power spectrum (periodogram); [4]Goff and Holliger, 1999, covariance; [5]Jones and Holliger, 1997, robust power spectrum; [6]Leonardi and Kümpel, 1998, power spectrum (periodogram); [7]Leonardi and Kümpel, 1998, rescaled range; [8]Marsan and Bean, 1999, power spectrum; [9]Marsan and Bean, 1999, structure function; [10]Wu et al., 1994, power spectrum]

2.5.2 Fractures and Faulting

Fractures, faulting and seismicity are perhaps the best known and most widely studied scale-invariant phenomena in geophysics. Fractures in the earth's shallow crust often have fractal spatial and length distributions (e.g., Barton, 1995; Bean and McCloskey, 1993; Berkowitz and Hadad, 1997; Bonnet et al., 2001; Velde et al., 1991), to the extent that their scaling properties have even be used to predict a parent fracture population from a restricted set of measurements (La Pointe, 2002). At Cajon Pass the distributions of fracture aperture and spacing are fractal (Barton and Zoback, 1992; Leary, 1991). Likewise at KTB induced seismicity experiments reveal that the crust is heavily fractured even at great depth (Leary et al., 1988; Zoback and Harjes, 1997), and both fracture lengths and the spatial distribution of fracture orientations are fractal, showing the same character from thin-section to seismic scales (Zimmerman et al., 2003).

Similarly, earthquakes display scale-invariant characteristics in magnitude, frequency of occurrence, and spatial distribution, and fractal concepts have found widespread application in the fields of seismology and fault mechanics (see review by Bak and Chen, 1995; Kanamori and Anderson, 1975). Frankel (1991), for example, used a model based on a scale-invariant fault strength distribution to explain several earthquake characteristics including the b-value of aftershock sequences. In the model, subevent areas correspond to small-scale perturbations of stress on the fault plane, and stress drop is related to the amplitude and standard deviation of the spatial distribution of fault stress. Source mechanisms of induced earthquakes at the KTB site suggest a direct relationship between earthquake size and stress heterogeneity at different scales (Bohnhoff et al., 2004).

By combining several basic scaling relationships in seismicity, the fractal dimension of earthquakes is shown to be a function of the earthquake b-value from the Gutenberg-Richter Law (e.g., see review in Chen et al., 2006 and derivations by Leary, 1991 and Main et al., 1994 among others). The Gutenberg-Richter Law (Gutenberg and Richter, 1944) defines a logarithmic scaling relationship between the number of earthquakes, N, and earthquake magnitude, M, according to

$$\log N = a - bM \ , \tag{E2–4}$$

where a and b are both constants, b being the earthquake b-value. Likewise, magnitude and moment, M_o, are related by

$$\log Mo = p + qM \ , \tag{E2–5}$$

where p and q are again constants. Moment can be expressed as a function of fault size, L_f, according to

$$Mo = \frac{\Delta\sigma \cdot {L_f}^d}{c} , \tag{E2–6}$$

in which $\Delta\sigma$ is stress drop and c and d are constants that depend on the fault geometry. By substituting Eqn. E2–6 into Eqn. E2–5, then solving for M and substituting into Eqn. E2–4, we can express the relationship between the number of earthquakes and the fault size as,

$$\log N \propto -\frac{bd}{q} \log L_f \ , \tag{E2–7}$$

or equivalently,

$$\log N \propto -D_{eq} \log L_f \ , \tag{E2–8}$$

where

$$D_{eq} = \frac{bd}{q} \tag{E2–9}$$

is the earthquake fractal dimension. We thus expect a plot of earthquake frequency versus fault size to be linear in log space and drop off at a rate equivalent to the earthquake fractal dimension. D_{eq} is effectively the scaling exponent, analogous to β, for the relationship between number of seismic events and fault size.

On a world-wide average q is approximately 1.5 (Kanamori and Anderson, 1975), and b is generally around 1. The frequency–magnitude scaling relationship quantified by the b-value has been shown to hold down to very small (M = 0 or less) seismic events (Abercrombie, 1996) and is controlled at least partly by the relative distribution of fault lengths in a given region (Wesnousky et al., 1983). The constant d ranges from 2 for small, radially symmetric earthquake ruptures to 3 for larger events that span the brittle crust and rupture a considerable distance along strike (King, 1983). Using these values, average earthquake fractal dimension ranges from 1.3 to 2.0. This is remarkably similar to the range of spectral exponents we found for stress orientation heterogeneity, suggesting that a fractal size distribution of seismogenic events in the crust controls the multi-scale stress heterogeneity we observe in our study wells. In other words, the pattern of wellbore stress along the boreholes results from the superposition of small stress perturbations from numerous small faults onto larger, long-wavelength perturbations caused by fewer larger faults. The contribution of small seismic events in distributing elastic stress in the crust has been demonstrated by Hanks (1992) and Marsan (2005, 2006), who showed that small earthquakes are equally as important as large ones, redistributing stress over shorter wavelengths but in greater numbers.

Local b-values often deviate significantly from the global average value of 1. The cause is unclear, but it may be related to factors such as situ stress regime (Schorlemmer et al., 2005), regional stress magnitudes (Huang and Turcotte, 1988), or fault strength heterogeneity (Steacy et al. 1996). Seismological estimates for b-values in our study regions differ markedly. For the creeping section of the San Andreas fault near SAFOD, b is estimated to be around 1.1 (Schorlemmer et al., 2004; Wyss et al., 2004). At Cajon Pass, where the San Andreas is locked, b is between 0.9 and 1 (Abercrombie, 1996; Schorlemmer et al., 2004; Wesnousky, 1994). Seismic activity in Sweden is low in general, with two areas of relatively frequent, low-magnitude events: one along the coast of the Gulf of Bothnia and another in the Lake Vanern region to the southwest of Siljan (La Pointe et al., 2002). We could find no estimates of b-

values near Siljan in particular, but estimates for larger regions range from 1.04 for southern Sweden to 1.35 for northern Sweden (La Pointe et al., 2002). Earthquakes near KTB are rare, although the Vogtland/Western Bohemia area 50 km to the northeast is one of the most seismically active areas in central Europe, characterized by swarms of earthquakes believed to be caused by crustal fluid flow (Kurz et al., 2004; Neunhöfer and Meier, 2004). Events recorded on the local seismic network around KTB include only a handful of very low-magnitude single events within roughly 10 km of the site and several earthquake swarms 20 km to the north (Dahlheim et al., 1997). Estimates for b-values of non-swarm activity in the Vogtland area are very low, near 0.5 or less. Earthquake swarms in these regions, however, often yield b-values well above 1.0 and sometimes even greater than 2.0 (Neunhöfer and Meier, 2004).

Using the individual b-value estimates for each of the study areas, we can derive unique earthquake fractal dimensions for each site, which we present in Table T2–3. Interestingly, both earthquake fractal dimension and β show the same relative differences between wells. This may reflect a relationship between in situ stress heterogeneity and local faulting environment. The relative influence of small faults versus larger ones is related to the local tectonic setting; in regions with very few large earthquakes (characterized by a higher b-value), both the earthquake fractal dimension and stress perturbation spectral exponent are higher.

well	ARMASA β	b-value	D_{eq}
Cajon Pass	1.12	0.9	1.17 to 1.35
SAFOD	1.47	1.1	1.43 to 1.65
Siljan	1.74	1.04 to 1.35	1.35 to 2.02
KTB-VB	1.71	> 1	> 1.3 to 1.5
KTB-HB	1.82	> 1	> 1.3 to 1.5

Table T2–3. Comparison of best spectral exponents for stress heterogeneity in each of the study areas with b-value estimates and earthquake fractal dimension.

Overlaying the periodogram spectra from all of the wells (Fig. 2–8) illustrates the differences in the spectra between the different wells. Most of the differences occur at smaller wavelengths, while the spectra tend to converge at wavelengths approaching 100 m.

Convergence at longer wavelengths may indicate the transition from stress being controlled by local fault-related phenomena to control by large-scale tectonic processes.

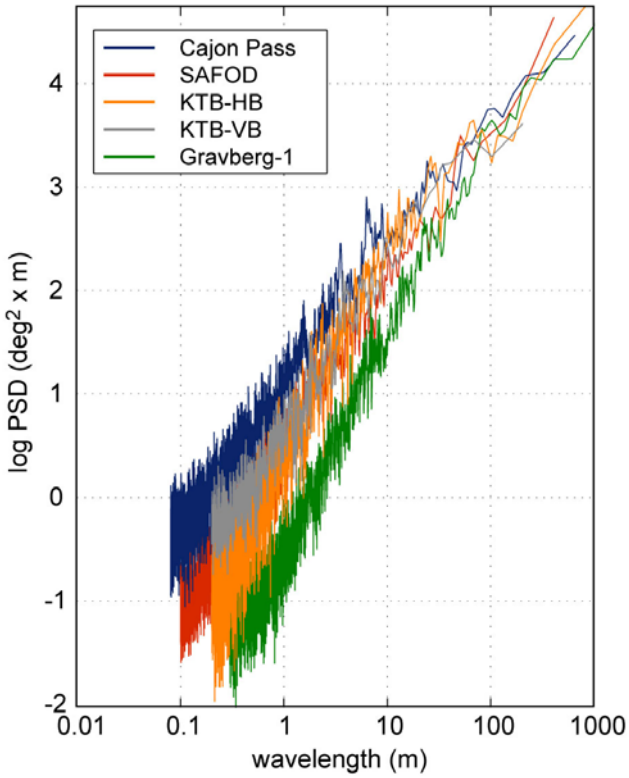

Figure 2–8. Periodogram power spectra for all of the wellbores superimposed, showing about the same PSD at long wavelengths, becoming more distinct at small wavelengths.

2.5.3 Stress Criticality

The conceptual model of self-organized criticality (SOC) holds that natural systems organize themselves into states that are just barely stable, the result being that local perturbations propagate through the system at all length scales (Bak, 1996; Bak et al., 1987). The fundamental properties of SOC processes are: (1) highly non-linear behavior, (2) a very slow driving rate, (3) stationary statistical properties, (4) power-law size distributions, and (5) fractal geometry. The concept has found widespread application in earthquake studies, providing rationalization of the Gutenberg-Richter law, fractal fault characteristics, and the spatial distributions of earthquake epicenters (Rundle et al., 2000; Sleep, 2002). Leary (1991) cited SOC as a mechanism for fractal fracture clustering at Cajon Pass. Arguments that self-organized fractures are responsible for the common scaling between various types of well logs suggests that the brittle crust is in a state of so-called fracture criticality.

Another aspect of SOC theory as applied to the earth is that the brittle crust is in a state of stress criticality, as evidenced by the presence of critically stressed fractures and faults (Baisch et al., 2002; Barton et al., 1995), the relationship of such faults to crustal strength (Townend and Zoback, 2000), and seismicity induced under conditions of low stress and fluid pressure perturbations (Cornet, 2007). The latter phenomenon has been observed at many locations including Cajon Pass (Abercrombie and Leary, 1993) and the KTB site (Zoback and Harjes, 1997). Our results support the critical stress concept by showing that at least one component of the in situ stress tensor—its orientation—displays fractal heterogeneity over length scales from centimeters to kilometers. Within this range, we see no breakdown of fractal scaling, although it is likely that the true upper limit is controlled by the highest level of stress that can be maintained without failure (the yield stress) in a given area. Stress variability has important implications in several fields such as Coulomb stress triggering (Marsan, 2006), earthquake inversion (Abers and Gephart 2001; Ghisetti, 2000), and rupture source modeling (Harris, 2004).

2.5.4 Suggestions for Further Work

We hope that our analysis will provide the basis for further characterization and modeling of in situ stress heterogeneity. Obviously, confirming our results by analyzing additional boreholes in more tectonic settings, particularly ones where seismic parameters such as the b-value and earthquake fractal dimension are well-constrained, would be the next logical step. Obtaining the full wellbore failure data set for KTB, either by finding previous results or reanalyzing the wellbore image and caliper logs, would be an important contribution considering that KTB is one of the deepest and most thoroughly analyzed scientific wells drilled to date. In addition, if an area could be found where data from multiple wellbores were available, our approach could perhaps be extended to 2-D or 3-D. A full statistical characterization of stress heterogeneity should allow development of a model that can provide stress estimates where data are missing or sparse [e.g., Kondrashov and Ghil, 2006; Bean and McCloskey, 1995). Using geostatistical approaches, the model could be conditioned to existing data and made to incorporate additional types of data and physical insight.

As for methodology, series analysis with wavelets is finding increasing geophysical application in recent years, particularly where scaling issues are important (e.g., Kumar and Foufoula-Georgiou, 1997). The approach would be particularly appropriate for analyzing stress heterogeneity. First, unlike traditional spectral analysis, wavelet analysis does not

assume that the periodic components in a signal are sinusoidal. Second, wavelets can deal with non-stationary data. Most importantly, however, wavelet analysis not only finds scaling properties, but it also identifies locations in the series where these scaling properties change (Wornell, 1996), which may provide further insight into the causative mechanisms of stress heterogeneity.

Finally, our work encourages further attempts to use a stochastic approach to understand and forecast the occurrence of earthquakes (e.g., Rundle et al., 2003; Hergarten et al., 2002). Stochastic approaches have already proven useful for describing heterogeneous fault properties and incorporating complex source parameters into earthquake rupture modeling (e.g., Hallgass et al., 1997; Hansen et al., 2000; Johnson and Nadeau, 2002; Lavalee et al., 2006; Mai and Beroza, 2003; Oglesby and Day, 2002; Peyrat et al., 2004). Turcotte (1986), for example, used fractal-based calculations to estimate earthquake repeat intervals for various faults. Using data from the San Andreas in central California, this provided an estimated repeat time of 35.4 years for the well-known Parkfield repeating magnitude 6 event. The latest two Parkfield events, in fact, occurred 32 and 38 years after one before it.

2.6 Conclusions

Our analysis of multi-scale variations in the direction of maximum horizontal compressive stress in several different wells finds that the variation displays scale-invariant, fractal distributions with spectral exponents between 1 and 2. The stress scaling differs significantly from the scaling of physical property heterogeneity as measured in well logs, which has a spectral exponent of about 1. The stress variations are, however, remarkably similar to the spatial scaling of earthquakes as a function of fault size in the study areas. We suggest that wellbore stress heterogeneity over the range of scales examined is controlled by slip on a fractal distribution of active faults in the surrounding crust.

Stress heterogeneity may not be predictable in an absolute sense, but our research providing insight into its scaling properties suggests it may be predictable in a statistical sense, which may aid in applications where changes in stress are important. In addition, our conclusion is consistent with the concepts of fractal fault distributions and a scale-free, complex network of seismicity in a critically stressed brittle crust. The observed correlation between the amount of stress heterogeneity and local fault behavior may prove useful in models of dynamic earthquake rupture, where many of the key parameters including stress and fault strength appear to vary spatially.

2.7 Acknowledgments

We wish to thank Gadi Shamir (Ministry of National Infrastructures, Israel), Björn Lund (Uppsala University, Sweden), Jochem Kück (GeoForschungsZentrum, Potsdam), and Birgit Müller (Universität Karlsruhe) for providing data from Cajon Pass, Siljan, and KTB. We also thank John Langbein (U.S. Geological Survey) for his interest in the project and P.M.T. Broersen and Stijn de Waele (Delft University of Technology) for making the ARMASA code freely available. Finally, we are grateful to numerous sources of financial support including the National Science Foundation Earthscope Project, the Stanford Rock and Borehole Geophysics Project, and the U.S. Geological Survey's Earthquake Hazards Program. A.D.L. appreciates scholarship support from the Society of Exploration Geophysicists Foundation and the Society of Petrophysicists and Well Log Analysts.

2.8 Explanation of Symbols

a, b	constants in the Gutenberg–Richter relationship (b is the earthquake b-value)
c, d	constants in the expression for earthquake moment
D	fractal dimension
D_{eq}	earthquake fractal dimension
f	frequency (for a time or spatial series)
f_s	sampling frequency of a data series
L	length of a data series
L_f	fault size
l	sampling interval of a data series
M	earthquake magnitude
M_o	earthquake moment
N	number of earthquakes
p, q	constants in the earthquake moment–magnitude relationship
S_{Hmax}	maximum in situ horizontal compressive stress
S_{hmin}	minimum in situ horizontal compressive stress
X_L	Fourier transform
β	spectral (or scaling) exponent
λ	wavelength
$\Delta\sigma$	earthquake stress drop

2.9 References

Abercrombie, R. E. (1996), The magnitude-frequency distribution of earthquakes recorded with deep seismometers at Cajon Pass, southern California, *Tectonophysics, 261*, 1–7.

Abercrombie, R., and P. Leary (1993), Source parameters of small earthquakes recorded at 2.5 km depth Cajon Pass, southern California: Implications for earthquake scaling, *Geophys. Res. Lett., 20*, 1511–1514.

Abers, G. A., and J. W. Gephart (2001), Direct inversion of earthquake focal first motions for both the stress tensor and focal mechanisms and application to southern California, *J. Geophys. Res., B, 106*, 26523–26540.

Baisch, S., M. Bohnhoff, L. Ceranna, Y. Tu, and H.-P. Harjes (2002), Probing the crust to 9-km depth: Fluid-injection experiments and induced seismicity at the KTB superdeep drilling hole, Germany, *Bull. Seismol. Soc. Am., 92*, 2369–2380.

Bak, P. (1996), *How Nature Works: The Science of Self-Organized Criticality*, 212 pp., Copernicus, New York.

Bak, P., and K. Chen (1995), Fractal dynamics of earthquakes, in *Fractals in the Earth Sciences*, edited by C. C. Barton and P. R. La Pointe, pp. 227–236, Plenum Press, New York.

Bak, P., C. Tang, and K. Wiesenfeld (1987), Self-organized criticality: An explanation for 1/f noise, *Phys. Rev. Lett., 59*, 381–384.

Barton, C. A., and M. D. Zoback (1992), Self-similar distribution and properties of macroscopic fractures at depth in crystalline rock in the Cajon Pass Scientific Drill Hole, *J. Geophys. Res., B, 97*, 5181–5200.

Barton, C. A., and M. D. Zoback (1994), Stress perturbations associated with active faults penetrated by boreholes: Evidence for near complete stress drop and a new technique for stress magnitude measurement, *J. Geophys. Res., B, 99*, 9373–9390.

Barton, C. A., M. D. Zoback, and D. Moos (1995), Fluid flow along potentially active faults in crystalline rock, *Geology, 23*, 683–686.

Barton, C. C., and P. R. La Pointe (Eds.) (1995), Fractals in the Earth Sciences, 284 pp., Plenum Press, New York.

Barton, C. C. (1995), Fractal analysis of scaling and spatial clustering of fractures, in *Fractals in the Earth Sciences*, edited by C. C. Barton and P. R. La Pointe, pp. 141–178, Plenum Press, New York.

Bean, C. J., and J. McCloskey (1993), Power-law random behaviour of seismic reflectivity in boreholes and its relationship to crustal deformation models, *Earth Planet. Sci. Lett., 117*, 423–429.

Bean, C. J., and J. McCloskey (1995), Seismic constraints on statistical models of upper crustal heterogeneity, *First Break, 13*, 105–110.

Bean, C. J. (1996), On the cause of 1/f power spectral scaling in borehole logs, *Geophys. Res. Lett., 23*, 3119–3122.

Berkowitz, B., and A. Hadad (1997), Fractal and multifractal scaling measures of natural and synthetic fracture networks, *J. Geophys. Res., B, 102*, 12205–12218.

Bohnhoff, M., S. Baisch, and H.-P. Harjes (2004), Fault mechanisms of induced seismicity at the superdeep German Continental Deep Drilling Program (KTB) borehole and their relation to fault structure and stress field, *J. Geophys. Res., B, 109*, B02309, doi:02310.01029/02003JB002528.

Bonnet, E., O. Bour, N. E. Odling, P. Davy, I. Main, P. Cowie, and B. Berkowitz (2001), Scaling of fracture systems in geological media, *Rev. Geophys., 39*, 347–384.

Bos, R., S. de Waele, and P. M. T. Broersen (2002), Autoregressive spectral estimation by application of the Burg algorithm to irregularly sampled data, *IEEE Trans. Instrum. Meas., 51*, 1289–1294.

Broersen, P. M. T. (2000), Facts and fiction in spectral analysis, *IEEE Trans. Instrum. Meas., 49*, 766–772.

Broersen, P. M. T. (2002), Automatic spectral analysis with time series models, *IEEE Trans. Instrum. Meas., 51*, 211–216.

Broersen, P. M. T., S. de Waele, and R. Bos (2004), Application of autoregressive spectral analysis to missing data problems, *IEEE Trans. Instrum. Meas., 53*, 981–986.

Brudy, M. (1995), Determination of in-situ stress magnitude and orientation to 9 km depth at the KTB site, Ph.D. thesis, 196 pp., Universitat Karlsruhe, Karlsruhe, 10 November.

Brudy, M., and M. D. Zoback (1999), Drilling-induced tensile wall-fractures: Implications for determination of in-situ stress orientation and magnitude, *Int. J. Rock Mech. Min. Sci. Geomech. Abstr., 36*, 191–215.

Brudy, M., M. D. Zoback, K. Fuchs, F. Rummel, and J. Baumgärtner (1997), Estimation of the complete stress tensor to 8 km depth in the KTB scientific drill holes: Implications for crustal strength, *J. Geophys. Res., B, 102*, 18453–18475.

Castillo, D., and M. D. Zoback (1995), Systematic stress variations in the southern San Joaquin Valley and along the White Wolf fault: Implications for the rupture mechanics of the 1952 Ms 7.8 Kern County earthquake and contemporary seismicity, *J. Geophys. Res., B, 100*, 6249-6264.

Chen, C.-C., W.-C. Wang, Y.-F. Chang, and Y.-M. Wu (2006), A correlation between the b-value and the fractal dimension from the aftershock sequence of the 1999 Chi-Chi, Taiwan, earthquake, *Geophys. J. Int., 167*, 1215–1219.

Chéry, J., M. D. Zoback, and S. Hickman (2004), A mechanical model of the San Andreas fault and SAFOD Pilot Hole stress measurements, *Geophys. Res. Lett., 31*, doi:10.1029/2004GL019521.

Constable, C., and C. Johnson (2005), A paleomagnetic power spectrum, *Phys. Earth Planet. Inter., 153*, 61–73.

Cornet, F. H. (2007), Introduction to the special section on induced seismicity, *Int. J. Rock Mech. Min. Sci., 44*, 1077–1078.

Cornet, F. H., Th. Bérard, and S. Bourouis (2007), How close to failure is a granite rock mass at a 5 km depth?, *Int. J. Rock Mech. Min. Sci., 44*, 47–66.

Dahlheim, H.-A., H. Gebrande, E. Schmedes, and H. Soffel (1997), Seismicity and stress field in the vicinity of the KTB location, *J. Geophys. Res., B, 102*, 18493–18506.

Davis, J. C. (2002), *Statistics and Data Analysis in Geology*, 638 pp., Wiley, Indianapolis.

de Waele, S. (2003), Automatic inference from finite time observations of stationary stochastic signals, Ph.D. thesis, 205 pp., Technische Universiteit, Delft, 13 May.

Dolan, S. S., C. J. Bean, and B. Riollet (1998), The broad-band fractal nature of heterogeneity in the upper crust from petrophysical logs, *Geophys. J. Int., 132*, 489–507.

Frankel, A. (1991), High-frequency spectral falloff of earthquakes, fractal dimension of complex rupture, b value, and the scaling of strength on faults, *J. Geophys. Res., B, 96*, 6291–6302.

Ghil, M., M. R. Allen, M. D. Dettinger, K. Ide, D. Kondrashov, M. E. Mann, A. W. Robertson, A. Saunders, Y. Tian, F. Varadi, and P. Yiou (2002), Advanced spectral methods for climatic time series, *Rev. Geophys., 40*, doi:10.1029/2000RG000092.

Ghisetti, F. (2000), Slip partitioning and deformation cycles close to major faults in southern California: Evidence from small-scale faults, *Tectonics, 19*, 25–43.

Goff, J. A., and K. Holliger (1999), Nature and origin of upper crustal seismic velocity fluctuations and associated scaling properties: Combined stochastic analyses of KTB velocity and lithology logs, *J. Geophys. Res., B, 104*, 13169–13182.

Gutenberg, B., and C. F. Richter (1944), Frequency of earthquakes in California, *Bull. Seismol. Soc. Am., 34*, 185–188.

Hallgass, R., V. Loreto, O. Mazzella, G. Paladin, and L. Peitronero (1997), Earthquake statistics and fractal faults, *Phys. Rev. E, 56*, 1346–1356.

Hanks, T. C. (1992), Small earthquakes, tectonic forces, *Science, 256*, 1430–1432.

Hansen, A., J. Schmittbuhl, G. G. Batrouni, and F. A. de Oliveira (2000), Normal stress distribution of rough surfaces in contact, *Geophys. Res. Lett., 27*, 3639–3642.

Harris, R. A. (2004), Numerical simulations of large earthquakes: Dynamic rupture propagation on heterogeneous faults, *Pure Appl. Geophys., 161*, 2171–2181.

Hergarten, S. (2002), *Self-Organized Criticality in Earth Systems*, 272 pp., Springer, Berlin.

Hickman, S., and M. Zoback (2004), Stress orientations and magnitudes in the SAFOD Pilot Hole: Implications for the strength of the San Andreas fault at Parkfield: *Geophys. Res. Lett., 31*, doi:10.1029/2004GL020043.

Holliger, K., A. G. Green, and C. Juhlin (1996), Stochastic analysis of sonic logs from the upper crystalline crust: Methodology, *Tectonophysics, 264*, 341–356.

Huang, J., and D. L. Turcotte (1988) Fractal distributions of stress and strength and variations of b-value, *Earth Planet. Sci. Lett. 91*, 223–230.

Jarosinski, M. (1998), Contemporary stress field distortion in the Polish part of the Western Outer Carpathians and their basement, *Tectonophysics, 297*, 91–119.

Johnson, L. R., and R. M. Nadeau (2002), Asperity model of an earthquake: Static problem, *Bull. Seismol. Soc. Am., 92*, 672–686.

Jones, A. G. and Holliger, K., 1997, Spectral analyses of the KTB sonic and density logs using robust nonparametric methods, *J. Geophys. Res., B, 102*, 18391–18403.

Kanamori, H., and D. L. Anderson (1975) Theoretical basis of some empirical relations in seismology. *Bull. Seismol. Soc. Am., 65*, 1073–1095.

King, G. C. P. (1983) The accommodation of large strains in the upper lithosphere of the Earth and other solids by self-similar fault systems: the geometrical origin of b-value, *Pure Appl. Geophys.*, 121 761–815.

Kondrashov, D., and M. Ghil (2006), Spatio–temporal filling of missing points in geophysical data sets, *Nonlinear Processes Geophys., 13*, 151–159.

Kumar, P., and E. Foufoula-Georgiou (1997), Wavelet analysis for geophysical applications, *Rev. Geophys., 35*, 385–412.

Kurz, J. H., T. Jahr, and G. Jentzsch (2004), Earthquake swarm examples and a look at the generation mechanism of the Vogtland/Western Bohemia earthquake swarms, *Phys. Earth Planet. Inter., 142*, 75–88.

La Pointe, P. R. (2002), Derivation of parent fracture population statistics from trace length measurements of fractal fracture populations, *Int. J. Rock Mech. Min. Sci., 39*, 381–388.

La Pointe, P. R., T. Cladouhos, and S. Follin (2002), Development, application, and evaluation of a methodology to estimate distributed slip on fractures due to future earthquakes for nuclear waste repository performance assessment, *Bull. Seismol. Soc. Am., 92*, 923–944.

Lavallee, D., P. Liu, and R. J. Archuleta (2006), Stochastic model of heterogeneity in earthquake slip spatial distributions, *Geophys. J. Int., 165*, 622–640.

Leary, P. (1991), Deep borehole evidence for fractal distribution of fractures in crystalline rock, *Geophys. J. Int., 107*, 615–627.

Leary, P. C. (1997), Rock as a critical–point system and the inherent implausibility of reliable earthquake prediction, *Geophys. J. Int., 131*, 451–466.

Leary, P. C., T. L. Henyey, Y.-G. Li, and Anonymous (1988), Basement rock seismic reflectivity: Joint VSP and CDP imaging at Cajon Pass, California, deep drill site, *SEG Technical Program Expanded Abstracts, 7*, 184–186.

Leonardi, S. and H. -J. Kümpel (1998), Variability of geophysical log data and the signature of crustal heterogeneities at the KTB, *Geophys. J. Int., 135*, 964–974.

Line, C. E. R., R. W. Hobbs, and D. B. Snyder (1998), Estimates of upper–crustal heterogeneity in the Baltic Shield from seismic scattering and borehole logs, *Tectonophysics, 286*, 171–183.

Liu, Y., S. Crampin, and R. E. Abercrombie (1997), Shear–wave anisotropy and the stress field from borehole recordings at 2.5 km depth at Cajon Pass, *Geophys. J. Int., 129*, 439–449.

Lomb, N. R. (1976), Least squares frequency analysis of unevenly spaced data, *Astrophys. Space Sci., 39*, 447–462.

Lund, B., and M.D. Zoback (1999), Orientation and magnitude of in situ stress to 6.5 km depth in the Baltic Shield, *Int. J. Rock Mech. Min. Sci. Geomech. Abstr., 36*, 169–190.

Mai, P. M., and G. C. Beroza (2003), A hybrid method for calculating near-source, broadband seismograms: Application to strong motion prediction, *Phys. Earth Planet. Inter., 137*, 183–199.

Main, I. G., J. R. Henderson, P. G. Meredith, and P. R. Sammonds (1994), Self–organised criticality and fluid–rock interactions in the brittle field, *Pure and Appl. Geophys., 142*, 529–543.

Mandelbrot, B. B. (1967), How long is the coast of Britain?, *Science, 156*, 636–638.

Mandelbrot, B. B., and J. W. Van Ness (1968), Fractional Brownian motions, fractional noises and applications, *Soc. Industr. Appl. Math. Rev.*, *10*, 422-437.

Mariucci, M. T., A. Amato, R. Gambini, M. Giorgioni, and P. Montone (2002), Along–depth stress rotations and active faults: An example in a 5–km deep well of southern Italy, *Tectonics, 21*, 1021, doi:1010.1029/2001TC001338.

Marple, S. L. (1987), *Digital Spectral Analysis with Applications*, 492 pp., Prentice Hall, Englewood Cliffs, NJ.

Marsan, D. (2005), The role of small earthquakes in redistributing crustal elastic stress, *Geophys. J. Int., 163*, 141–151.

Marsan, D. (2006), Can coseismic stress variability suppress seismicity shadows? Insights from a rate-and-state friction model, *J. Geophys. Res., B, 111*, B06305, doi:10.1029/2005JB004060.

Marsan, D., and C. J. Bean (1999), Multiscaling nature of sonic velocities and lithology in the upper crystalline crust: evidence from the KTB Main Borehole, *Geophys. Res. Lett., 26*, 275–278.

Martin, C. D., and N. A. Chandler (1993), Stress heterogeneity and geological structures, *Int. J. Rock Mech. Min. Sci. Geomech. Abstr., 30*, 993–999.

Murray, J. R., and P. Segall (2005), Spatiotemporal evolution of a transient slip event on the San Andreas fault near Parkfield, California. *J. Geophys. Res., B, 110*, doi:10.1029/2005JB003651.

Neunhöfer, H., and T. Meier (2004), Seismicity in the Vogtland/Western Bohemia earthquake region between 1962 and 1998, *Stud. Geophys. Geod., 48*, 539–562.

Oglesby, D. D., and S. M. Day (2002), Stochastic fault stress: Implications for fault dynamics and ground motion, *Bull. Seismol. Soc. Am., 92*, 3006–3021.

Okada, Y. (1992) Internal deformation due to shear and tensile faults in a half-space: *Bull. Seismol. Soc. Am., 82*, 1018–1040.

Peška, P., and M. D. Zoback (1995), Compressive and tensile failure of inclined well bores and determination of in situ stress and rock strength, *J. Geophys. Res., B, 100*, 12791–12811.

Peyrat, S., K. B. Olsen, and R. Madariaga (2004), Which dynamic rupture parameters can be estimated from strong ground motion and geodetic data?, *Pure Appl. Geophys., 161*, 2155–2169.

Plumb, R.A., and S. H. Hickman (1985), A comparison between the four-arm dipmeter and the borehole televiewer in the Auburn geothermal well, *J. Geophys. Res., B, 90*, 5513–5521, 1985.

Rundle, J. B., D. L. Turcotte, and W. Klein (2000), Introduction, in *GeoComplexity and the Physics of Earthquakes*, edited by J. B. Rundle et al., pp. 1–3, American Geophysical Union, Washington, DC.

Rundle, J. B., D. L. Turcotte, R. Shcherbakov, W. Klein, and C. Sammis (2003), Statistical physics approach to understanding the multiscale dynamics of earthquake fault systems, *Rev. Geophys., 41*, doi:10.1029/2003RG000135.

Scargle, J. D. (1982), Studies in astronomical time series. II. Statistical aspects of spectral analysis of unevenly spaced data, *Astrophys. J., 263*, 835–853.

Sornette, D. (2000), *Critical phenomena in natural sciences: Chaos, fractals, self-organization, and disorder*, 434 pp., Springer, New York.

Schorlemmer, D., and S. Wiemer, and M. Wyss (2004), Earthquake statistics at Parkfield: 1. Stationarity of b values. *J. Geophys. Res., B, 109*, doi:10.1029/2004JB003234.

Schorlemmer, D., S. Wiemer, and M. Wyss (2005), Variations in earthquake–size distribution across different stress regimes, *Nature, 437*, 539–542.

Shamir, G. and M. D. Zoback (1992), Stress orientation profile to 3.5 km near the San Andreas fault at Cajon Pass, California, *J. Geophys. Res., B, 97*, 5059–5080.

Sleep, N. H. (2002), Self–organization of crustal faulting and tectonics, *Int. Geol. Rev., 44*, 83–96.

Steacy, S. J., J. McCloskey, C. J. Bean, and J. Ren (1996), Heterogeneity in a self-organised critical earthquake model, *Geophys. Res. Lett. 23*, 383–386.

Tessier, Y., S. Lovejoy, P. Hubert, and D. Schertzer (1996), Multifractal analysis and modeling of rainfall and river flows and scaling, causal transfer functions, *J. Geophys. Res., B, 101*, 26427–26440.

Tingay, M. R. P., R. R. Hillis, C. K. Morley, R. E. Swarbrick, and E. C. Okpere (2003), Variation in vertical stress in the Baram Basin, Brunei; tectonic and geomechanical implications, *Mar. Pet. Geol., 20*, 1201–1212.

Todoeschuck, J. P., O. G. Jensen, and S. Labonte (1990), Gaussian scaling noise model seismic reflection sequences: Evidence from well logs, *Geophysics, 55*, 480–484.

Townend, J., and M. D. Zoback (2000), How faulting keeps the crust strong, *Geology, 28*, 399–402.

Townend, J., and M. D. Zoback (2004), Regional tectonic stress near the San Andreas fault in central and southern California, *Geophys. Res. Lett.*, *31*, doi:10.1029/2003GL18918.

Turcotte, D. L. (1986), A fractal model for crustal deformation, *Tectonophysics, 132*, 261–269.

Turcotte, D. L. (1997), *Fractals and Chaos in Geology and Geophysics*, 2nd ed., 398 pp., Cambridge University Press, New York.

Velde, B., J. Dubois, D. Moore, and G. Touchard (1991), Fractal patterns of fractures in granites, *Earth Planet. Sci. Lett., 104*, 25–35.

Wesnousky, S. G. (1994), The Gutenberg–Richter or characteristic earthquake distribution, which is it? *Bull. Seismol. Soc. Am. 84*, 1940–1959.

Wesnousky, S. G., C. H. Scholz, K. Shimazaki, and T. Matsuda (1983), Earthquake frequency distribution and the mechanics of faulting, *J. Geophys. Res., B*, *88*, 9331–9340.

Wornell, G. W. (1996), *Signal Processing with Fractals: A Wavelet–based Approach*, 177 pp., Prentice Hall PTR, Upper Saddle River, NJ.

Wu, R. S., Z. Xu, and X. P. Li (1994), Heterogeneity spectrum and scale-anisotropy in the upper crust revealed by the German Continental Deep-Drilling (KTB) Holes, *Geophys. Res. Lett., 21*, 911–914.

Wyss, M., C. G. Sammis, R. M. Nadeau, and S. Wiemer (2004), Fractal dimension and b-value on creeping and locked patches of the San Andreas fault near Parkfield, California, *Bull. Seismol. Soc. Am., 94*, 410–421.

Zimmermann, G., H. Burkhardt, and L. Engelhard (2003), Scale dependence of hydraulic and structural parameters in the crystalline rock of the KTB, *Pure Appl. Geophys., 160*, 1067–1085.

Zoback, M., and J. H. Healy (1992), In situ stress measurements to 3.5 km depth in the Cajon Pass scientific research borehole: Implications for the mechanics of crustal faulting, *J. Geophys. Res., B, 97*, 5039–5057.

Zoback, M. D., and H.-P. Harjes (1997), Injection-induced earthquakes and crustal stress at 9 km depth at the KTB deep drilling site, Germany, *J. Geophys. Res., B, 102*, 18477–18491.

Zoback, M. D., D. Moos, L. Mastin, and R. N. Anderson (1985), Well bore breakouts and in situ stress, *J. Geophys. Res., B, 90*, 5523–5530.

Zoback, M.D., C.A. Barton, M. Brudy, D.A. Castillo, T. Finkbeiner, B.R. Grollimund, D.B. Moos, P. Peška, C.D. Ward, and D. Wiprut (2003), Determination of stress orientation and magnitude in deep wells, *Int. J. Rock Mech. Min. Sci., 40*, 1049–1076.

Zoback, M. L., M. D. Zoback, J. Adams, M. Assumpção, S. Bell, E. A. Bergman, P. Blümling, N. R. Brereton, D. Denham, J. Ding, K. Fuchs, N. Gay, S. Gregersen, H. K. Gupta, A. Gvishiani, K. Jacob, R. Klein, P. Knoll, M. Magee, J. L. Mercier, B. Müller, C. Paquin, K. Rajendran, O. Stephansson, G. Suarez, M. Suter, A. Udias, Z. H. Xu, and M. Zhizhin (1989), Global patterns of tectonic stress, *Nature, 341*, 291–298.

CHAPTER 3. PRESSURE-INDUCED STRESS ORIENTATION CHANGES IN BOUNDED RESERVOIRS

3.1 Abstract

We propose two models to explain the rotation of in situ horizontal principal stresses resulting from a pore pressure change on one side of an impermeable boundary—for example, an impermeable boundary at the edge of a depleted reservoir. In the first, we derive a simple analytical expression to estimate the amount of rotation based on the pore pressure change, the original horizontal differential stress magnitude, and the orientation of the boundary with respect to the original direction of the maximum horizontal compressive stress (S_{Hmax}). This model shows clearly that depletion will induce S_{Hmax} to become more parallel to the boundary. Reasonable values for the input parameters can result in very significant S_{Hmax} rotations. In the second model we use three-dimensional numerical modeling to investigate the effects of different reservoir shapes and properties. Our results show a strong interaction between many parameters that affect the predicted stress rotations. In situ stress magnitudes, rock property contrasts, reservoir shape, and boundary orientations are all significant. We examine the results of applying both models to two case studies of depleted fields—the Scott Field in the North Sea and the Arcabuz-Culebra field in northeastern Mexico. Using estimates of the original (i.e., unperturbed) stress state and the production history, we predict the fault orientation that would cause S_{Hmax} to rotate to directions observed using wellbore failure analysis, hydraulic fracture mapping, and shear velocity anisotropy studies. The analytical model provides a closer match to the mapped stress orientations, but the numerical model suggests that for certain ratios of pore pressure change to differential horizontal stress, the analytical model is likely to overpredict the amount of expected stress rotation.

3.2 Introduction

3.2.1 Motivation and Objectives

Knowledge of the local stress state is critical for optimizing well design, developing production strategies, and making informed drilling and completion decisions. Changes in stress throughout the life of a field are commonly observed. Stress reorientation in particular

has been reported in several locations around the world including the North Sea (Yale et al., 1994), Mexico (Wolhart et al., 2000) and the United States (Wright and Conant, 1995). With recent industry focus on re-engineering mature fields through practices such as hydraulic refracturing (e.g., Mouret, 2005), it is important to understand how and why such stress changes occur.

In this chapter we derive and test two models, one analytical and one numerical, that explain how a change in pore pressure will not only change the magnitudes of the in situ principal stresses through poroelastic effects, as expected, but can also cause those stresses to rotate. For the analytical model we use a simplified reservoir geometry, allowing us to make several simplifying assumptions in our calculations. In contrast, the numerical model allows us to explore a wider range of reservoir shapes and properties. Our overall goal is to provide a practical method for explaining observed depletion-induced stress rotations and, more importantly, for estimating potential ones.

3.2.2 Background

The theory of poroelasticity, in which pore pressure and elastic deformation are coupled, is based on work by Biot (1941). Application of poroelasticity theory to reservoirs has mainly been in the study of compaction due to fluid withdrawal. Geertsma (1957, 1973) modeled vertical deformation due to depletion of a thin, deep, horizontal layer with the same elastic properties as the surrounding material. Morita et al. (1989) expanded this work by developing numerical models for a disc-shaped reservoir under a wider range of conditions—e.g., when the reservoir is not necessarily thin, deep, or elastically the same as the material around it. Based on their results, they provided simple equations for calculating displacements, compaction, and stress magnitudes in both the reservoir and the caprock. In general, they found that the stress change is considerably greater when Young's modulus in the reservoir is significantly less than in the surrounding rock, with a greater effect at the edge of the reservoir than at the center. They concluded that a uniaxial strain assumption is appropriate only if the reservoir Young's modulus is 0.2 to 1.5 times that of the surrounding rock, and the reservoir is both deep and laterally extensive.

Lorentz et al. (1991) derived a solution for total horizontal stress under uniaxial strain and an increase in pore pressure, but they did not derive the *change* in stress (ΔS_H) as a function of pore pressure change (ΔP_p), which can be expressed as

$$\Delta S_H = A\Delta P_p . \qquad \text{(E3–1)}$$

We refer to A, the ratio of stress change to pore pressure change, as the stress–depletion response. Engelder and Fischer (1994) derived an expression for A in an infinite, horizontal layer under isothermal conditions with no horizontal strain and a constant vertical stress,

$$A = \alpha \frac{(1-2\nu)}{(1-\nu)}, \qquad \text{(E3–2)}$$

where α is the Biot effective stress coefficient and ν is Poisson's ratio. Their resulting prediction of uniform subsidence and no horizontal strain above the reservoir, however, was in contrast to common observations of depletion-induced seismicity. Segall (1989, 1992) used a disk-shaped reservoir and provided a much better match to field experience. Based on inclusion theory by Eshelby (1957) and Mura (1982), Segall and Fitzgerald (1998) looked more at the issue of reservoir shape and found that for an ellipsoidal reservoir under isothermal conditions, the stress–depletion response is a function of both the Biot coefficient and the relative lengths of the reservoir axes. For a very thin ellipse, which approximates a laterally extensive reservoir, the solution reduces to that of Eqn. E3–2. Rudnicki (1999) extended their analysis by allowing the ellipsoidal reservoir to have different elastic properties than the surrounding rock.

Empirically, the stress-depletion response is generally in the range of 0.5 to 1.0, and under uniaxial strain and no faulting, the maximum (S_{Hmax}) and minimum (S_{hmin}) horizontal principal stresses change by the same amount (Addis, 1997a, 1997b; Segall and Fitzgerald, 1998). In an active faulting environment, the response may be dependent on the type and strength of nearby faults (Addis et al., 1994). Sayers (2006) describes how the stress–depletion response can be anisotropic due to either reservoir shape or local heterogeneities and suggests using repeat seismic measurements to constrain its value(s) in a given field.

While these studies have been carried out in order to understand changes in stress magnitudes as a result of pore pressure changes, almost no work has been done to examine changes in stress directions, yet anecdotal reports of variations in stress orientations throughout the life of a field are not uncommon.

3.2.3 Field Cases

While there is plenty of data on pressure-induced stress magnitude changes (e.g., see Addis, 1997a), we can find very few data sets suitable for carefully examining pressure-

induced stress rotations. In order to quantify the relationship between pressure and stress reorientation, we need not only reliable before-and-after stress directions, but also a well-defined initial stress state for the area (before any pore pressure change), a good record of how much the pore pressure has changed, and mapped faults and/or reservoir boundaries. So far we have identified two suitable case studies in the published literature.

Scott Field

Scott Field is a sand and shale reservoir in the Witch Ground Graben in the British North Sea. While in a normal faulting regime, the field is cut by several sealing faults that have not been active since the Upper Cretaceous. Stress orientations were measured in individual wells from both stress-induced wellbore failures (Figure 3–1, dashed arrows) and shear-velocity anisotropy measured on core samples (Figure 3–1, solid arrows) (Yale et al., 1994). The two data types show good agreement at nearby wells even though the failure-derived orientations are mainly from the shales and the anisotropy-derived orientations are mainly from the sands. The results reveal that local stresses, while quite consistent within individual wells, are at a wide range of angles to the regional north-northwest–south-southeast S_{Hmax} azimuth.

The Scott Field has been heavily depleted, with production reducing the pore pressure 60 MPa, from approximately 65 MPa initially to about 5 MPa. The estimated overburden and least principal horizontal stress are 98 MPa and 33 MPa, respectively.

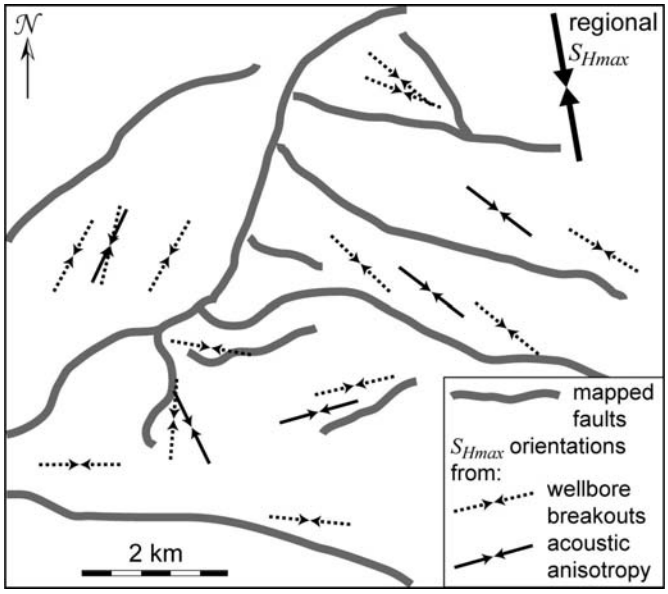

Figure 3–1. S_{Hmax} orientations and mapped faults in the Scott Field, North Sea. Stress data come from wellbore failure (dashed arrows) and acoustic anisotropy (solid arrows). (after Yale et al., 1994)

Arcabuz-Culebra

The Arcabuz and Culebra Fields are adjacent to each other in the center of the Burgos Basin, onshore in northeast Mexico. The production target is a high porosity (10–15%), low permeability (0.01–0.1 mD) gas reservoir in Eocene-Paleocene, shallow marine sands interbedded with shale. The reservoir is fault bounded and compartmentalized by north-south trending syn-depositional growth faults that formed under east-southeast–west-northwest extension (Boulter et al., 1998; Vázquez et al., 1997; Wolhart et al., 2000). Although the field is one of the most productive in the Burgos Basin, the reservoir's low permeability requires hydraulic fracture stimulation to enhance recovery. A comprehensive analysis of in situ stress in the field, performed to optimize hydraulic fracturing efforts, revealed highly variable stress directions (Wolhart et al., 2000). S_{Hmax} azimuths in individual wells, measured from either wellbore failure or tiltmeter mapping of hydraulic fractures, were frequently rotated from the northeast–southwest regional stress direction to be more parallel to nearby faults (Figure 3–2). This was more pronounced in the Arcabuz Field, which had been under production longer, and therefore experienced more depletion, than the Culebra Field.

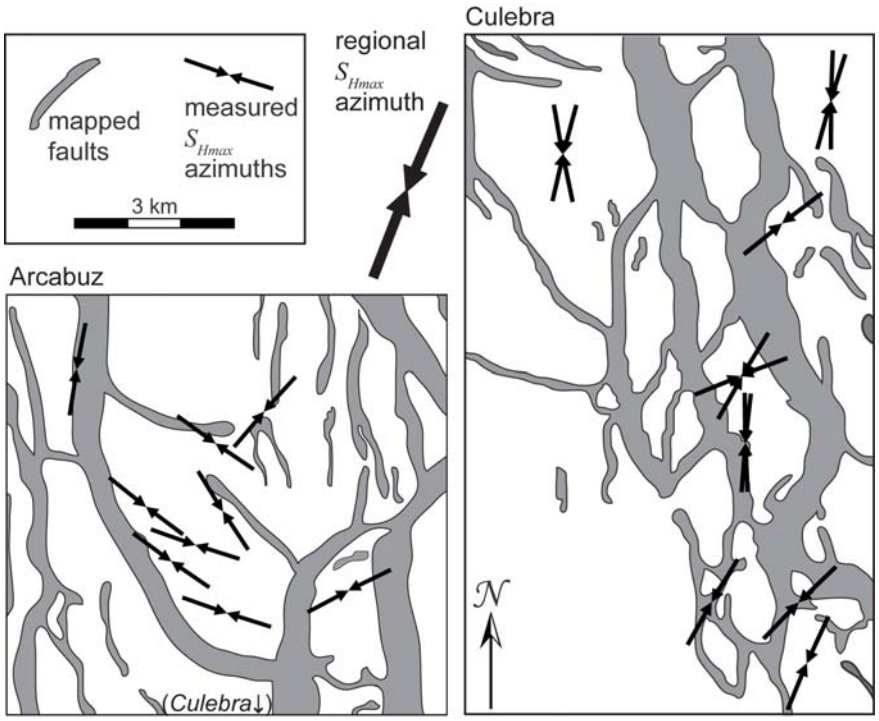

Figure 3–2. Observations of post-production S_{Hmax} azimuths in the Arcabuz and Culebra gas fields in the Burgos Basin, Mexico, superimposed on mapped faults. The width of the faults indicates lateral offset of the top or bottom reservoir boundary due to fault slip. Double arrows in the Culebra Field indicate stress directions from both wellbore failure and hydraulic fractures. (after Wolhart et al., 2000)

The unperturbed stress state in the Arcabuz field was strike-slip with S_{Hmax} oriented 21° and only slightly higher in magnitude than the overburden (Wolhart et al., 2000). The original, differential horizontal stress magnitude was approximately 0.2 psi/ft, and pore pressure was 0.9 psi/ft at most. Depletion estimates up to the time the hydraulic fracturing study was carried out range from 0.09 to 0.4 psi/ft.

3.3 Analytical Model

3.3.1 Model Development

As described in the previous section, the exact value and analytical form of the stress–depletion response for a given reservoir depend on the reservoir depth, geometry, and tectonic setting as well the poroelastic properties of the reservoir and its surroundings. For a simple case in which the reservoir is laterally extensive (i.e., no horizontal strain), homogeneous, and isotropic with elastic properties that do not contrast strongly with the surrounding rock, the total vertical stress change due to depletion (or injection) is very small (Hettema et al., 2000) and can be assumed to be zero. While the horizontal stress magnitudes are expected to change according to the stress–depletion response given in Eqn. E3–2, S_{Hmax} and S_{hmin} will change by the same amount, and therefore no change in horizontal stress orientation is expected.

We extend this simple model to include the potential effects of a vertical boundary, such as an impermeable fault, separating the region experiencing a pore pressure change from one in which pore pressure remains constant. Our model geometry is illustrated in Figure 3–3. We

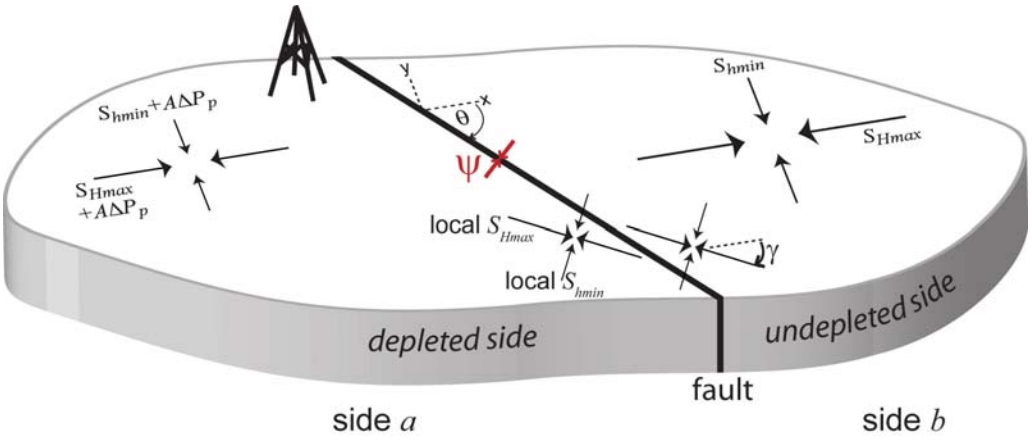

Figure 3–3. Model geometry: The vertical stress is assumed to be a principal stress, and the regional maximum horizontal principal compressive stress (S_{Hmax}) is in the x-direction. An impermeable fault is at an angle θ (clockwise positive) from the x-axis. The difference in pore pressure on either side of the fault induces a normal traction (ψ, red arrows), which changes the fault-normal stress by $A\Delta P_p$.

assume that the vertical stress is a principal stress, and the boundary is at an angle θ from the direction of the regional maximum horizontal principal compressive stress, S_{Hmax}. The fault separates side *a*, which experiences a change in pore pressure (ΔP_p = depleted P_p − initial P_p), from side *b*, which does not. According to Eqn. E.3–1, both of the horizontal stress magnitudes in side *a* change by $A\Delta P_p$, while there is no change in stress magnitudes on side *b*. The difference in pore pressure on either side imposes a normal traction, ψ, also of magnitude $A\Delta P_p$ (Segall and Fitzgerald, 1998, after Eshelby, 1957) on the fault. Since the normal stress must be continuous across the fault, both sides experience the same change in normal stress, although it decays rapidly with distance from the fault.

Following the approach developed by Sonder (1990), the complete, new stress state near the fault can be found by superimposing the uniaxial normal stress perturbation ($\psi = A\Delta P_p$) onto the background stress state. First, we find the magnitudes of the individual components of the normal stress perturbation in the original, *x*–*y* coordinate system by rotating the perturbation axis through the angle θ (Jaeger and Cook, 1979):

$$\psi_x = \psi \sin^2 \theta = \frac{A\Delta P_p}{2}(1 - \cos 2\theta) \tag{E3–3}$$

$$\psi_y = \psi \cos^2 \theta = \frac{A\Delta P_p}{2}(1 + \cos 2\theta) \tag{E3–4}$$

$$\psi_{xy} = -\frac{A\Delta P_p}{2}\sin 2\theta \tag{E3–5}$$

The resultant stress components near the fault on side *a* (the depleted side) are then

$$S_x{}^a = S_{\text{Hmax}} + A\Delta P_p + \psi_x = S_{\text{Hmax}} + A\Delta P_p + \frac{A\Delta P_p}{2}(1 - \cos 2\theta) \tag{E3–6}$$

$$S_y{}^a = S_{\text{hmin}} + A\Delta P_p + \psi_y = S_{\text{hmin}} + A\Delta P_p + \frac{A\Delta P_p}{2}(1 + \cos 2\theta) \tag{E3–7}$$

$$S_{xy}{}^a = \psi_{xy} = -\frac{A\Delta P_p}{2}\sin 2\theta \tag{E3–8}$$

and near the fault on side *b* (the undepleted side) are

$$S_x{}^b = S_{\text{Hmax}} + \psi_x = S_{\text{Hmax}} + \frac{A\Delta P_p}{2}(1 - \cos 2\theta) \tag{E3–9}$$

$$S_y{}^b = S_{\text{hmin}} + \psi_y = S_{\text{hmin}} + \frac{A\Delta P_p}{2}(1+\cos 2\theta) \qquad \text{(E3–10)}$$

$$S_{xy}{}^b = \psi_{xy} = -\frac{A\Delta P_p}{2}\sin 2\theta\,. \qquad \text{(E3–11)}$$

The presence of non-zero shear stress (Eqns. E3–8 and E3–11) indicates that x and y are no longer principal stress directions. The new principal stress coordinate system, rotated at some angle γ from the original x–y coordinate system, near the fault can be found by

$$\gamma = \frac{1}{2}\tan^{-1}\left[\frac{2S_{xy}}{S_x - S_y}\right] \qquad \text{(E3–12)}$$

(Jaeger and Cook, 1979). The rotation is the same on both sides of the fault because, from Eqns. E3–6 through E3–11, $S_{xy}{}^a = S_{xy}{}^b$ and $S_x{}^a - S_y{}^a = S_x{}^b - S_y{}^b$. Therefore,

$$\gamma = \frac{1}{2}\tan^{-1}\left[\frac{-A\Delta P_p \sin 2\theta}{(S_{\text{Hmax}} - S_{\text{hmin}}) - A\Delta P_p \cos 2\theta}\right] \qquad \text{(E3–13)}$$

If we define a new parameter, q, as the negative ratio of pore pressure change to the horizontal differential stress,

$$q = \frac{-\Delta P_p}{(S_{\text{Hmax}} - S_{\text{hmin}})}, \qquad \text{(E3–14)}$$

then we can simplify Eqn. E3–13 to

$$\gamma = \frac{1}{2}\tan^{-1}\left[\frac{Aq\sin 2\theta}{1 + Aq\cos 2\theta}\right]. \qquad \text{(E3–15)}$$

In this convention, q is positive for depletion, and γ, like θ, is clockwise positive. One can see from Eqns. E3–14 and E3–15 that the stress reorientation depends on 1) the relative magnitudes of the pore pressure change and original horizontal differential stress, 2) the orientation of the fault relative to the original S_{Hmax} azimuth, and 3) the stress–depletion response, A.

3.3.2 Generalized Results

Figure 3–4 illustrates the amount of stress rotation expected for values of q from 0 to 10 near faults of any azimuth and for two different stress–depletion responses: A = 0.67, corresponding to Eqn. E3–2 with α = 1 and ν = 0.25, and A = 1, representing the maximum

possible ratio of stress change to pore pressure change. The sign of γ (the stress rotation), is the same as θ (the angle from S_{Hmax} to the fault), so for positive q (depletion), S_{Hmax} will rotate to be more parallel to the fault. For small q the predicted stress rotations are generally small. If, however, the pore pressure drop is similar to, or greater than the initial horizontal differential stress ($q \geq \sim 1$), the amount of stress reorientation can be quite large, particularly for larger values of A. Once q reaches 10, the model predicts that S_{Hmax} will rotate to be totally parallel to the boundary. Relatively high q-values are likely to be encountered in overpressured, normal faulting regions when a reservoir experiences significant depletion. In such areas, the horizontal differential stress will be small as both horizontal stress magnitudes must be higher than the pore pressure but lower than the overburden stress.

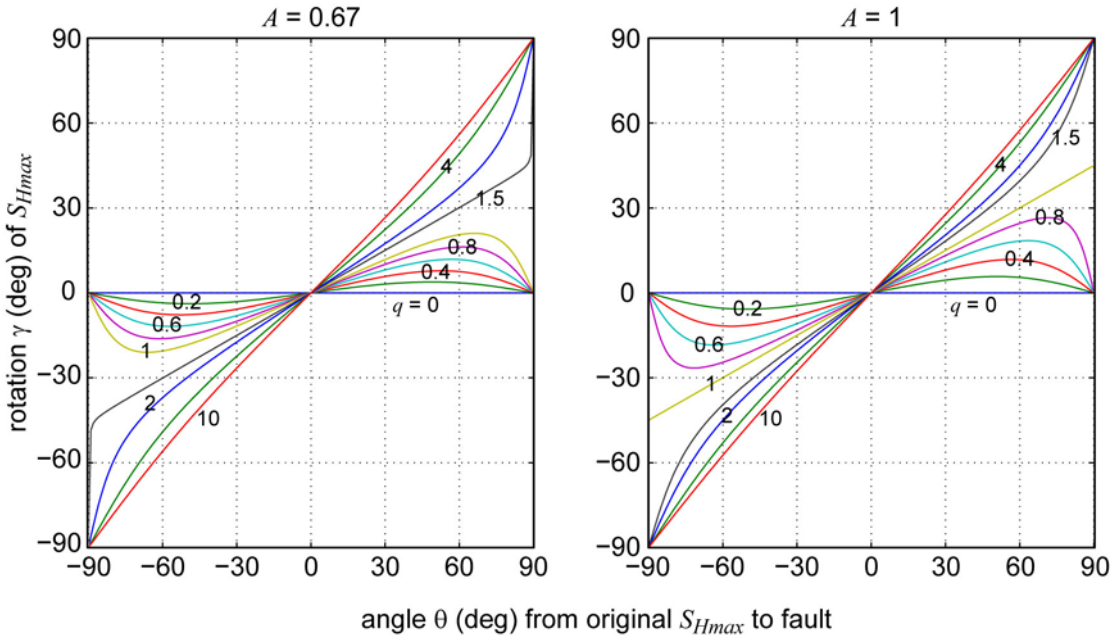

Figure 3–4. Generalized S_{Hmax} rotation predicted by our analytical model for stress–depletion responses (A) equal to 0.67 (left) and 1.0 (right) and depletion with q ranging from 0 to 10.

3.3.3 Case Studies

Scott Field

Since in a normal faulting regime S_{Hmax} is the intermediate stress, its magnitude in the Scott Field is in the range 34 MPa to 97 MPa ($S_{hmin} < S_{Hmax} < Sv$, see Section 3.2.3). Therefore q can range anywhere from 1.9 to 60. Figure 3–5 presents our analytical modeling results using these parameters. The red, dashed lines on the fault map represent the predicted fault orientations that would explain the observed stress direction in each well using q = 1.9 and A =

0.67 (note in Figure 3–4 that for q greater than about 1.5 the difference in the solutions for A = 0.67 and A = 1 is small). Nearly all of the predicted fault orientations closely match the strikes of nearby mapped faults.

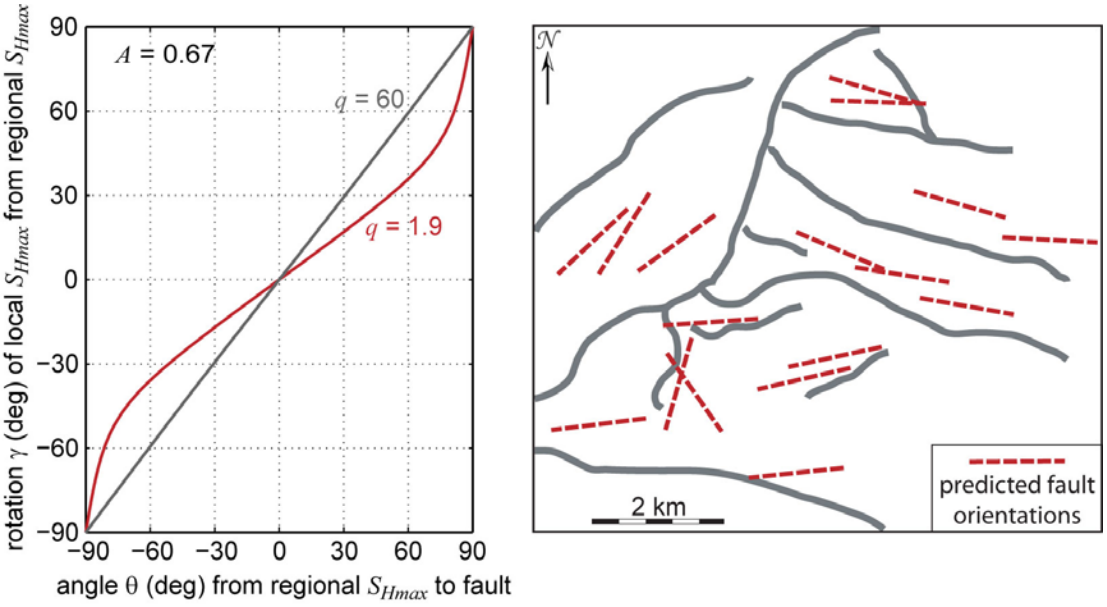

Figure 3–5. Results from applying our analytical model to the Scott Field. Theoretical rotations as a function of fault orientation for a stress–depletion response (A) of 0.67 and q equal to 1.9 and 60 are shown on the left. Predicted fault orientations (red, dashed lines on right) are shown that can explain the observed stress reorientation at each well if q = 1.9.

Arcabuz Field

Using an original, differential horizontal stress magnitude of 0.2 psi/ft, and depletion ranging from 0.09 to 0.4 psi/ft (see Section 3.2.3), q for the Arcabuz Field can range from 0.45 to 2. Figure 3–6 shows the resulting range of stress rotation amounts for a stress-depletion response of A = 0.67 (left-hand plot). For q = 0.45, the maximum expected stress reorientation, γ, is only about 10°, which can not account for observed rotations that vary from -75° to 85° (Fig. 3–2). For q = 2, however, estimated stress rotations do span the observed range. The predicted fault orientations that, according to the q = 2 model, would explain the observed stress directions are shown on the fault map (right-hand plot). At most of the wells, a fault exists nearby with the predicted orientation, even if it is not the closest (or largest) mapped fault.

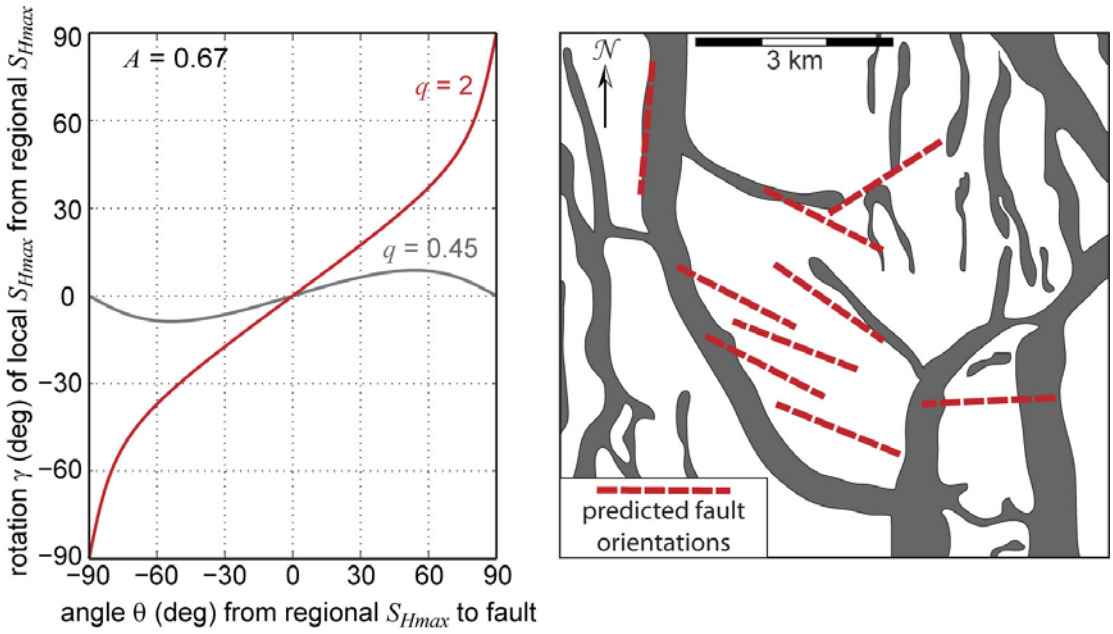

Figure 3–6. Results from applying our analytical model to the Arcabuz Field. Theoretical rotations as a function of fault orientation for a stress–depletion response (A) of 0.67 and q equal to 0.45 and 2 are shown on the left. Predicted fault orientations (red, dashed lines on right) are shown that can explain the observed stress reorientation at each well if $q = 2$.

3.4 Numerical Model

Inherent in the analytical model described in the previous section are several underlying assumptions. Some of these, such as assuming that the faults remain sealed during the change in pore pressure, will be addressed later when we discuss the implications of our work. In this section we look specifically at the geometry and elastic properties of the reservoir and present a three-dimensional, numerical model that allows us to remove the restrictions regarding them that are present in the analytical model.

The analytical model is based on a thin, laterally extensive reservoir that experiences no horizontal strain, has a constant vertical stress, and is the same elastically as its surroundings, from which it is separated by a vertical, impermeable boundary. Although Morita et al. (1989) demonstrate through finite element modeling that vertical stress is highly dependent on reservoir thickness, Segall and Fitzgerald (1998) show that vertical stress changes are relatively small when the lateral extent of the reservoir is at least 5–10 times its thickness. Deviation from the uniaxial strain assumption increases with increasing reservoir thickness. In addition, Morita et al. (1989) show that if Young's modulus in the reservoir is within 0.2 to 1.5 times that outside the reservoir, then the modulus contrast does not significantly affect the solution.

The primary reason we wanted to extend our analysis, despite the validation these case studies provide for our previous model, was that we wanted to closely examine the effect of reservoir shape. Specifically, we wanted to simulate some other, geologically reasonable reservoir types such as small fault blocks and channel deposits. Our secondary goal was to see how the effects of the pore pressure change decay with distance from the impermeable boundary. To this end, we created a three-dimensional, finite element model based on Eshelby's (1957) inclusion theory using COMSOL Multiphysics™. We verified the model results by comparing them to solutions from Eshelby (1957) and Segall and Fitzgerald (1998) for specific cases. We then examined several additional cases including different shapes and physical properties. Finally, we used the model to revisit the Scott Field and Arcabuz case studies.

3.4.1 Model Development

Physics

In a classic paper, Eshelby (1957) derived an analytical solution for the state of stress both inside and outside of an inclusion or heterogeneity under an applied load (an inclusion has the same elastic properties as its surroundings, while those for a heterogeneity are different). Conceptually, the solution is divided into several steps. In the first step, the inclusion is allowed to deform without any outside constraints, as if it had been completely removed from the surrounding material. At this point a reference state is defined in which stress and strain inside the inclusion are set to zero. In the second step, a traction is applied to the outside of the deformed inclusion in order to restore it to its original shape, inducing a stress (called the transformation stress) inside the inclusion. Importantly, the transformation stress is 1) opposite and equal in magnitude to the stress induced in the inclusion (which was later set to zero) in the first step, and 2) uniform throughout the inclusion if the inclusion is an ellipsoid. The inclusion is then figuratively "welded" back into the matrix, and the traction on its boundary becomes a layer of body force within the combined solid. At this point total stress in the inclusion is simply the transformation stress, and there is still no stress in the surrounding material. This is followed by the third and final step, in which an equal and opposite body force is applied to the boundary layer in order to cancel out the one created by the welding. This additional force causes strain in both the inclusion and matrix, with deformation in each being constrained by its connection to the other; thus, the stresses induced in this step are appropriately called the constrained stresses. The total stresses inside the

inclusion are its constrained stress plus the transformation stress, while the total stress outside is just its constrained stress.

In our COMSOL Multiphysics model, it is only necessary to perform Eshelby's first step to determine the transformation stress, which is simply taken as the opposite of the stress induced by the unconstrained deformation. Eshelby's third step, calculation of the constrained stresses, is performed by starting with the undeformed and welded geometry, applying traction on the boundary between matrix and inclusion, and then letting both deform. For each step, COMSOL first calculates displacements as a function of applied loads, boundary conditions and material properties, then calculates the full strain tensor from the displacements, and then converts strains to stresses. Finally, the total induced stresses are found by superimposing the transformation stress on the constrained stress in the inclusion only.

In the analysis that follows, we first use our model to examine the stresses induced by changing the pore pressure in inclusions of several different shapes in the absence of a remote applied stress. We then look at the effects of different elastic properties in the inclusion and matrix. Finally, we revisit our case studies by superimposing the total induced stresses in both the inclusion and matrix onto a pre-existing, in situ stress state. (A full COMSOL model report, which would allow for reproduction of our model by any experienced COMSOL user, is provided in Section 3.10 as an appendix.)

Shapes

As Eshelby (1957) noted, if the inclusion being modeled is an ellipsoid, the transformation stress throughout the inclusion is uniform. We take advantage of this fact to substantially simplify our modeling. Rather than having to calculate and superimpose two spatially variable stresses inside the reservoir, we can simply add the constant transformation stress to the spatially varying constrained stress. This said, however, we still want to approximate some realistic reservoir shapes. As a result we ran our model on three different ellipsoids, as illustrated in Figure 3–7. The first (Fig. 3–7a) is a thin, oblate spheroid, which we use to match the flat-lying, laterally extensive reservoir approximation used by Segall and Fitzgerald (1998). In this geometry, the x and y dimensions are each ten times the vertical dimension. The second shape (Fig 3–7b) is a modification of the first to examine the effects of reservoir thickness. It is meant to purposely violate the assumption that there is an insignificant change in vertical stress, which Segall and Fitzgerald (1998) found to be appropriate when the horizontal axes were at least 5 to 10 times longer than the vertical. The shape we use is a regular oblate spheroid where the two horizontal axes are only one-third

larger than the vertical, and it is meant to roughly approximate, for example, a structural trap or laterally restricted fault block. The final geometry (Fig. 3–7c) is an elongate, thin ellipsoid where the *x*:*y*:*z* axis ratio is 5:50:1. This is meant to represent, for example, a channel deposit. Each shape is embedded in a much larger, rectangular matrix with boundary conditions that simulate a semi-infinite half-space with a free surface on the top.

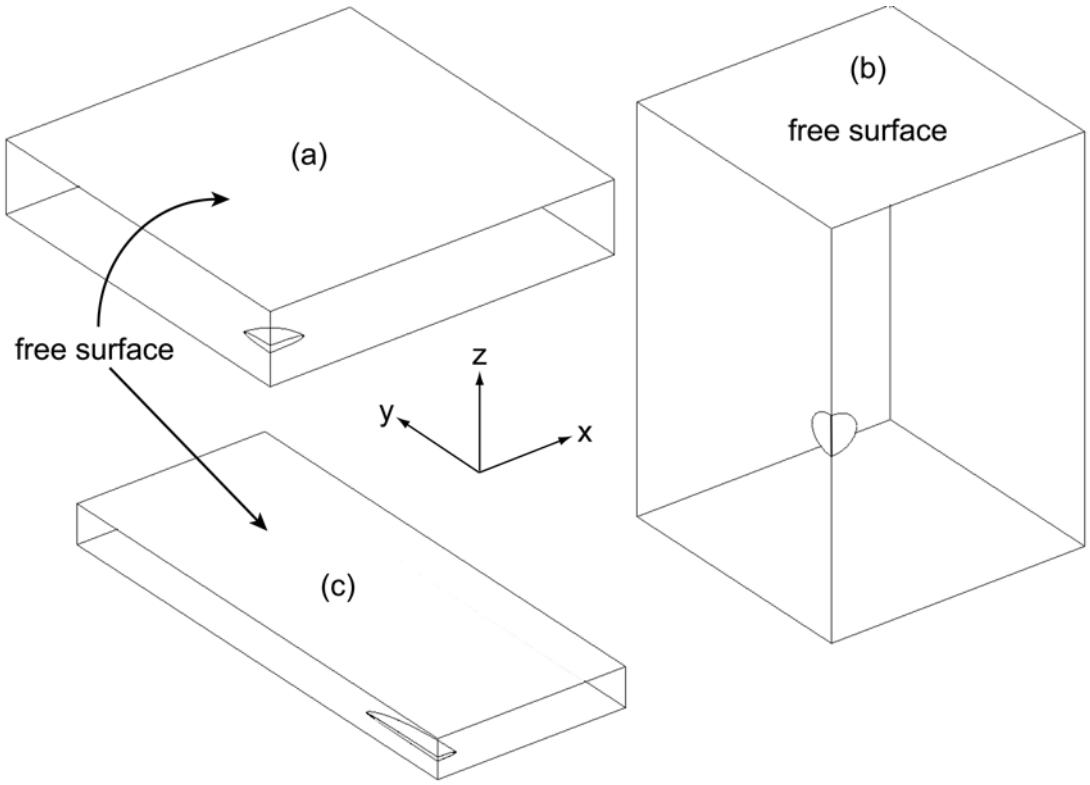

Figure 3–7. The geometries of our three numerical models. The embedded ellipsoids represent the reservoirs embedded in a half-space with a free surface on top.

3.4.2 Generalized Results

Before examining our individual case studies, it is instructive to look at only the induced stresses—that is, the stresses induced in the absence of any pre-existing in situ stress—caused by depleting each of the three modeled shapes. The elastic parameters needed for both the inclusion (the reservoir) and matrix are the Biot coefficient, Young's modulus, Poisson's ratio, and bulk density. For our generic simulations we used 0.75, 15 GPa, 0.25, and 2750 kg/m^3, respectively, for these values.

Figures 3–8 through 3–10 present the induced principal stress magnitudes (S_I is most compressive/least extensional) and directions for each of the reservoir shapes shown in two

planar sections through the model geometry. For the thin disc-shaped reservoir and thick reservoir, these are the horizontal plane through the vertical center of the reservoir and a vertical plane extending radially from the vertical axis. Since the models are radially symmetric, the azimuthal direction of the vertical plane does not matter. For the long, narrow reservoir the horizontal plane is shown as in the previous examples, but the vertical plane is oriented parallel to the *x*-axis. Induced stress magnitudes are quantified as a percentage of the pore pressure change, ΔP_p, and stress directions are indicated with large tick-marks (a small square indicates stress oriented normal to the plane shown). Stress directions are not shown where the induced stress magnitude is less than 1% ΔP_p in order to emphasize the spatial limit of significant induced stresses away from the reservoir boundary.

Thin, Disc-shaped Reservoir

On the horizontal plane through the middle of the disc-shaped reservoir (Fig. 3–8, left-hand plots), strongly extensional horizontal stresses are induced in both the tangential (parallel to the boundary) and radial (perpendicular to the boundary) directions. These are equal and approximately 50% of ΔP_p, in agreement with the prediction of Segall and Fitzgerald (1998, Eqns. 7 and 10) where the induced horizontal stresses inside should be about 46% of ΔP_p. A slightly extensional vertical stress equal to about 8% ΔP_p is also induced inside the reservoir, again corresponding with a predicted stress change of 7.8% using Segall and Fitzgerald's (1998) solution. Just outside the lateral edge of the reservoir on the horizontal plane, where the boundary is essentially vertical and we can compare the model results to our analytical model predictions, there is a significant vertical compression (nearly 20% of ΔP_p), a small tangential compression, and a moderate radial extension. This difference in horizontal induced stresses will cause any pre-existing stresses to become increasingly compressional parallel to the boundary, thus S_{Hmax} will rotate to be more parallel to the boundary as our analytical model predicts.

Stresses in the vertical plane (Fig. 3–8, right-hand plots) illustrate the important insights that the 3-D numerical model can provide. While one principal stress remains horizontal everywhere and parallel to the reservoir outer edge, the overall stress state is significantly inclined for a considerable distance above, below, and laterally away from the reservoir except along the horizontal plane through the geometry center. Note, however, that the magnitudes of the induced stresses are very low in these regions. Immediately above the center of the reservoir, for example, the horizontal stresses are both slightly compressive (just over 3% ΔP_p), and the vertical stress is slightly extensional. Once more our results agree with Segall

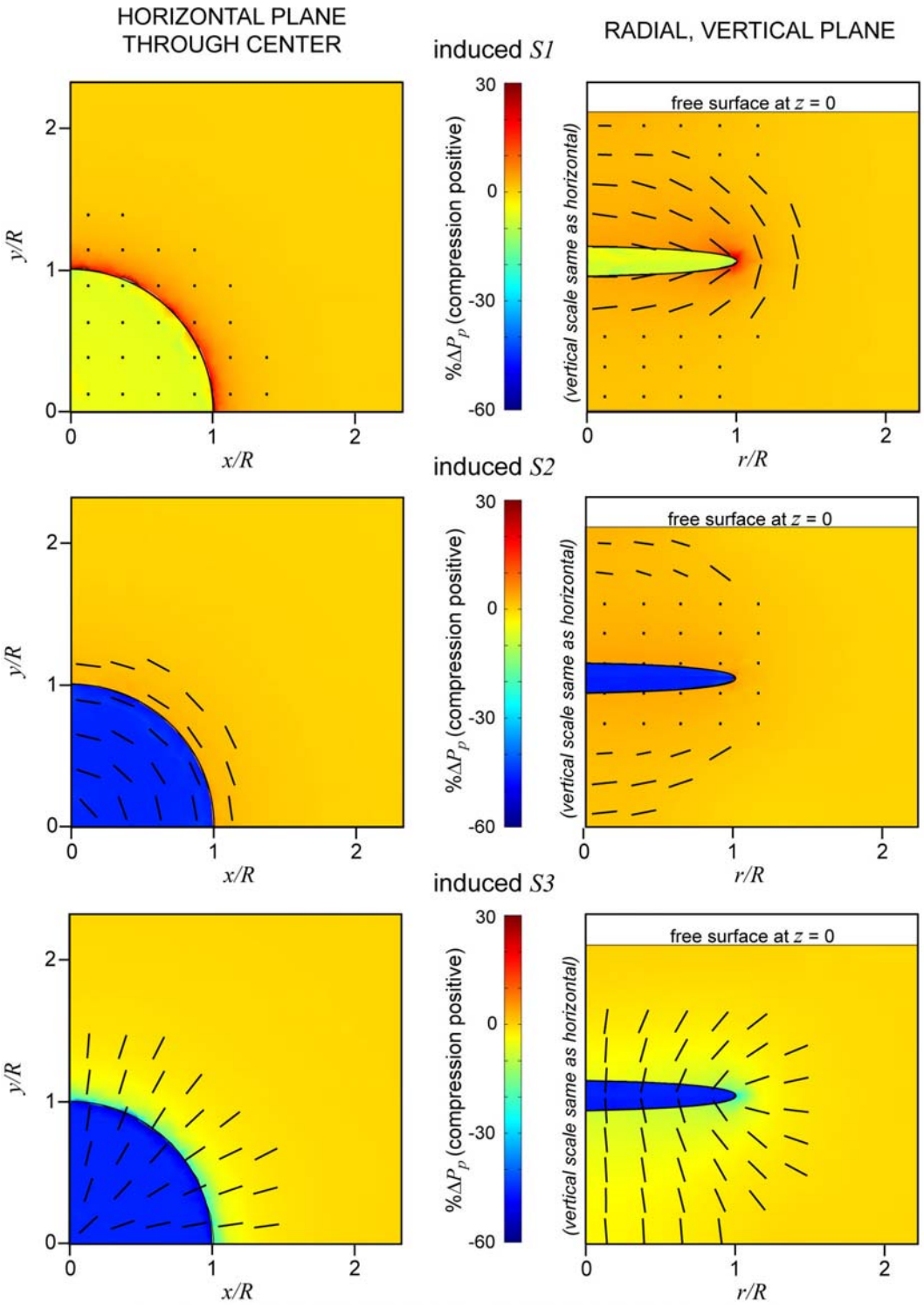

Figure 3–8. Stresses induced by depleting a disc-shaped reservoir by $-\Delta P_p$. Stress directions are shown with large tick-marks (dots indicate stress oriented into the plane shown). S_1 is the most compressive, and S_3 the least compressive, principal stress.

and Fitzgerald (1998, Eqn. 14), which predicts horizontal compression equal to 3.9% ΔP_p at this location.

Thick Reservoir

For a thicker reservoir the results are quite different (Fig. 3–9). Through the center of the reservoir the induced horizontal extension is slightly smaller than in the thin reservoir case, but the induced vertical extension is relatively large, comparable to the horizontal induced stresses. Outside of the reservoir the induced stresses decay more slowly with distance from the boundary. As in the previous model, the stress state above and below the reservoir is significantly inclined, but the induced stress magnitudes are several times their values for the thinner geometry.

The contrast in the horizontal stresses just outside the reservoir boundary in the horizontal plane through the reservoir center is similar to the thin reservoir results; stress induced parallel to the boundary (S_2) is compressive, and stress induced perpendicular to it (S_3) is extensional. Thus, as in the previous case, a pre-existing maximum horizontal compressive stress will rotate to be more parallel to the boundary. The significantly greater magnitude and lateral extent of this contrast, however, will make the effect greater and present further from the boundary than in the thin reservoir case.

Thin, Elongated Reservoir

Model results from our approximation of a thin channel are shown in Figure 3–10. This case is very different from the radially symmetric reservoir models. Inside the reservoir the horizontal stress magnitudes are no longer equal; maximum extension is approximately 50% of ΔP_p and oriented along the channel long axis (parallel to the channel edge), while extension perpendicular to the channel edge is around 40–45% ΔP_p. The vertical induced stress is relatively small, around 10% ΔP_p or less, and is also extensional. Outside the reservoir there is a small extension induced perpendicular to the reservoir boundary and a small induced vertical compression.

Just outside the reservoir boundary, the extension parallel to the boundary will cause a rotation of maximum horizontal compressive stress similar to the previous two cases and our analytical model. Inside the reservoir, however, the significant horizontal extension along the reservoir long axis will cause the opposite sense of rotation—that is, the direction of maximum horizontal compression is predicted to become more *perpendicular* to the reservoir boundary.

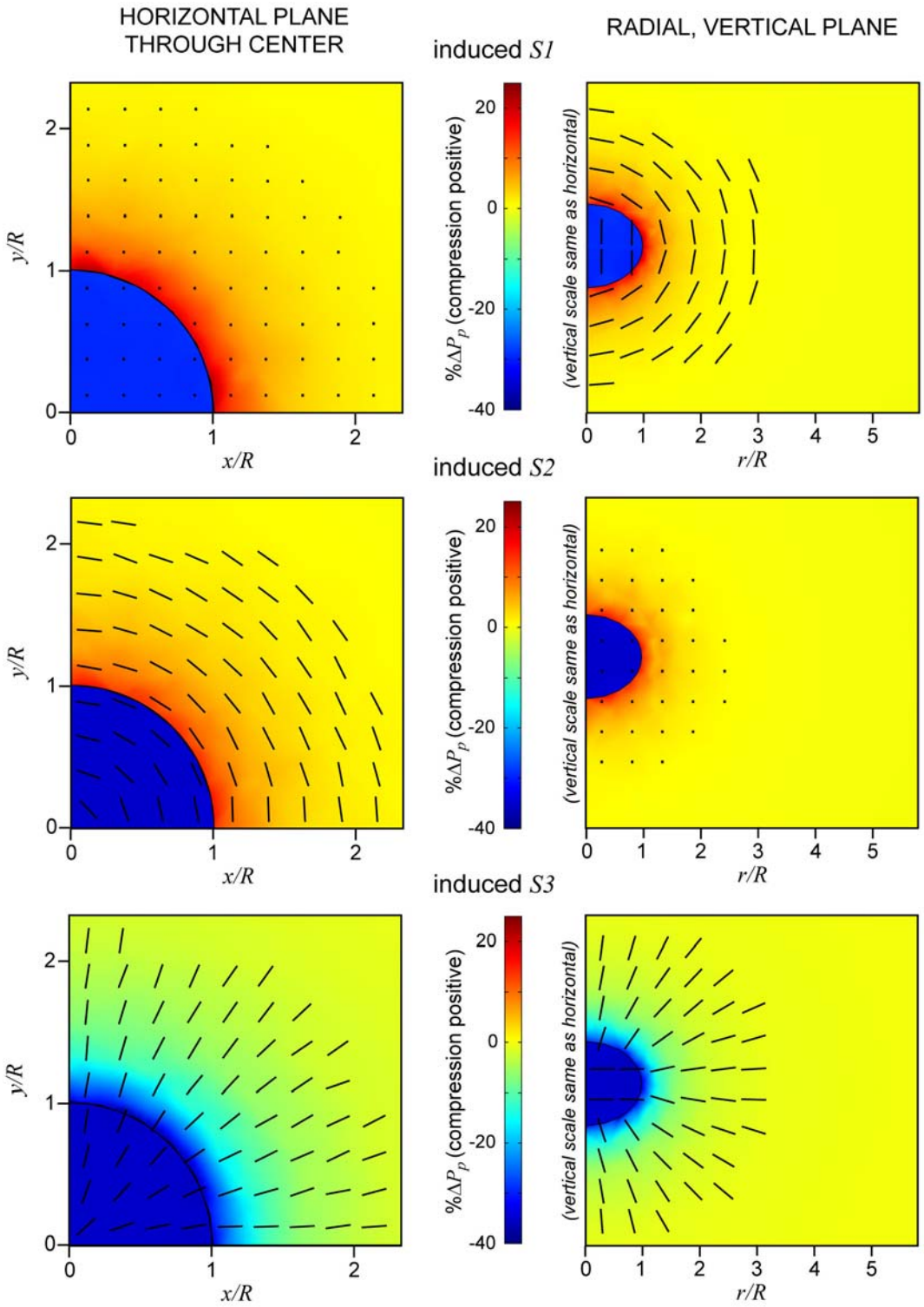

Figure 3–9. Stresses induced by depleting a thick, ellipsoidal reservoir by $-\Delta P_p$. Stress directions are shown with large tick-marks (dots indicate stress oriented into the plane shown). S_1 is the most compressive, and S_3 the least compressive, principal stress.

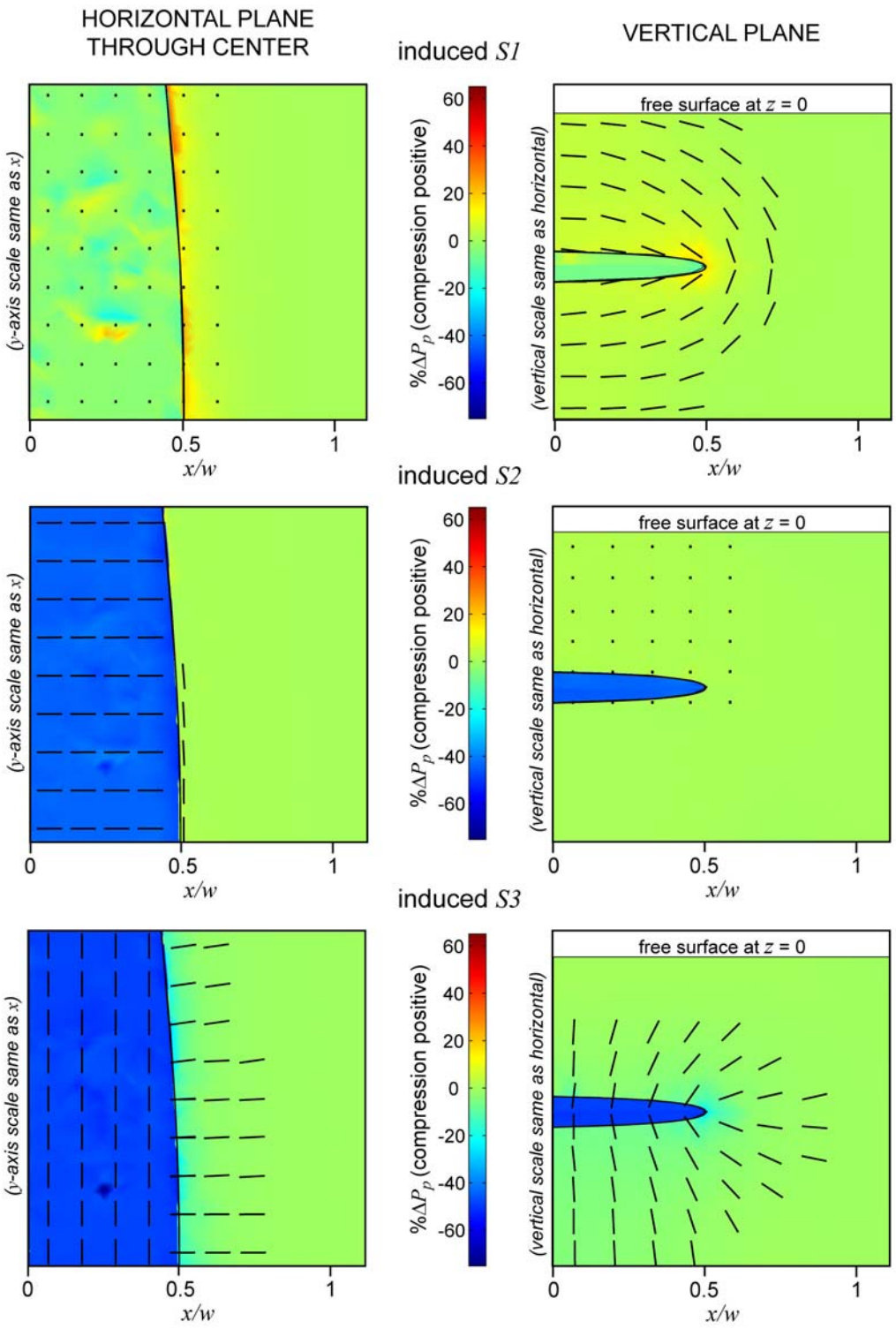

Figure 3–10. Stresses induced by depleting a thin, elongate ellipsoidal reservoir with horizontal width w by $-\Delta P_p$. Stress directions are shown with large tick-marks (dots indicate stress oriented into the plane shown). S_1 is the most compressive, and S_3 the least compressive, principal stress.

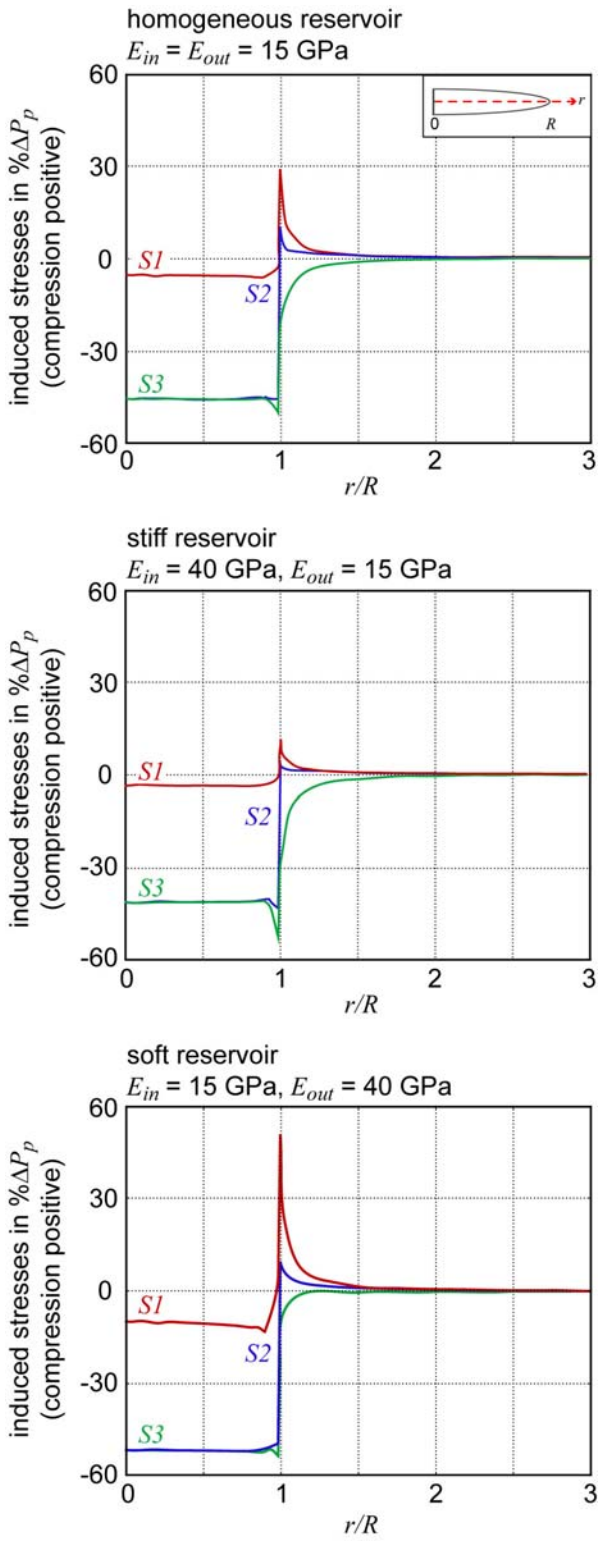

Figure 3–11. Induced principal stress magnitudes as a function of distance from the vertical axis of a disc-shaped reservoir depleted by $-\Delta P_p$. Results are shown from the horizontal plane in the vertical center of the reservoir. The three cases correspond to a reservoir with the same elastic properties as its surroundings (top), a relatively stiff reservoir (middle), and a relatively soft reservoir (bottom).

Effects of Elastic Property Differences

Figure 3–11 illustrates the effects of reservoir elastic properties different from the surrounding material. In the figure, induced stress magnitudes are plotted along a radial line on the horizontal plane through the disc-shaped reservoir geometry. The top plot corresponds to the case shown in Figure 3–8 and discussed above. When the reservoir is effectively stiffer than the surrounding material (in this case has a higher Young's modulus), the induced stress magnitudes decrease. The most notable change is immediately outside the reservoir boundary, where induced vertical compression is greatly reduced. When the reverse case is true, and the material outside higher Young's modulus, then all of the induced stresses increase. Inside the reservoir the change is greatest in the horizontal stresses, but just outside the change is again most notable in the vertical induced compression.

We find the same general results for the thick reservoir model. For the elongate reservoir, however, we find similar but smaller changes in S_1 and S_2, while S_3 (parallel to the boundary inside the inclusion) is relatively unaffected.

3.4.3 Case Studies

Scott Field

In order to illustrate the usefulness of our numerical model, we ran it using stress and pore pressure input parameters from our Scott field case study. For direct comparison to our analytical model results, we used our thin, disc-shaped reservoir and looked at predicted stress orientation changes across the boundary between the depleted and undepleted side on the horizontal plane through the vertical center of the reservoir. An example of our results is shown in Figure 3–12, which presents the expected S_{Hmax} orientation and magnitude changes near an impermeable boundary oriented 75° from the regional S_{Hmax} orientation. Using an original S_{Hmax} magnitude of 96 MPa (close to the overburden magnitude of 98 MPa), the ratio of pore pressure change to differential horizontal stress (equivalent to q in the analytical model) is equal to 2. The maximum rotation from the regional S_{Hmax} direction is in this case only around 20° (Fig. 3–12, top), much lower than the 45–50° rotation predicted by the analytical model (Fig. 3–5). By decreasing the original S_{Hmax} to 81 MPa, which is in the allowable range (see section 3.2.3), we can better match the observed stress rotations near the northeast–southwest striking faults in the Scott field (Fig. 3–1) and original analytical predictions. Doing this however, increases the ratio of pore pressure change to differential

horizontal stress to 4. In the analytical model, q = 4 would result in slightly greater S_{Hmax} rotations (see Fig. 3–4).

The results of this analysis for all values θ are shown in Figure 3–13, in which the numerical model results (circles) are superimposed on the original analytical prediction (black line).

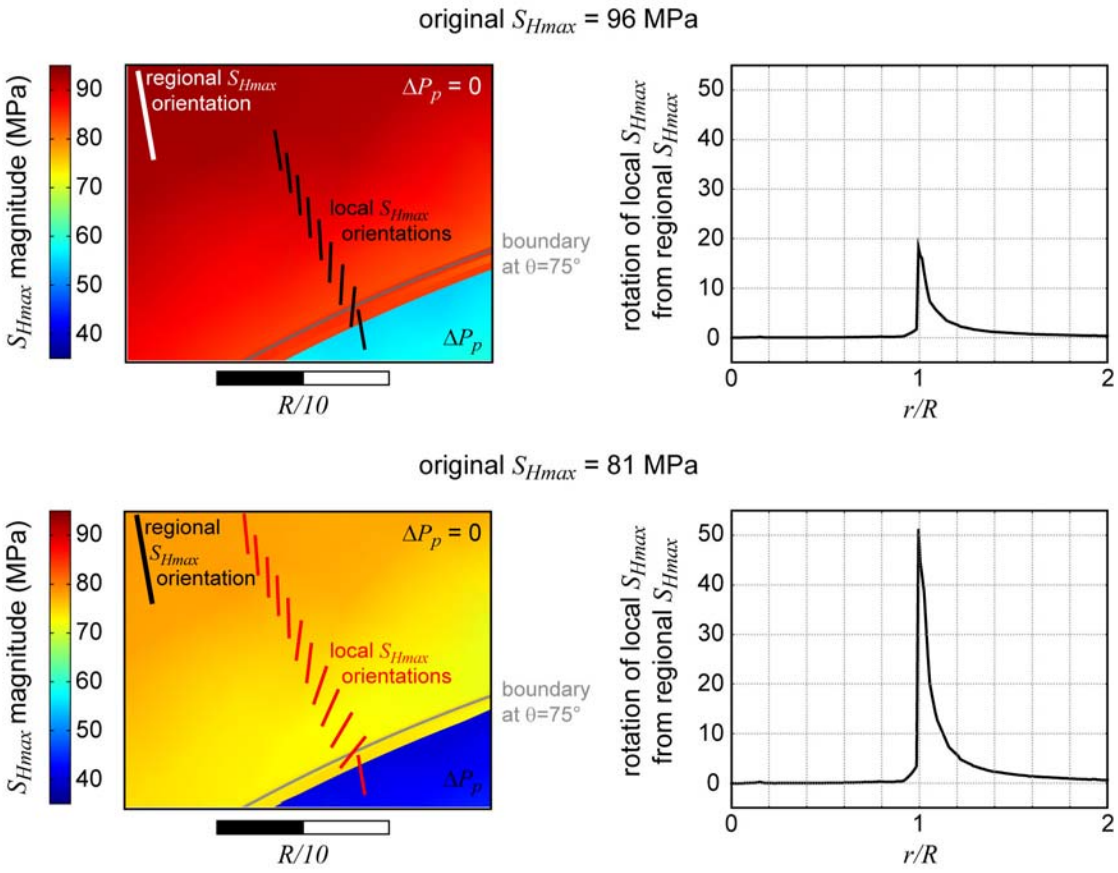

Figure 3–12. Numerical model results for the Scott field using the disc-shaped reservoir model. The left-hand plots show a portion of the horizontal plane through the vertical center of the reservoir, illustrating the rotation of the local S_{Hmax} azimuth across the reservoir boundary (gray line). The right-hand plots show the amount of rotation (γ) as a function of horizontal distance (r) from the reservoir center.

Arcabuz-Culebra

As with the Scott Field case, we used our disc-shaped reservoir to model predicted stress changes in the Arcabuz Field and compared the results directly to the analytical model predictions. Hydraulic fracture tests from a depth of 8000 ft constrain the magnitude of S_{hmin} magnitude to be 0.91 psi/ft, or 50.2 MPa. Using an S_{Hmax} magnitude of 60.6 MPa (equivalent

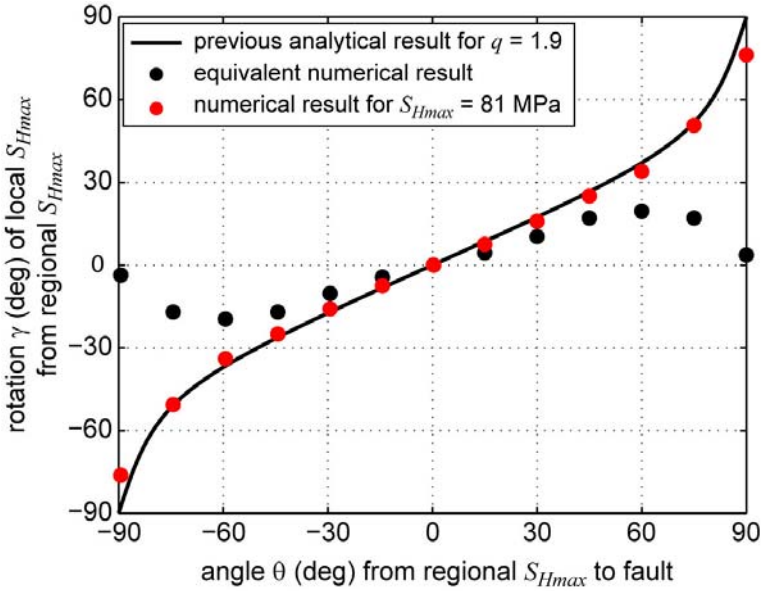

Figure 3–13. Comparison of numerical modeling results (circles) to analytical results (line) for the Scott field.

to 1.1 psi/ft at 8000 ft depth), and ΔP_p = –20 MPa, the ratio of pore pressure change to differential horizontal stress (q in the analytical model) is equal to 2. Our results are shown in Figure 3–14 superimposed on the analytical solution. Once again the numerical model (circles) predicts rotations significantly lower than the analytical model (line). In this case, we can not change numerical model parameters sufficiently to match the analytical predictions.

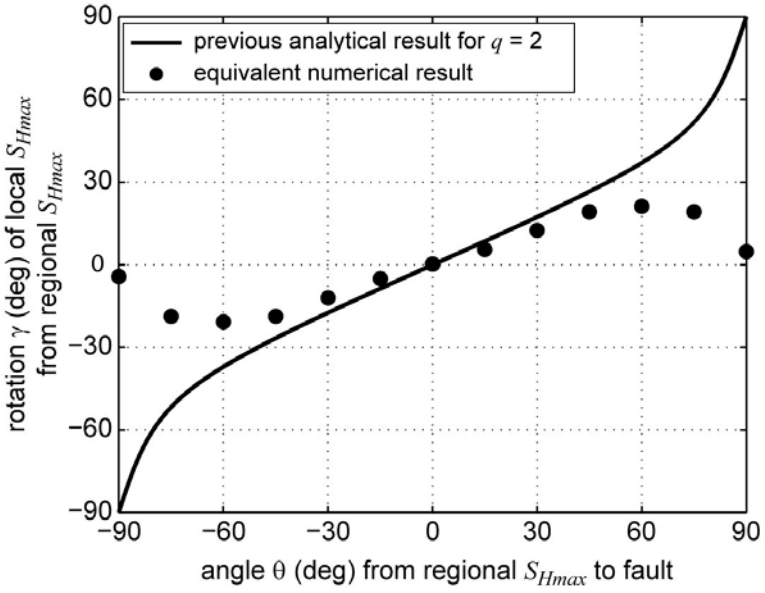

Figure 3–14. Comparison of numerical modeling results (circles) to analytical results (line) for the Arcabuz field.

3.5 Discussion

3.5.1 Model Comparison

The two case studies clearly show that there is not an exact agreement between the analytical and numerical models. In both cases the numerical model predicted smaller stress rotations than the analytical model. This can easily be explained by looking back at the results for our three-dimensional, laterally extensive reservoir in Fig. 3–11. In our analytical model we assumed there was no change to either S_{Hmax} or S_{hmin} outside of the reservoir, but the numerical model shows that induced horizontal stress magnitudes (S_2 and S_3) immediately outside the reservoir boundary are not the same.

The introduction of unequal horizontal induced stresses outside of the reservoir changes the analytical solution presented in Section 3.3. If we introduce a change in stress magnitude in the x direction equal to some value Φ, Eqn. E3–9, our expression for total stress in the x direction outside the reservoir, becomes

$$S_x^{\ b} = S_{\mathrm{Hmax}} + \Phi + \psi_x = S_{\mathrm{Hmax}} + \Phi + \frac{A\Delta P_p}{2}(1-\cos 2\theta)\,. \qquad \text{(E3–16)}$$

This in turn changes Eqn. E3–13, the predicted stress rotation outside the reservoir, to

$$\gamma = \frac{1}{2}\tan^{-1}\left[\frac{-A\Delta P_p \sin 2\theta}{\left(S_{\mathrm{Hmax}} + \Phi - S_{\mathrm{hmin}}\right) - A\Delta P_p \cos 2\theta}\right]. \qquad \text{(E3–17)}$$

Figure 3–15 compares our original ($\Delta S_H^{\ b} = 0$, black lines) and revised ($\Delta S_H^{\ b} = \Phi$, red lines) calculations of stress rotations for several values of q and using $\Phi = -\frac{1}{2}A\Delta P_p$ just outside the boundary in the revised predictions. For all but very small values of q, the inclusion of a stress change outside the reservoir predicts smaller stress rotations. The difference is greatest for intermediate values of q, because at very large or very small values of q the solution is relatively insensitive to the input parameters, predicting either no rotation or total rotation ($\gamma = \theta$) (see Fig. 3–4).

3.5.2 Frictional Stability of Nearby Faults and Fractures

Both our analytical and numerical models assume that if the impermeable boundary is a sealed fault, the changes in stress magnitudes and orientations resulting from the pore pressure

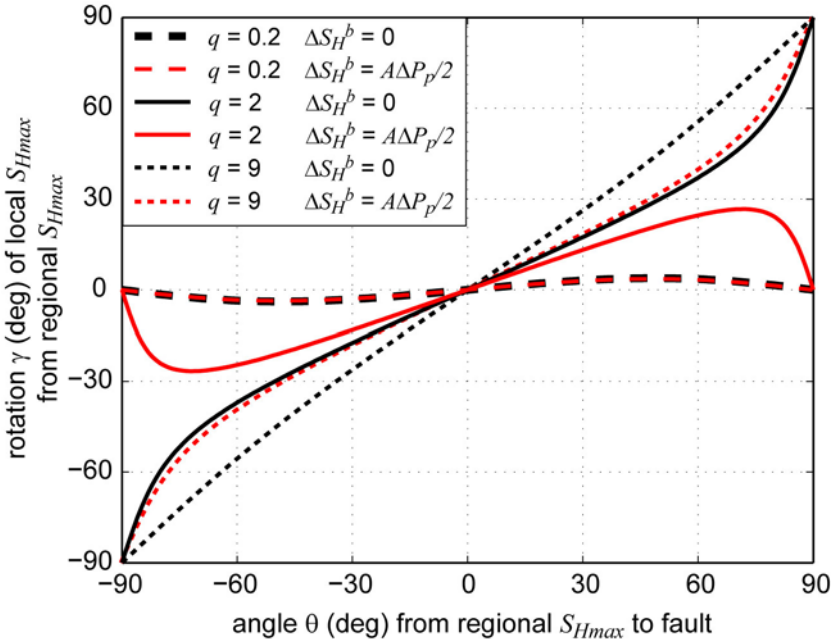

Figure 3–15. Results of our initial and revised analytical solutions. The revised solution (red lines) includes a change in S_{Hmax} outside of the reservoir, $\Phi = -\frac{1}{2}A\Delta P_p$.

change do not induce slip on that fault. However, it has long been known that both injection and depletion can induce small earthquakes (e.g., Zoback and Zinke, 2002). The tendency for pressure-induced stress changes to cause slip on pre-existing faults both outside and inside a reservoir is discussed in detail by Segall (1989, 1992), Segall and Fitzgerald (1998), and Rudnicki (1999). Their results indicate that the risk of inducing faulting varies with both faulting environment and position relative to the reservoir. In a normal faulting environment, for example, the risk of normal faulting due to depletion always increases just outside the edges of the reservoir and increases inside the reservoir if the Biot coefficient is high enough. In a compressional environment, reverse faulting is favored above and below the reservoir, while inside the reservoir all faults are stabilized. Again, however, these studies focus on the effects of changes in stress *magnitudes* only.

To illustrate how pressure-induced stress *orientation* changes may affect the stability of nearby fractures and faults, we calculated the stability of all possible fracture orientations before and after depletion in the Scott field case. Because there are two dominant fault strikes in this field, northeast and east-southeast, we looked at results near each of these assuming they act as impermeable boundaries. The stress rotations induced near each are based on the analytical predictions for q = 1.9 and the numerical predictions for S_{Hmax} = 81 MPa, both of which match stress rotations observed in the field.

As a measure of frictional stability we use the Coulomb Failure Function (CFF), defined as

$$\mathrm{CFF} = \tau - \mu\sigma_n, \qquad \text{(E3–18)}$$

where μ is the coefficient of sliding friction and τ and σ_n are the shear and effective normal stresses, respectively, on the fracture or fault plane. When CFF is negative, the ratio of shear to effective normal stress is less than the frictional strength, μ. Likewise when CFF is positive, the ratio of shear to normal stress exceeds the frictional strength, and we can expect the plane to fail in shear. We call such planes critically stressed. For each stress state, we calculate CFF on all possible fracture or fault orientations, and the results are displayed as colored poles on the lower hemisphere stereoplots in Figure 3–16. Poles to a select subset of planes are shown as larger circles for emphasis, with white poles indicating a positive CFF value and therefore a critically stressed plane.

The upper left-hand plot in Figure 3–16 represents the initial stress and pore pressure conditions prior to production in the Scott field. In this case, faults and fractures with moderate and steep dips towards the northeast, southwest, east, west, southeast, and northwest have a positive CFF and are thus likely to slip. The upper right-hand plot represents the state of stress after a decline in pore pressure but without any resulting stress rotation. Depletion increases stability overall by increasing the effective normal stress on all fractures and faults. While the general east and west dip directions of the most critically stressed fractures do not change, very steeply dipping features are no longer critically stressed. The bottom two plots introduce stress rotations induced by either a northeast (left) or east-southeast (right) striking boundary. In the former case, S_{Hmax} rotates 33° to the east during production. The number of critically stressed faults and fractures is the same as in the case of no stress rotation, but now it is fractures and faults dipping more towards the southeast and northwest that are likely to slip. In contrast, production near an east-southeast striking boundary rotates S_{Hmax} 41° towards the west and the set of critically stressed fracture dips to the northeast and southwest, 90˚ from the critically stressed features in the previous case. Clearly the orientation of the boundary that causes the stress rotation strongly influences which local fractures and faults are likely to be stable or unstable. This can have important implications for issues such as fault leakage and fracture permeability in tight reservoirs.

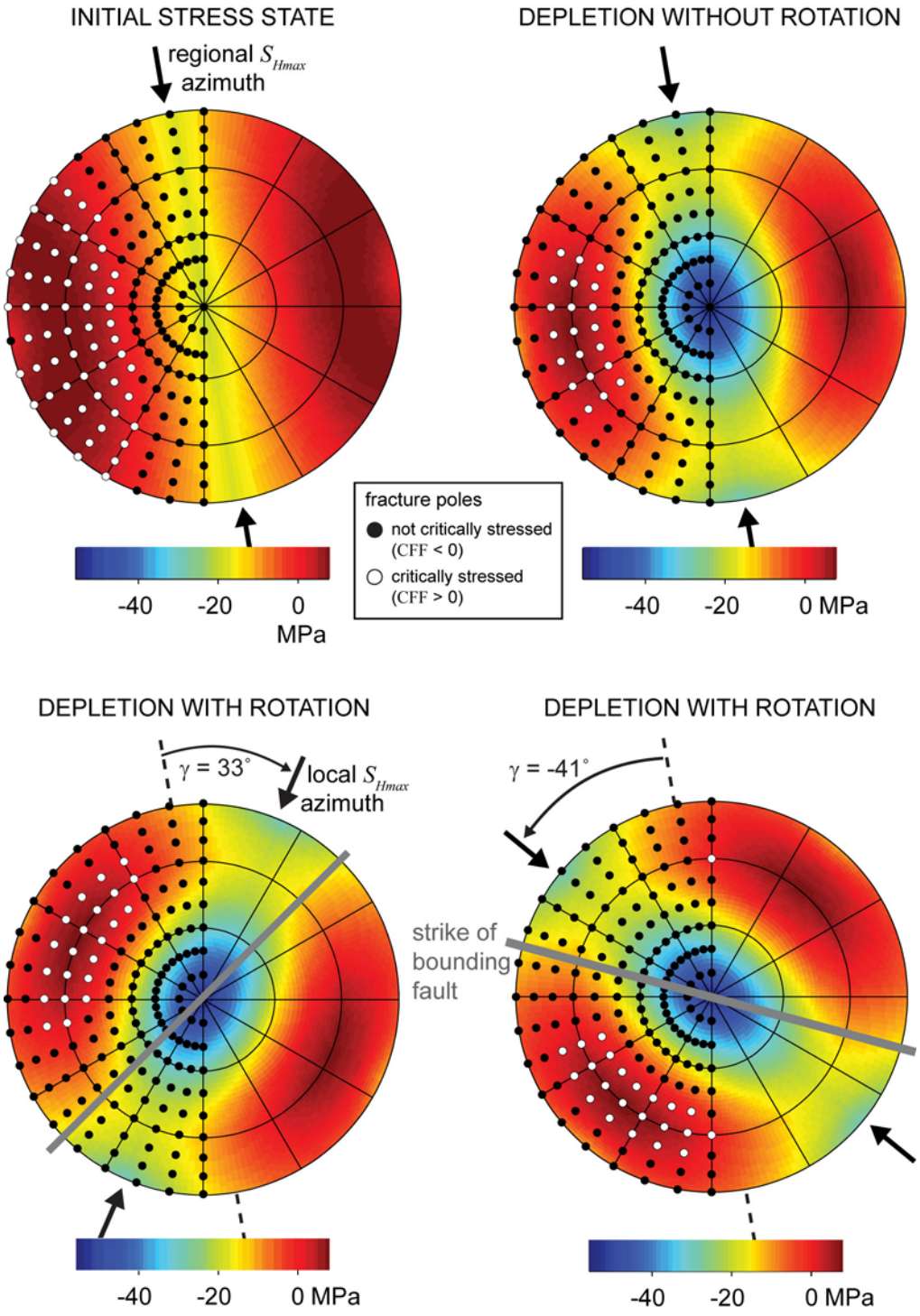

Figure 3–16. Analysis of frictional stability of fractures and faults based on the Scott Field case study. Plots are lower-hemisphere stereoplots showing poles to fault or fracture planes. Background colors give the value of the Coulomb Failure Function (CFF) for all orientations, and poles of a subset of fractures with CFF less than zero (black) and greater than zero (white) are shown for emphasis.

3.5.4 Suggestions for Further Work

Clearly one of the most important extensions of this work would be to find more field cases with which to test our models. For example, in the Lost Hills field in California and the Van field in East Texas, stress directions are available over long time periods from initial and repeat hydraulic fracture treatments (Winterstein and Meadows, 1991; Wright et al., 1994, 1995; Wright and Conant, 1995). In fact, the phenomenon of hydraulic fracture reorientation was first recognized at Lost Hills. The key is, of course, to find data sets with not only stress orientation data, but pre-production stress information and a good estimate of the amount of depletion.

It would be interesting to not just look at the before and after scenarios, but also be able to model the dynamic changes that occur in the reservoir during production. Segall and Fitzgerald (1998) mention, in a general way, the potential effects of abrupt versus slow pore pressure change. Sayers (2006) argues that it should be possible to monitor the change in the ratio of vertical to horizontal effective stresses during depletion using time-lapse seismic measurements.

Finally, our work assumes a uniform pore pressure change throughout the reservoir and a vertical boundary, neither of which may be realistic in many cases. It would be highly beneficial to develop models which allow for non-uniform pore pressure change due to, for example, the effects of individual wells or spatial changes in the hydrologic properties of the reservoir. This might also include looking at combined effects from multiple boundaries. Similarly, the boundary orientations and reservoir shapes should be modified to look at more geologically reasonable scenarios. Numerical modeling would be the ideal tool for such complicated cases.

3.6 Conclusions

Initially we presented a relatively simple analytical method to approximate the rotation of in situ horizontal principal stresses near vertical, impermeable faults in semi-infinite, depleted reservoirs. The presence of a sealing vertical fault in a laterally extensive reservoir causes a uniaxial stress perturbation, which when superimposed onto the background stress field, renders the unperturbed S_{Hmax} azimuth no longer a principal stress direction. As a result, the local S_{Hmax} near the fault is rotated from the regional S_{Hmax}. Depletion causes S_{Hmax} to reorient itself more parallel to the nearby fault, and the amount of rotation depends on 1) the magnitude of the pore pressure change with respect to the original horizontal differential

stress, 2) the orientation of the fault relative to the original S_{Hmax} azimuth, and 3) the elastic properties of the reservoir medium. We showed that reasonable values for these parameters can lead to significant S_{Hmax} rotations, as observed in two documented case studies.

In order to both test the accuracy of our initial model and examine more complicated reservoir geometries and properties, we then developed a three-dimensional numerical model to predict changes in stress magnitudes and directions in and surrounding an elliptical depleted reservoir in a semi-infinite half-space. Our model reveals strong interaction between many parameters that affect the predicted stress rotations. In situ stress magnitudes, rock property contrasts, and reservoir shape are all significant. The following summarizes the main conclusions from our numerical modeling:

- The induced stress magnitudes inside and outside of the reservoir are proportional to the change in pore pressure and the Biot coefficient.
- When the material outside of the reservoir is stiffer, the constrained stresses, and therefore the total induced stresses, increase, and vice-versa.
- In a radially symmetric reservoir, the horizontal induced stresses inside the inclusion are equal, which should not cause any stress rotation. In an elongated reservoir, greater extension is induced parallel to the reservoir long axis than perpendicular to it.
- Relative compression is always induced both in the vertical direction and parallel to the boundary at and outside of the boundary. The effect extends further away from the boundary as reservoir thickness increases.
- In a thin reservoir, the horizontal stresses inside change significantly more than the vertical stress and become less compressive. As reservoir thickness increases, the relative change in the vertical stress increases.
- In much of the region surrounding the reservoir, the induced stress tensor is inclined, although induced stress magnitudes are low.

Importantly, the numerical model predicts a change in maximum horizontal stress magnitude immediately outside of the reservoir boundary that can cause the predicted stress rotation to be significantly different from that determined by our simple, analytical solution. This is especially important for intermediate (roughly 0.5 to 9) ratios of pore pressure change to original horizontal differential stress.

While the primary motivation for this work was to provide a means to predict changes in stress directions that might affect practices like secondary hydraulic fracturing throughout the

life of a reservoir, our results also have important implications for the frictional stability of faults and fractures both in and around the reservoir.

3.7 Acknowledgments

This work was supported primarily by the Stanford Rock and Borehole Geophysics (SRB) consortium with additional scholarships from the Society of Exploration Geophysicists and the Society of Petrophysicists and Well Log Analysts. Thanks to Sang-min Kim for his early work on the analytical model.

3.8 Explanation of Symbols

A	stress–depletion response
a, b	labels for sides of the boundary (a experiences ΔP_p)
E	Young's modulus
P_p	pore pressure
q	parameter for analytical calculation of expected stress rotation
R	horizontal radius of a thin, oblate spheroid
r	radial distance from the vertical axis of a spheroidal reservoir
$S_{1,\ 2,\ or\ 3}$	principal induced stress (1 = most compressive)
S_{Hmax}	maximum in situ horizontal compressive stress
S_{hmin}	minimum in situ horizontal compressive stress
S_H	either principal horizontal stress
$S_{x\ or\ y}$	total stress in x or y direction
S_{xy}	shear stress
w	width of elongated ellipsoid in numerical model
α	Biot effective stress coefficient
γ	stress rotation
θ	angle from the original S_{Hmax} to the boundary
ν	Poisson's ratio
Φ	change in S_{Hmax} outside of the boundary in modified analytical model
σ_n	effective normal stress on a fracture plane
τ	shear stress on a fracture plane
ψ	magnitude of the normal traction on the impermeable boundary
$\psi_{x\ or\ y}$	x or y component of the boundary normal traction
ψ_{xy}	shear component of the boundary normal traction

3.9 References

Addis, M. A. (1997a), Reservoir depletion and its effect on wellbore stability evaluation, *Int. J. Rock Mech. Min. Sci., 34*, 423.

Addis, M. A. (1997b), The stress-depletion response of reservoirs: Proc. Soc. Pet. Eng. Annu. Tech. Conf., 55–65.

Addis, M. A., N. C. Last, and N. A. Yassir (1994) Estimation of horizontal stresses at depth in faulted regions and their relationship to pore pressure variations, in *Eurock '94: Rock Mechanics in Petroleum Engineering*, *Proceedings of the SPE/ISRM International Conference, Delft, Netherlands*, pp. 887–895.

Biot, M. A. (1941), General theory of three-dimensional consolidation, *J. Appl. Phys., 12*, 155–164.

Boulter, R. S., H. Bernal, A. Mendoza, M. Frorup, and Anonymous (1998), Integrated reservoir characterization of the Arcabuz–Culebra Field, Burgos Basin, northern Mexico, *Proc. Amer. Assoc. Pet. Geol. Int. Conf. Exhibit.*, 1894.

Brown, D. (1987) The flow of water and displacement of hydrocarbons in fractured chalk reservoirs, in *Fluid Flow in Sedimentary Basins and Aquifers*, edited by J. C. Goff and B.P. Williams, pp. 201–218, The Geological Society, London.

Engelder, T., and M. P. Fischer (1994), Influence of poroelastic behavior on the magnitude of minimum horizontal stress, Sh, in overpressured parts of sedimentary basins, *Geology, 22*, 949–952.

Eshelby, J. D. (1957), The determination of the elastic field of an ellipsoidal inclusion, and related problems, *Proc. R. Soc. London, A, 241*, 376–396.

Geertsma, J. (1957), The effect of fluid pressure decline on volumetric changes of porous rocks, *Trans. ASME, 210*, 331–340.

Geertsma, J. (1973), Land subsidence above compacting oil and gas reservoirs, *J. Pet. Technol., June*, 734–744.

Hettema, M. H. H., P. M. T. M. Schutjens, B. J. M. Verboom, and H. J. Gussinklo (2000), Production-induced compaction of sandstone reservoirs: The strong influence of stress path, *Soc. Pet. Eng. Res. Eval. Eng., 3*, 342–347.

Jaeger, J. C., and N. G. W. Cook (1979) *Fundamentals of Rock Mechanics*, 593 pp., Chapman and Hall, London.

Lorenz, J. C., L. W. Teufel, and N. R. Warpinski (1991), Regional fractures I: A mechanism for the formation of regional fractures at depth in flat-lying reservoirs, *AAPG Bull., 75*, 1714–1737.

Morita, N., D. L. Whitfill, O. Nygaard, and A. Bale (1989), A quick method to determine subsidence, reservoir compaction, and in-situ stress induced by reservoir depletion, *J. Pet. Technol., 41*, 71–79.

Mouret, C., J.–P. Valois, E. Mastin, and J. Chastang (2005), A new method for efficient fast-track evaluation and assessment of the re-engineering potential of mature fields, *The Leading Edge, 24*, 50–54.

Mura, T. (1982) *Micromechanics of Defects in Solids*, 494 pp., Martinus Nijhoff, The Hague.

Rudnicki, J. W. (1999), Alteration of regional stress by reservoirs and other inhomogeneities: Stabilizing or destabilizing?, *Ninth Int. Congress Rock Mech.*, 1629–1637.

Sayers, C. M. (2006), Sensitivity of time-lapse seismic to reservoir stress path, *Geophys. Prospect., 54*, doi:10.1111/j.1365-2478.2006.00539.x.

Segall, P. (1989), Earthquakes triggered by fluid extraction, *Geology, 17*, 942–946.

Segall, P. (1992), Induced stresses due to fluid extraction from axisymmetric reservoirs, *Pure Appl. Geophys., 139*, 535–560.

Segall, P., and S. D. Fitzgerald (1998), A note on induced stress changes in hydrocarbon and geothermal reservoirs, *Tectonophysics, 289*, 117–128.

Sonder, L. J. (1990), Effects of density contrasts on the orientation of stresses in the lithosphere: Relation to principal stress directions in the Traverse Ranges, California, *Tectonics, 9*, 761–771.

Vazquez, R., A. Mendoza, A. Lopez, M. Linares, and H. Bernal (1997), 3-D seismic role in the integral study of the Arcabuz–Culebra Field, Mexico, *The Leading Edge, 16*, 1763–1766.

Winterstein, D. F., and M. A. Meadows (1991), Shear-wave polarizations and subsurface stress directions at Lost Hills field, *Geophysics, 56*, 1331–1348.

Wolhart, S. L., S. Berumen, C. L. Cipolla, C. A. Barton, and P. T. Branagan (2000) Use of hydraulic fracture diagnostics to optimize fracturing jobs in the Arcabuz–Culebra field, paper presented at SPE Rocky Mountain Regional/Low-Permeability Reservoirs Symposium and Exhibition, SPE Paper 60314.

Wright, C. A., and R. A. Conant (1995), Hydraulic fracture reorientation in primary and secondary recovery from low-permeability reservoirs, paper presented at Society of Petroleum Engineers Annual Technical Conference and Exhibition, SPE Paper 30484.

Wright, C. A., D. W. Stewart, M. A. Emanuele, and W. W. Wright (1994), Reorientation of propped refracture treatments in the Lost Hills Field, paper presented at SPE Western Regional Meeting, Long Beach, CA, 23–25 March, SPE Paper 27896.

Yale, D. P., J. M. Rodriguez, T. B. Mercer, and D. W. Blaisdell (1994), In-situ stress orientation and the effects of local structure—Scott Field, North Sea, in *Eurock '94: Rock Mechanics in Petroleum Engineering*, *Proceedings of the SPE/ISRM International Conference, Delft, Netherlands*, 945–952.

Zoback, M. D., and J. C. Zinke (2002), Production-induced normal faulting in the Valhall and Ekofisk oil fields, *Pure Appl. Geophys., 159*, pp. 403–420.

3.10 Appendix

This appendix contains the information necessary for any experienced COMSOL Multiphysics™ user to recreate the models used in this study. Any properties not present in the appendix maintain their default values in the model.

Model Properties

Property	Value
Model name	Stress Rotation from Depletion
Author	Amy Day-Lewis
Company	Stanford University
Department	Geophysics
Reference	
URL	
Saved date	Nov 28, 2007 12:30:10 PM
Creation date	Jun 29, 2007 10:33:50 AM
COMSOL version	COMSOL 3.3.0.511

File name: disc in halfspace.mph

Application modes and modules used in this model: Solid, Stress-Strain

Model description

This model uses the basic concepts behind Eshelby inclusion theory (Eshelby, Proceedings of the Royal Society of London, Series A, 1957) to calculate stress magnitudes and directions induced by changing the pore pressure in ellipsoidal reservoirs. It can be easily customized by changing the model Constants.

How to use:

1) Set the values for the Constants: deltap, in situ stresses, biot coefficient, and elastic properties inside and outside the boundary.
2) Select the desired geometry.
3) Run the model.
4) Use the Postprocessing menu to look at the results in various ways. Many useful parameters for display are defined in the Global Expressions.

Notes:
* To view the original in situ stresses only, set deltap to zero.
* To see only the induced stresses/strains (Eshelby "transform" + "constrained"), set the in situ stresses to zero.
* To see the "constrained" stresses/strains only, set the in situ stresses AND s_tform to zero.

Warnings:
1) Changing the scale of the geometry in Draw mode may render the model unable to draw a mesh.
2) Refining the mesh more than once often makes the solver run out of memory (machine-specific).
3) If a new geometry is made, all of the subdomain and boundary settings, boundary expressions, and changes to the equation system must be redefined for that geometry. Use the information below.

Global Expressions

Name	Expression	Description
phi	pi*angleSH/180+0.5*pi	angle used to calculate original stress components (magnitudes)
origSx	0.5*(SHmax+Shmin)-0.5*(SHmax-Shmin)*cos(2*phi)	original horizontal stress magnitude in x direction
origSy	0.5*(SHmax+Shmin)+0.5*(SHmax-Shmin)*cos(2*phi)	original horizontal stress magnitude in y direction
origSxy	0.5*(SHmax-Shmin)*sin(2*phi)	original horizontal shear stress
phi2	-pi*angleSH/180	used to calculate original SHmax arrow components
origSHx	cos(phi2)	x component for original SHmax arrow
origSHy	sin(phi2)	y component for original SHmax arrow
s1x	if(abs(s1_sld)<1,0,s1x_sld)	removes arrows where induced stress magnitudes are very small
s1y	if(abs(s1_sld)<1,0,s1y_sld)	removes arrows where induced stress magnitudes are very small

s1z	if(abs(s1_sld)<1,0,s1z_sld)	removes arrows where induced stress magnitudes are very small
s2x	if(abs(s2_sld)<1,0,s2x_sld)	removes arrows where induced stress magnitudes are very small
s2y	if(abs(s2_sld)<1,0,s2y_sld)	removes arrows where induced stress magnitudes are very small
s2z	if(abs(s2_sld)<1,0,s2z_sld)	removes arrows where induced stress magnitudes are very small
s3x	if(abs(s3_sld)<1,0,s3x_sld)	removes arrows where induced stress magnitudes are very small
s3y	if(abs(s3_sld)<1,0,s3y_sld)	removes arrows where induced stress magnitudes are very small
s3z	if(abs(s3_sld)<1,0,s3z_sld)	removes arrows where induced stress magnitudes are very small
s1inc	90*(1-abs(s1z_sld))	inclination of first principal stress
s2inc	90*(1-abs(s2z_sld))	inclination of second principal stress
s3inc	90*(1-abs(s3z_sld))	inclination of third principal stress
s1v_flag	if(abs(s1z_sld)>abs(s2z_sld)&abs(s1z_sld)>abs(s3z_sld),1,0)	(used in Sv_flag)
s2v_flag	if(abs(s2z_sld)>abs(s1z_sld)&abs(s2z_sld)>abs(s3z_sld),2,0)	(used in Sv_flag)
s3v_flag	if(s1v_flag==0&s2v_flag==0,3,0)	(used in Sv_flag)
Sv_flag	s1v_flag+s2v_flag+s3v_flag	indicator of which principal stress is most vertical (= 1, 2, or 3)
Svmag	if(Sv_flag==1,s1_sld,if(Sv_flag==2,s2_sld,s3_sld))	magnitude of most vertical principal stress
Svx	if(Sv_flag==1,s1x,if(Sv_flag==2,s2x,s3x))	x-component of most vertical principal stress
Svy	if(Sv_flag==1,s1y,if(Sv_flag==2,s2y,s3y))	y-component of most vertical principal stress
Svz	if(Sv_flag==1,s1z,if(Sv_flag==2,s2z,s3z))	z-component of most vertical principal stress
Svinc_temp	if(abs(s1z_sld)>abs(s2z_sld),s1z_sld,s2z_sld)	(used in Svinc)
Svinc	if(abs(s3z_sld)>abs(Svinc_temp),s3inc,90*(1-abs(Svinc_temp)))	inclination of most vertical principal stress
SHmag	if(Sv_flag==3,s2_sld,s3_sld)	magnitude of the most compressive horizontal stress
SHx	if(Sv_flag==3,s2x,s3x)	x-component of most compressive horizontal stress
SHy	if(Sv_flag==3,s2y,s3y)	y-component of most compressive horizontal stress
SHz	if(Sv_flag==3,s2z,s3z)	z-component of most compressive horizontal stress

SHrot	-atan(SHy/SHx)*180/pi	rotation of SHmax from the x-axis
Shmag	if(Sv_flag==1,s2_sld,s1_sld)	magnitude of the least compressive horizontal stress
Shx	if(Sv_flag==1,s2x,s1x)	x-component of the least compressive horizontal stress
Shy	if(Sv_flag==1,s2y,s1y)	y-component of the least compressive horizontal stress
Shz	if(Sv_flag==1,s2z,s1z)	z-component of the least compressive horizontal stress

Boundary Expressions

Boundary	6	10
pressure_x	-deltap*nx*biot	-deltap*nx*biot
pressure_y	-deltap*ny*biot	-deltap*ny*biot
pressure_z	-deltap*nz*biot	-deltap*nz*biot

Application Mode: Solid, Stress-Strain (sld)
Application mode type: Solid, Stress-Strain
Application mode name: sld

Property	Value
Default element type	Lagrange - Quadratic
Analysis type	Static
Specify eigenvalues using	Eigenfrequency
Frame	Frame (ref)
Weak constraints	Off

Boundary Settings

Boundary		11	1, 4, 7, 13
Face load (force/area) x-dir. (Fx)		0	0
Face load (force/area) y-dir. (Fy)		0	0
Face load (force/area) z-dir. (Fz)		0	0
Hx		0	1
Hy		0	0
Hz		0	0

Boundary	2, 5, 8, 12	3, 9	10
Face load (force/area) x-dir. (Fx)	0	0	pressure_x
Face load (force/area) y-dir. (Fy)	0	0	pressure_y
Face load (force/area) z-dir. (Fz)	0	0	pressure_z
Hx	0	0	0
Hy	1	0	0

Hz	0	1	0

Boundary	6
Face load (force/area) x-dir. (Fx)	-pressure_x
Face load (force/area) y-dir. (Fy)	-pressure_y
Face load (force/area) z-dir. (Fz)	-pressure_z
Hx	0
Hy	0
Hz	0

Subdomain Settings

Locked Subdomains: 1-3

Subdomain	1	2-3
Shape functions (shape)	shlag(2,'u') shlag(2,'v') shlag(2,'w')	shlag(2,'u') shlag(2,'v') shlag(2,'w')
Integration order (gporder)	4 4 4	4 4 4
Constraint order (cporder)	2 2 2	2 2 2
Young's modulus (E)	E_out	E_in
Density (rho)	rho_out	rho_in
Poisson's ratio (nu)	nu_out	nu_in

Constants

Name	Expression	Value	Description
deltap	-100		pressure difference [Pa, neg for depletion]
biot	.75		Biot coefficient
s_tform	-biot*deltap		Eshelby transformation stress
SHmax	0		[Pa, compression negative]
Shmin	0		[Pa, compression negative]
Sv	0		[Pa, compression negative]
angleSH	0		angle from x to SHmax [-90 to 90, CW+]
E_in	15e9		Young's modulus inside [Pa]
E_out	15e9		Young's modulus outside [Pa]
nu_in	.25		Poisson's ratio inside
nu_out	.25		Poisson's ratio outside
rho_in	2750		density inside [kg/m^3]
rho_out	2750		density outside [kg/m^3]

Solver Settings

Solve using a script: off

Analysis type	Static

Auto select solver	On
Solver	Stationary
Solution form	Automatic
Symmetric	auto
Adaption	Off

Direct (SPOOLES)
Solver type: Linear system solver

Parameter	Value
Pivot threshold	0.1
Preordering algorithm	Minimum degree

Equations

Variables Subdomain 1 (matrix)

Name	Description	Expression
sx_sld	sx normal stress global sys.	origSx+E_sld * (1-nu_sld) * ex_sld/((1+nu_sld) * (1-2 * nu_sld))+E_sld * nu_sld * ey_sld/((1+nu_sld) * (1-2 * nu_sld))+E_sld * nu_sld * ez_sld/((1+nu_sld) * (1-2 * nu_sld))
sy_sld	sy normal stress global sys.	origSy+E_sld * nu_sld * ex_sld/((1+nu_sld) * (1-2 * nu_sld))+E_sld * (1-nu_sld) * ey_sld/((1+nu_sld) * (1-2 * nu_sld))+E_sld * nu_sld * ez_sld/((1+nu_sld) * (1-2 * nu_sld))
sz_sld	sz normal stress global sys.	Sv+E_sld * nu_sld * ex_sld/((1+nu_sld) * (1-2 * nu_sld))+E_sld * nu_sld * ey_sld/((1+nu_sld) * (1-2 * nu_sld))+E_sld * (1-nu_sld) * ez_sld/((1+nu_sld) * (1-2 * nu_sld))
sxy_sld	sxy shear stress global sys.	origSxy+E_sld * exy_sld/(1+nu_sld)

Subdomain 2-3 (inclusion)

Name	Description	Expression
sx_sld	sx normal stress global sys.	origSx+s_tform+E_sld * (1-nu_sld) * ex_sld/((1+nu_sld) * (1-2 * nu_sld))+E_sld * nu_sld * ey_sld/((1+nu_sld) * (1-2 * nu_sld))+E_sld * nu_sld * ez_sld/((1+nu_sld) * (1-2 * nu_sld))
sy_sld	sy normal stress global sys.	origSy+s_tform+E_sld * nu_sld * ex_sld/((1+nu_sld) * (1-2 * nu_sld))+E_sld * (1-nu_sld) * ey_sld/((1+nu_sld) * (1-2 * nu_sld))+E_sld * nu_sld * ez_sld/((1+nu_sld) * (1-2 * nu_sld))
sz_sld	sz normal stress global sys.	Sv+s_tform+E_sld * nu_sld * ex_sld/((1+nu_sld) * (1-2 * nu_sld))+E_sld * nu_sld * ey_sld/((1+nu_sld) * (1-2 * nu_sld))+E_sld * (1-nu_sld) * ez_sld/((1+nu_sld) * (1-2 * nu_sld))
sxy_sld	sxy shear stress global sys.	origSxy+E_sld * exy_sld/(1+nu_sld)

CHAPTER 4. LONG-TERM POROELASTIC STRAIN IN SHALLOW BOREHOLES

4.1 Abstract

Borehole strainmeter data routinely show a relatively large magnitude trend over the first months to years after installation. These trends mask much smaller-magnitude signals of interest such as coseismic offsets and therefore must be removed from the strain record. The traditional approach for trend removal involves either regression or low-pass filtering, neither of which is based on a physical model for the source of the signal. Utilizing data from twenty-one four-component, borehole tensor strainmeters deployed as part of the NSF EarthScope Plate Boundary Observatory between 2005 and 2007, we show that these long-term trends result at least in part from poroelastic deformation driven by the wellbore stress concentration, which allows us to derive a model-based approach for removing them. In addition, from the long-term strain accumulation we can gain insight into the physical properties of the rock surrounding the strainmeter as well as the local in situ stress state; the latter can be compared to independent stress indicators such as earthquake focal mechanisms and stress-induced wellbore failure. In a general sense, this work provides information about time-dependent borehole deformation that will have implications not only for the strainmeter community but also in wellbore engineering and other scientific applications.

4.2 Introduction

Strainmeters have been in use for several decades for the measurement of strain in the earth's crust. Yet the dominant signal recorded by these instruments during the first months, a relatively large magnitude, long-term accumulation of compressional or extensional strain that is removed prior to interpretation of the residual signal, has never been fully understood. In this work we model these long-term trends in terms of the poroelastic response of the wellbore to drilling. First, we examine the azimuthal distribution of measured radial strain from four-component borehole tensor strainmeters and show that the distribution matches that predicted by a poroelastic model. We then use the poroelastic model to provide a single expression that describes the trends measured by all four gauges. Using data from several strainmeters in different locations, we illustrate how our expression for the trend successfully describes strain accumulation for several months to over a year after installation. Finally, we show how

analysis of the strainmeter data using the poroelasticity approach reveals in situ crustal stress orientations that are consistent with independent stress measurements in the same region.

4.2.1 Borehole Strainmeters

Agnew (1986) provides an excellent introduction to the measurement of wellbore strain and the development of volumetric strainmeter instruments. The subsequent development of borehole tensor strainmeters allowed for the measurement of radial strain in specific directions, which enables calculation of both areal and shear strain (Gladwin, 1984). Installation of these instruments involves lowering them into a borehole that was cored or rotary drilled slightly larger than the strainmeter diameter, with centralizers on the tool string to keep the instrument centered. The strainmeter is then coupled to the rock by injection of a layer of expansive grout between the instrument and borehole wall (see Fig. 4–2). Some installations also include a pressure transducer, temperature sensor, and/or borehole seismometer located above the grouted strainmeter.

Raw borehole strainmeter data are a combination of numerous signals including but not limited to atmospheric pressure, earth tides, ocean loading, grout curing and thermal equilibration, background noise, and, finally, responses to tectonic events (Agnew, 1986). Atmospheric and tidal signals are on the order of hundredths of a microstrain and can be accurately removed from the strainmeter data using measured or modeled values. They are also used to calibrate strainmeter data and evaluate data quality. The effects of grout curing and temperature perturbations, while not exactly known, are relatively short-term and only occur soon after installation of the instrument, and therefore they are often ignored or removed using a best-fit mathematical function. Noise can be characterized using spectral methods and removed through filtering.

Most tectonic strain signals are relatively small in magnitude. Coseismic offsets, for example, are generally on the order of one microstrain or less (e.g., Johnston et al., 1994), and aseismic creep events are on the order of 50 to 100 nanostrain (e.g., Gladwin et al., 1994). Long-term tectonic strain accumulation occurs in tectonically active areas like Parkfield, California near the San Andreas fault (Gwyther et al., 1996), and Piñon Flat, California, near the San Jacinto fault (Gladwin et al., 1987) and has magnitudes generally less than 1 microstrain per year. Non-tectonic events such as groundwater-induced strain from rainfall events, seasonal recharge, or pumping in nearby water wells may also be observed (e.g.,

Gwyther et al., 1996; Wyatt and Agnew, 1998) and have magnitudes generally less than 1 microstrain.

Masking all of these relatively small signals is a much larger long-term trend that amounts to tens of microstrain and persists for months to years after installation. Qualitatively the trends are attributed to "borehole relaxation" or "post-relief recovery" assuming viscoelastic behavior of the surrounding rock (Gladwin et al., 1987), but no quantitative, physical model for them has been offered. Uncertainty in their origin and meaning have led to the conclusion that long-term tectonic strain rates can not be measured, because they are masked by the trends (Roeloffs, 2006). That is not to say that there is nothing physically meaningful in the long-term trends, just that without a physical model it is impossible to extract anything meaningful from them.

The most common approach for removing the trends involves determining a best-fit curve, a combination of linear and exponential terms, to strain measured as a function of time (Gwyther et al., 1996). Historically, this approach has worked well, particularly for volumetric strainmeters. In tensor strainmeters, it is applied to each gauge separately. Figure 4–1 shows an example of this approach using data from a PBO four-component borehole tensor strainmeter. In this case the form chosen for the trend is

$$\text{mathematical trend} = F + A_1 e^{T_1 t} + Mt + A_2 e^{T_2 t} \qquad \text{(E4–1)}$$

where t is time (in days) and the constants F, A_1, T_1, M, A_2, and T_2 are unique for each gauge. The long-term trend recorded on one gauge, therefore, is completely independent of those on all of the other gauges.

It is also important to note that a strainmeter is essentially an inclusion, and one that is usually softer elastically than the surrounding rock. As a result, strain measured by a borehole strainmeter is a magnified version of the rock strain. Gladwin and Hart (1985) attempted to quantify this effect by deriving elastic solutions for the strainmeter response to a uniaxial far-field stress. They examined three cases: an empty hole (or one in which the strainmeter and grout are elastically the same as the rock), a "one-ring model" where the instrument has distinct elastic properties but the layer of grout between the instrument and the rock is very thin or has elastic properties similar to the rock, and a "two-ring model" where the grout has distinct elastic properties from both the instrument and the rock. For each model, far-field strain is related to instrument strain by derivation of instrument response factors (essentially scaling constants) for both the shear and areal strain components. The response factor

magnitudes range roughly from one to four, meaning measured strain is one to four times the strain in the surrounding rock (Gladwin et al., 1987). Since they are based on elasticity, these models do not incorporate any time-dependent effects. Spathis (1988) examined the case where the instrument response factors may in fact have some dependence on time.

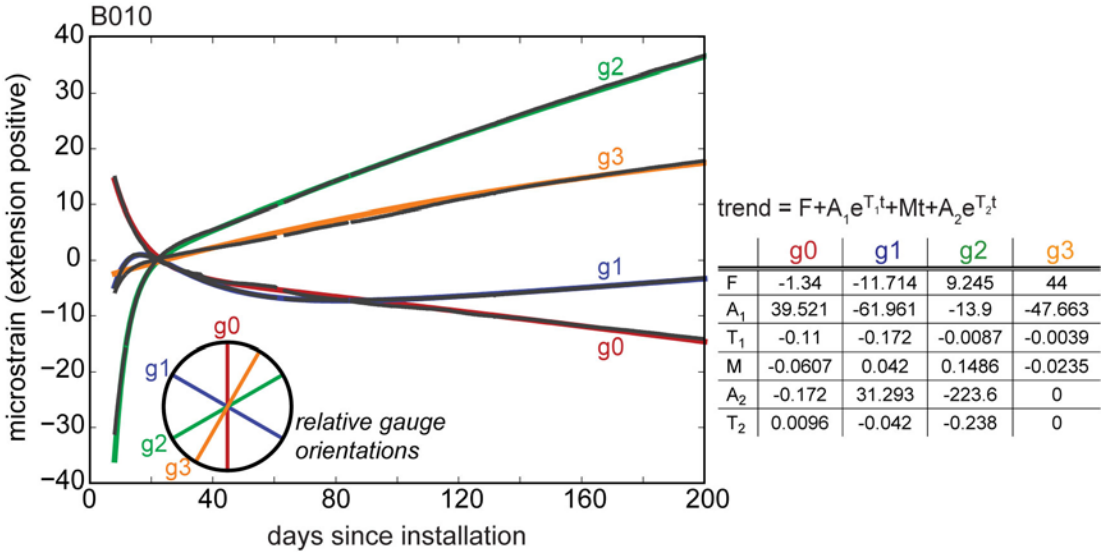

	g0	g1	g2	g3
F	-1.34	-11.714	9.245	44
A_1	39.521	-61.961	-13.9	-47.663
T_1	-0.11	-0.172	-0.0087	-0.0039
M	-0.0607	0.042	0.1486	-0.0235
A_2	-0.172	31.293	-223.6	0
T_2	0.0096	-0.042	-0.238	0

Figure 4–1. Radial strain (grey lines) measured by a four-component borehole tensor strainmeter and the best-fit mathematical trends (colored lines) for each gauge. The table gives the general form of all of the trend lines and the exact trend parameters for each gauge. (Data and trend parameters are from PBO. Day for zero strain is arbitrary, and only relative strain changes over time are meaningful).

The ring model approach is the recommended basis for analytical strainmeter data calibration, but it is generally not used in practice because of the difficulty in constraining the elastic parameters (which can number up to nine). Instead, an empirical approach using modeled solid earth tides and ocean loading is employed (Hart et al., 1996). The calibration process involves empirically determining values for the areal and shear response factors such that earth tides measured by the instrument match theoretical, model-derived tides. The data that remain after removal of the trends are calibrated against modeled tides and then used to calculate the local areal and shear strain components (Hart et al., 1996).

In addition to overall instrument calibration, it is sometimes necessary to weight data from particular gauges in order to bring atmospheric pressure, tidal signals, or earthquake signals measured on different gauges into agreement. Unfortunately, this remains an imprecise science, and not uncommonly gauge weights determined using one approach differ from those derived from an alternate approach. The need for individual gauge weights has been attributed

to instrument errors, measurement errors, and inhomogeneities in the near wellbore environment (Hart et al., 1996; Yoshikawa et al., 2001).

4.2.2 Wellbore Stress and Strain

The Elastic Wellbore Stress Concentration

Kirsch (1898) first described the local, elastic stress concentration caused by drilling a well with a given radius (R) into rock subject to in situ principal stresses S_v (vertical), S_{Hmax} (maximum horizontal compression), and S_{hmin} (minimum horizontal compression). If the wellbore axis is vertical and fluid pressure in the wellbore is the same as in the surrounding rock, then the resulting stresses near the borehole in polar coordinates are

radial stress

$$\sigma_{rr} = \frac{1}{2}\left(S_{\mathrm{Hmax}} + S_{\mathrm{hmin}}\right)\left(1 - \frac{r^2}{R^2}\right) + \frac{1}{2}\left(S_{\mathrm{Hmax}} - S_{\mathrm{hmin}}\right)\left(1 - 4\frac{r^2}{R^2} + 3\frac{r^4}{R^4}\right)\cos 2\theta \qquad \text{(E4–2)}$$

tangential stress

$$\sigma_{\theta\theta} = \frac{1}{2}\left(S_{\mathrm{Hmax}} + S_{\mathrm{hmin}}\right)\left(1 + \frac{r^2}{R^2}\right) - \frac{1}{2}\left(S_{\mathrm{Hmax}} - S_{\mathrm{hmin}}\right)\left(1 + 3\frac{r^4}{R^4}\right)\cos 2\theta \qquad \text{(E4–3)}$$

and vertical stress

$$\sigma_{zz} = S_{\mathrm{v}} - 2\nu\left(S_{\mathrm{Hmax}} - S_{\mathrm{hmin}}\right)\frac{r^2}{R^2}\cos 2\theta, \qquad \text{(E4–4)}$$

where θ is the angle from the direction of S_{Hmax} and r is radial distance from the wellbore axis (Cristescu and Hunsche, 1998, Eqn. 8.3.2). One can easily see that if the two horizontal stress magnitudes are equal, then the dependence on azimuth disappears. Radial strain (ε_{rr}) that occurs in response to the stress concentration in an isotropic, linear elastic medium is given by

$$\varepsilon_{rr} = \frac{1}{2G}\left[\sigma_{rr} - \frac{\nu}{1+\nu}\left(\sigma_{rr} + \sigma_{\theta\theta} + \sigma_{zz}\right)\right] \qquad \text{(E4–5)}$$

where G is the shear modulus of the rock, and ν is the drained Poisson's Ratio (Wang, 2000, Eqn. 2.39). Radial strain, therefore, also varies with $\cos 2\theta$ under conditions of unequal horizontal stresses; the greatest amount of compression occurs parallel to S_{Hmax}, while the greatest amount of extension occurs perpendicular to it. (Note that in this study we will follow

the strainmeter community's convention of positive extensional strains. We therefore also assign positive values to tensional stresses and negative values to compressional stresses).

The elastic stress concentration and resulting strain are instantaneous. In practice, however, there is some delay between drilling a strainmeter borehole and installing the instrument itself. This delay can range from hours to months. Borehole strainmeters, therefore, can only measure strain changes after the instrument is in place, not the instantaneous elastic strain caused by drilling of the hole. If the long-term strain trends are due to the borehole stress concentration, then there must be some mechanism that delays the accumulation of total strain in the rock near the wellbore.

Poroelasticity

In a poroelastic material, solid deformation is coupled to fluid pressure. As a result, the equation for strain contains an additional, pressure-dependent term,

$$\varepsilon_{rr} = \frac{1}{2G}\left[\sigma_{rr} - \frac{\nu}{1+\nu}\left(\sigma_{rr} + \sigma_{\theta\theta} + \sigma_{zz}\right)\right] + \frac{1-2\nu}{2G(1+\nu)}\alpha p\,, \qquad \text{(E4–6)}$$

where α is the Biot coefficient and p is pressure (Biot, 1941; Rice and Cleary, 1976). Pressure, in turn, depends on the volumetric strain rate,

$$\frac{\partial p}{\partial t} = k\frac{K_u B}{\alpha}\nabla^2 p + K_u B\frac{\partial \varepsilon_{kk}}{\partial t}\,, \qquad \text{(E4–7)}$$

where t is time, k is permeability, and K_u is the undrained bulk modulus. In a fully drained material, fluid can escape from the pore space instantaneously upon application of a load, and deformation is governed by the purely elastic moduli. When fluids are completely trapped in the pore space, the material is *undrained*, and deformation is governed by undrained moduli. Most real situations fall somewhere between these two extremes. Skempton's coefficient, B, quantifies the change in pressure resulting from a change in applied stress and is related to the poroelastic properties of the rock through

$$B = \frac{3(\nu_u - \nu)}{\alpha(1+\nu_u)(1-2\nu)}\,, \qquad \text{(E4–8)}$$

where ν_u is the undrained Poisson's ratio (Wang, 2000).

Drilling sets up an unequal pressure distribution around a wellbore due to azimuthal and radial variations in volumetric strain. Initially, this distribution is

$$p^{(t=0^+)} = \frac{4}{3} B(S_{\text{Hmax}} - S_{\text{hmin}})(1+\nu_u)\frac{R^2}{r^2}\cos 2\theta \qquad \text{(E4–9)}$$

(Detournay and Cheng, 1988), which clearly depends not only on radius, but also on azimuth. Therefore fluid flow during equilibration is both radial and tangential to the wellbore. This is shown conceptually in Figure 4–2. The time it takes for pressure to re-equilibrate depends strongly on the formation permeability.

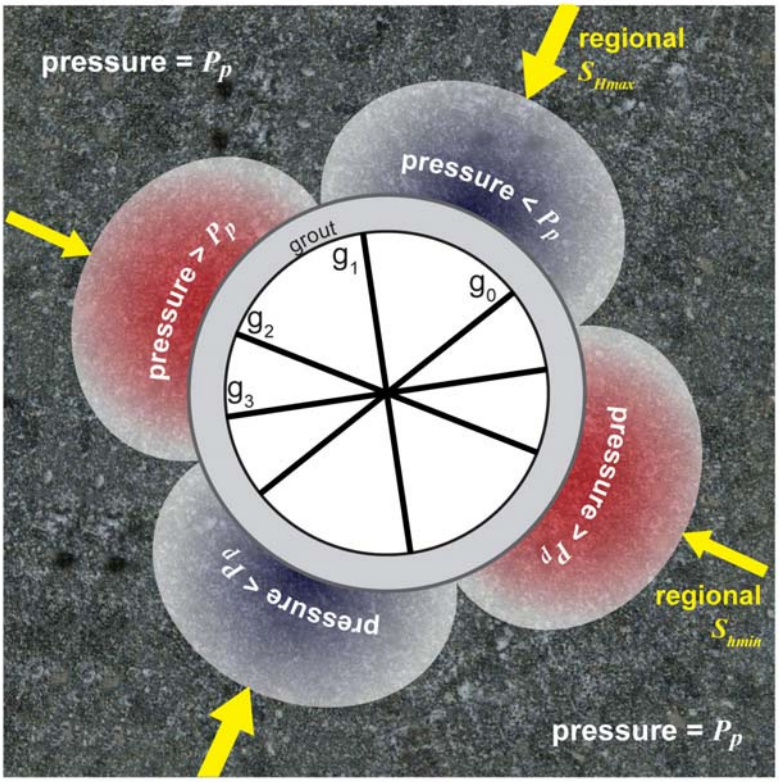

Figure 4–2. Conceptual illustration of the unequal pressure distribution set up around the borehole by the wellbore stress concentration, as given in Eqn. E4–9. View is of a horizontal cross-section through a vertical wellbore.

The effect of in situ pore pressure change on borehole stresses and deformation has been well explored. Jaeger et al. (2007) and Wang (2000) provide analytical solutions for the "short time" (undrained) and "long time" (drained) minimum and maximum circumferential stresses at the wall of a vertical wellbore but do not provide solutions for intermediate times. For the purpose of examining wellbore stability, Detournay and Cheng (1988) derive solutions for stresses near a vertical wellbore by solving for pore pressure and the induced stress components in the Laplace domain and providing illustrations of numerical results in the time domain. Importantly, their decomposition of the problem into three loading modes shows that

at the borehole wall, the response to isotropic stress is purely elastic (instantaneous), the maximum stress concentration due to the original, in situ pore pressure is also instantaneous, and the deviatoric far-field stress is the only load causing a time-dependent stress concentration. This stress concentration is seen primarily in the circumferential stress and is proportional to $\cos 2\theta$. The proportionality depends on the drained and undrained moduli and permeability. Cui et al. (1997) provide a similar solution for an inclined wellbore. The effects of constant wellbore fluid temperature and pressure different from the surrounding rock are described by Li et al. (1998a, 1998b). Finally, a thermoporoelastic solution for an inclined wellbore in a transversely isotropic medium is provided by Abousleiman et al. (1995).

4.3 Azimuthal Strain Distribution

4.3.1 PBO data

The San Andreas Fault Observatory at Depth (SAFOD), US Array, and the Plate Boundary Observatory (PBO) comprise the National Science Foundation's EarthScope program (see www.earthscope.org). PBO employs a network of Global Positioning Systems (GPS), laser strainmeters, and borehole strainmeters, to closely monitor ongoing deformation across the boundary between the Pacific and North American plates. All data collected as part of EarthScope are made available through the program's website.

PBO borehole strainmeters are four-component Gladwin Tensor Strainmeters (see Gladwin, 1984 and www.gtsmtechnologies.com). The wells in which they are installed are drilled and/or cored vertically (maximum bottom hole deviation is less than 10°) into primarily igneous and metamorphic rock and are carefully evaluated using core and/or logs to ensure that the instrument is installed in a substantial interval of intact rock. The strainmeters are carefully centered in the hole and then held in place using an expansive grout. Gauge orientations are determined using a magnetometer mounted on the strainmeter. Relative gauge orientations are fixed with three gauges 60° apart and a fourth gauge 30° from either neighbor in order to create an orthogonal gauge pair (see Fig. 4–2).

At the time of our analysis, PBO level 2 processed data—quality-controlled, calibrated data for which tidal, atmospheric and any other necessary corrections have been calculated—were available for twenty-one borehole strainmeters installed in the Pacific Northwest and California. The earliest data begin in June 2005 (wellbore B004), and the most recent begin in May 2007 (B036). Of these, three data sets have large intervals of missing data (B081, B082,

B089), five display sudden, large-magnitude increases or decreases in strain (B005, B007, B010, B082, B089), and five more have extreme, long-period strain fluctuations (B006, B011, B028, B036, B084). All of the strainmeters except B028 were installed using the same type of grout.

4.3.2 Analysis

Utilizing the approach of Detournay and Cheng (1988) and Li et al. (1998) for calculating poroelastic wellbore stress, we examined the azimuthal distribution of radial strain in a fictional wellbore for comparison to measured data. Lacking any data on in situ stress and rock properties for the strainmeter wells, we estimated reasonable values given the areas and rock types in which the PBO strainmeters were installed. Because the presence of the strainmeter creates an impermeable boundary at the wellbore wall, we set the initial difference in pore pressure between the borehole and its surroundings to zero in order to minimize fluid flow into or out of the wellbore (this differs from the published solutions in which the initial borehole is empty). Our results are shown in Fig. 4–3a, with detailed model parameters given in the figure caption. Most notably, radial strain magnitude shows a $\cos 2\theta$ distribution, as predicted by poroelasticity theory, and the rate of strain accumulation decreases with time.

Actual measured strain from PBO wellbore B004, located on the Olympic Peninsula, Washington is shown with asterisks in Fig. 4–3b. In this example, the gauge data have not been weighted. Using simple non-linear regression, we determined a best-fit, cosine (with frequency equal to 2) to the data from each day with excellent results, obtaining adjusted R-square values between 0.87 and 1.0. The south-southeast–north-northwest direction of maximum compression remains stable throughout the entire time period. Note that the fourth gauge, located 30° from its neighbors, is critical, because without it the cosine fit would be poorly constrained.

Clearly in both azimuthal distribution and decreasing rate of strain accumulation, the data match the model extremely well, although the absolute strain magnitudes between the data and the model are quite different. This difference is due to the contrast in elastic properties between the rock, grout, and strainmeter as described earlier (Gladwin and Hart, 1985; Agnew, 1986). In addition, the model solution is quite sensitive to the difference in the horizontal stress magnitudes; an increase of even just a few megapascals can cause a significant increase in the strain magnitudes while not affecting the relative rate of strain

accumulation, which is controlled primarily by permeability. The role of permeability will be discussed further in Section 4.6.

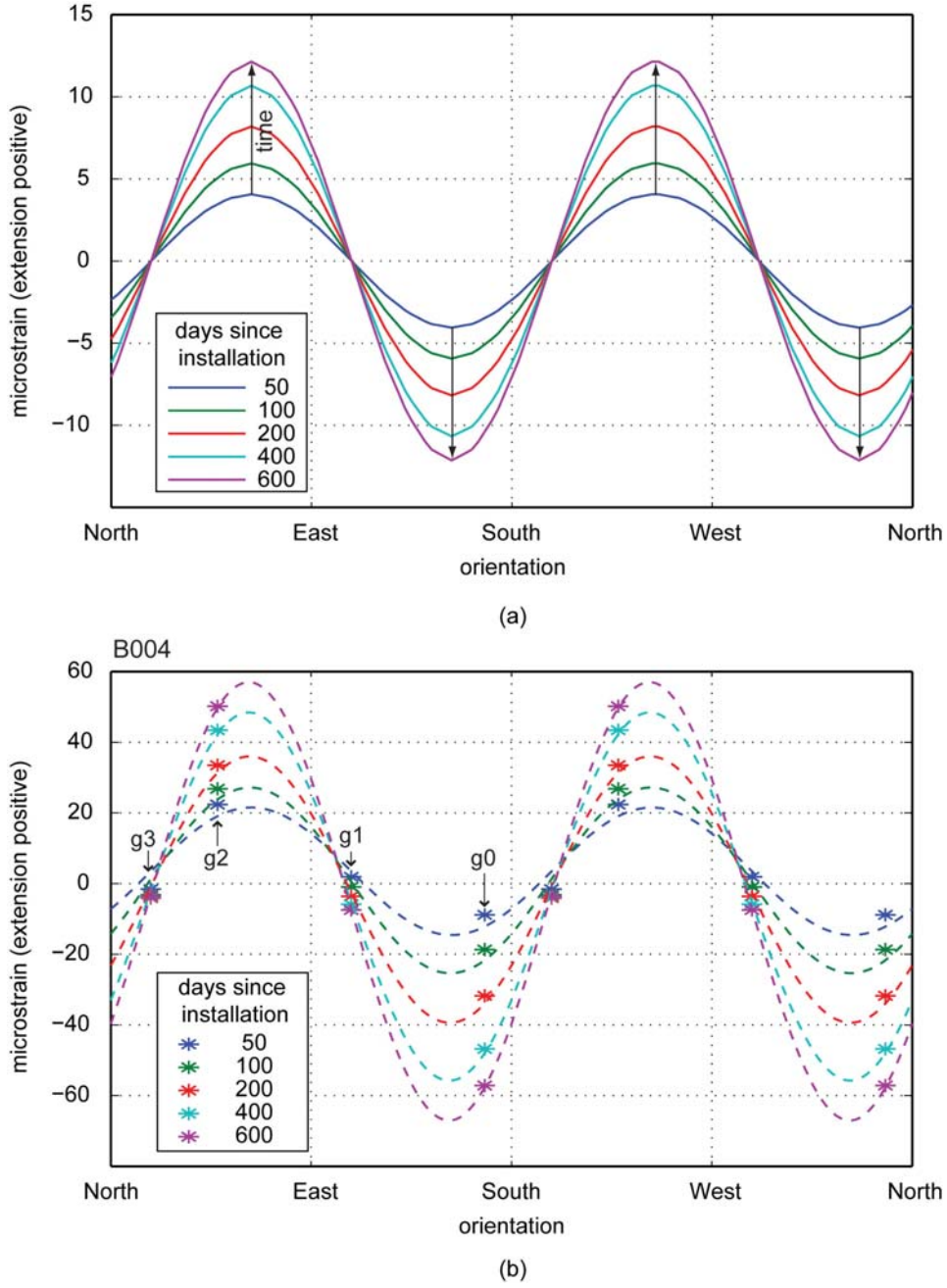

Figure 4–3. Modeled and measured radial strain as a function of azimuth in wellbore B004. The poroelastic solution for wellbore strain predicts a cosine distribution of radial strain with azimuth, with increasing amplitude over time (a). Non-linear regression shows that at any given time, measured strain (asterisks) also has a cosine distribution with a similar rate of increasing amplitude (b). See text for a discussion of the difference in absolute strain magnitudes. The parameters used in the model in (a) were: $S_{Hmax} - S_{hmin} = -10$ MPa with S_{Hmax} at 152°, $P_p = 1.75$ MPa, $\nu = 0.25$, $\nu_u = 0.35$, $B = 0.99$, Biot coefficient = 0.45, $G = 15$ GPa, porosity = 2%, permeability = 10^{-9} millidarcy, $R = 3$ in.

Another important difference between the observations and the model is an increasing downward shift of the cosines fit to the measured data, indicating radially uniform compression (note the increasing difference between the maximum positive and negative amplitudes of the cosine curves over time in Fig. 4–3b). Overall volumetric compression is expected in strainmeter data and is actually used as a check on whether or not a strainmeter is coupled adequately to the rock. In wellbore B004, as in about half of the other wells analyzed, an exponential of the form

$$D(t) = X_1 e^{Y_1 t} + X_2 e^{Y_2 t}, \qquad \text{(E4–10)}$$

where X_1, Y_1, X_2, and Y_2 are constants, best describes this offset. The offset in some other wells is better fit by a power law decay or a first- or second-order polynomial. An early source of uniform compression is expansion of the grout surrounding the strainmeter. While in B004 the magnitude of the offset is only about 5 to 10 microstrain over 600 days, which is small relative to the azimuthally dependent strain, in some other wells it is much greater, reaching up to approximately 10 microstrain per 100 days. This may be caused by temperature effects or a high-magnitude isotropic horizontal stress component, which the poroelastic wellbore stress solutions show do not cause azimuthally dependent stress and strain (Detournay and Cheng, 1988). Finally we note that all of the PBO wells in the Anza region of southern California show nearly as much, if not more, uniform compression as azimuthally dependent strain. This will be mentioned again when we discuss the possible contribution of viscoelastic rock behavior in Section 4.6.3.

In total we are able to fit a cosine strain distribution to six of the available PBO data sets (B004, B009, B081, B084, B087, and B089) with excellent results without having to weight any of the gauge data. In another five wells (B006, B007, B010, B036, B082), data problems such as those described in Section 4.3.1 prohibited successful analysis. In wells B018 and B086, despite no apparent problems with the data, the strain distribution around the wellbore did not fit our model. Figures of data and model fits for all of the wells are available in the appendix in Section 4.11.

Interestingly, for eight strainmeters we could obtain good analysis results only if we changed the assigned gauge orientations, in most cases just by shifting the assignments clockwise or counter-clockwise one gauge. These are B001, B005, B011, B012, B022, B028, B035, and P403. An example is shown for wellbore B012 in Figure 4–4. On the left are the strain measurements for 50, 100, 200, 400, and 600 days after installation located according to the originally assigned gauge orientations, with best-fit cosine curves. On the right are the

same data located according to revised gauge orientations, with new best-fit cosine curves. The insets illustrate the original and revised gauge orientations.

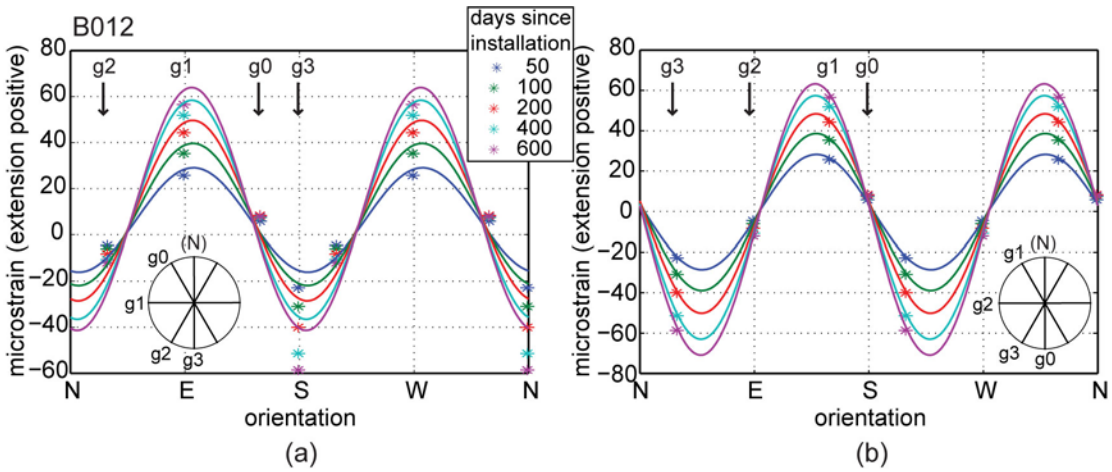

Figure 4–4. Strain data from wellbore B012 shown using the original (a) and revised (b) gauge orientations. Insets provide schematic instrument cross-sections showing gauge orientations in each case (with North up).

4.4 Long-term Strain Trends

In addition to describing the azimuthal distribution of strain at a given time, the results from the poroelastic model also give us, through non-linear regression, the form of the long term strain accumulation at any azimuth. The expression

$$\varepsilon_{rr}(t,\theta) = (-At^b + C)\cos 2\theta\,, \qquad \text{(E4–11)}$$

describes the accumulation of azimuthally dependent radial strain over time for the entire strainmeter. A, b and C are constants and have the same value for all θ. b, which is less than 1, accounts for a decrease in strain accumulation rate with time. C provides an offset to account for the arbitrary time when data collection started. The A term (including the exponent b) contains the primary effect of the poroelastic wellbore response to the in situ deviatoric stress. Parallel to S_{Hmax}, Eqn. E4–11 becomes

$$\varepsilon_{rr}(t,0^\circ) = -At^b + C\,, \qquad \text{(E4–12)}$$

which is equal to the maximum amplitude of the sinusoidal strain distribution around the wellbore determined in the previous section. Superimposing Eqn. E4–11 and the uniform strain, $D(t)$, we have a complete expression for the long-term strain measured by any gauge on a given strainmeter,

$$\varepsilon_{rr}\ \text{total} = (-At^b + C)\cos 2\theta + D(t). \qquad \text{(E4–13)}$$

To continue using wellbore B004 as an example, Figure 4–5 again compares our poroelastic model predictions to actual strainmeter data. Using the same model parameters as in the previous section, Figure 4–5a shows the predicted accumulation of strain over time at each of the B004 gauge orientations (168°, 108°, 48° and 18° for g0 through g3). Notice that since S_{Hmax} at this location is oriented at 153° (taken from the cosine fits to the B004 data), gauges 1 and 3 have $2\theta = 90°$, and therefore no strain should be recorded on these gauges. In the past, a lack of strain accumulation on a gauge has often been thought to indicate a problem with the instrument. In Figure 4–5b the actual gauge data are plotted with the uniform compression removed. Superimposed on the data are trends determined by multiple, non-linear regression using Eqn. E4–11 and constraining the constants A, b, and C to be the same for all gauges. In the long term, the trends fit the data extremely well. Differences in the early data can be attributed to short-time signals not accounted for in the long-term trend calculation (these are addressed more in the next section). For this wellbore, constants A, b, and C take on values of 5.377, 0.3993, and −7.009, respectively.

Figure 4–6 shows results from wellbores B009, B084, B087, and B089, the remaining four installations for which the azimuthal strain distribution fits our model using the default gauge orientation assignments (see previous section). Wellbore B009 is located on Vancouver Island, British Columbia, while the remaining wellbores shown are all located in the Anza region of southern California. Clearly despite large fluctuations in the gauge data or late starts in data availability, trends described by Eqn. E4–11 fit quite well. The very small fluctuations in the data from wellbore B084 are due to atmospheric signals; no atmospheric correction was available for the first three months of data, so the entire data set has been analyzed without that correction. The large fluctuations in wellbore B089 after about day 200 are attributed to site disturbances and pumping in nearby wells.

In the wells that require changing the gauge orientations to get a good azimuthal strain distribution (B001, B005, B011, B012, B022, B028, B035, and P403, see previous section), our trend model fits the data only after the gauge orientation reassignments are made. Figure 4–7 shows an example from wellbore B005. Despite obvious artifacts in the data, the overall trend fits using the gauge reassignments (Fig. 4–7b) are excellent. Figures for the remaining wells can be found in the appendix in Section 4.11.

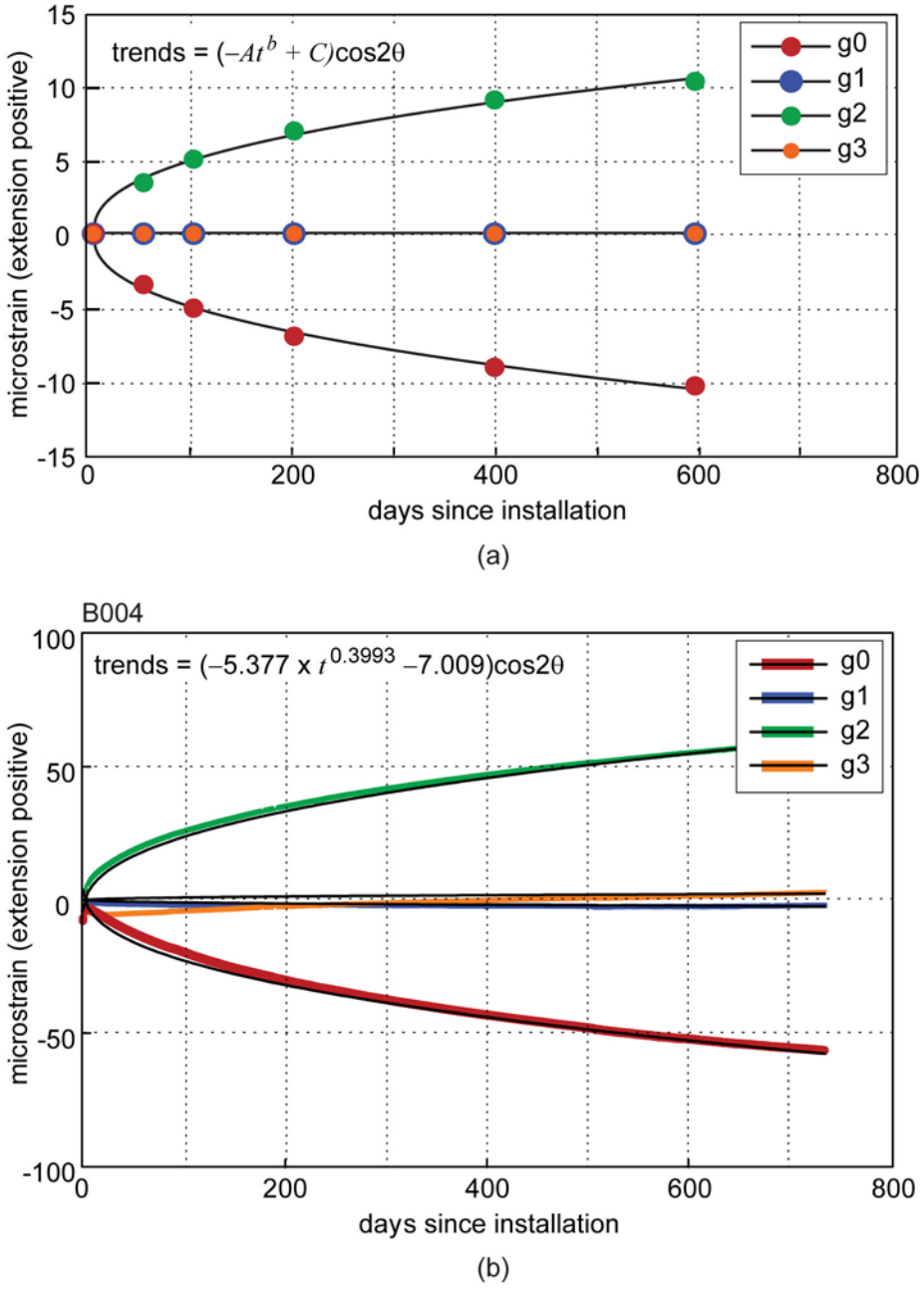

Figure 4–5. Modeled and measured radial strain as a function of time in wellbore B004. The poroelastic solution for wellbore strain predicts a long-term trend which is a function of $\cos 2\theta$, where θ is the angle between S_{Hmax} (here oriented at 153°) and the gauge (a). The constants in the trend expression are the same for all gauges. Non-linear regression shows that the measured long-term strain follows the same function of $\cos 2\theta$ (b), but with different coefficients than in (a) to account for the difference in absolute magnitudes. (See Fig. 4–3 for model parameters.)

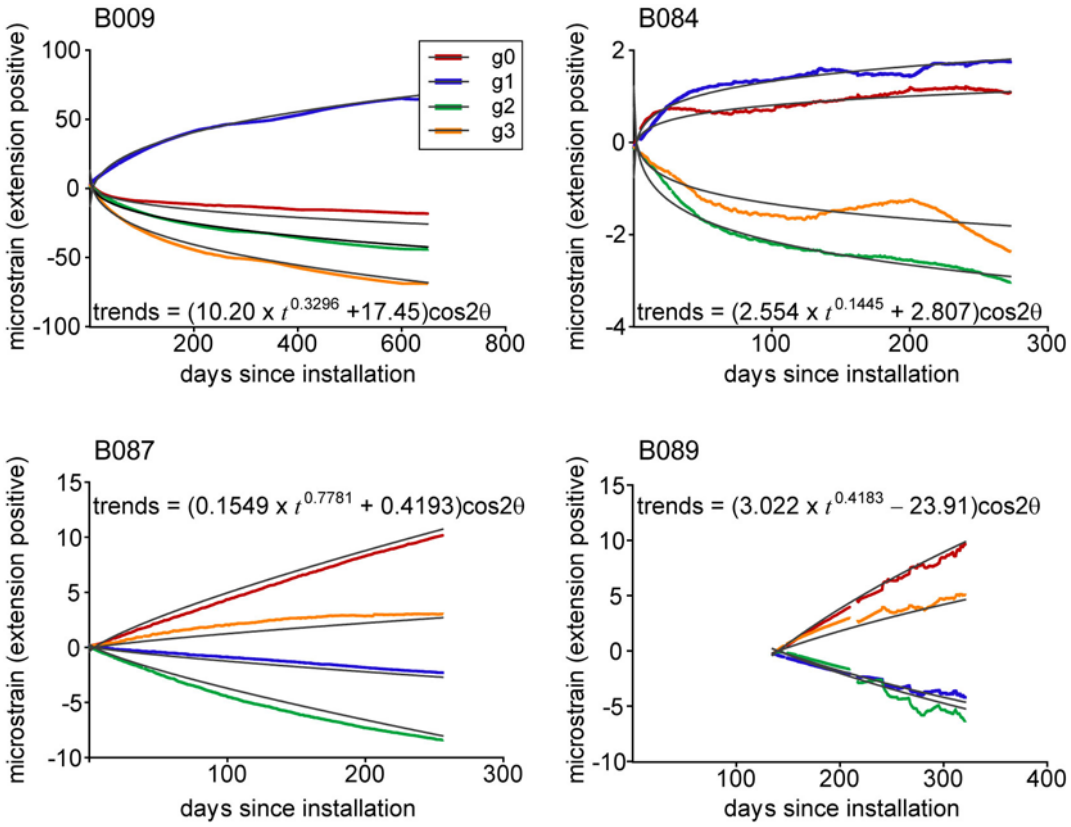

Figure 4–6. Trends calculated using Eqn. E4–9 [after removal of radially uniform strain, *D(t)*] for data from four PBO wellbores. See text for explanation of trend parameters.

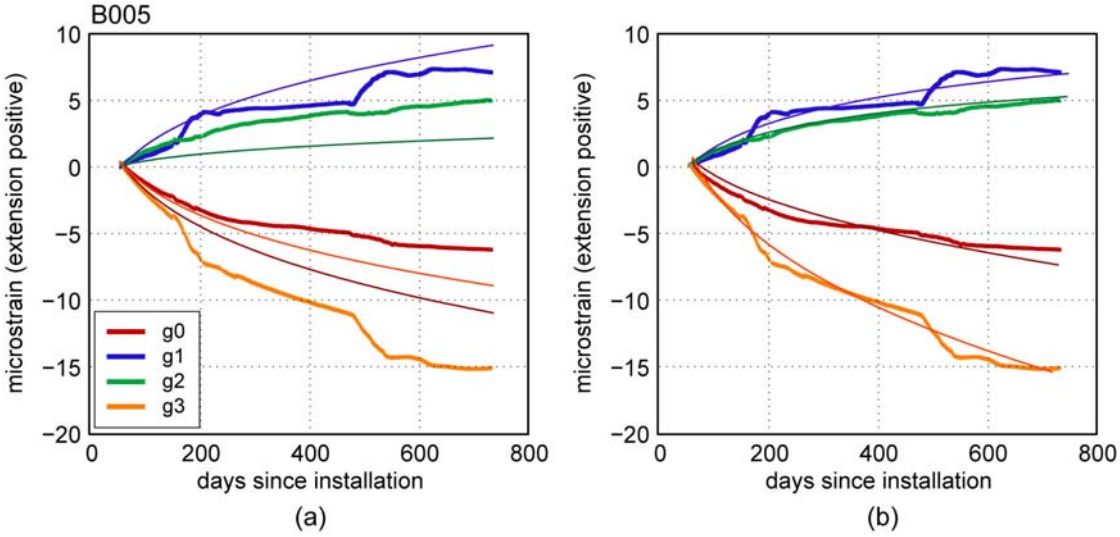

Figure 4–7. Trends calculated using Eqn. E4–9 [after removal of radially uniform strain, *D(t)*] for data from wellbore B005. a) Results using original gauge orientations. b) Results using reassigned gauge orientations.

4.5 Comparison with Regional Stress Data

As described in Section 4.3, we are able to determine the direction of the maximum horizontal stress, S_{Hmax}, at each strainmeter from the direction of maximum compression in the azimuthal distribution of radial strain. Because in situ stress orientations are controlled by large-scale tectonic processes and plate boundary forces (e.g., Flesch et al., 2000; Humphreys and Coblentz, 2007), they are generally consistent in a given region (Zoback and Zoback, 1980; Zoback et al., 1989). Figures 4–8 and 4–9 show available stress orientation data in the Pacific Northwest, coastal Oregon, and the Anza region of southern California. Focal mechanism data are from the World Stress Map (Reinecker et al., 2005), and the yellow circles with black or orange lines through them show S_{Hmax} directions from the PBO strainmeter data analyzed in this study (wellbores with very poor data have gray numbers and no stress direction plotted). In some cases, such as B004 (Fig. 4–8a) and B089 (Fig. 4–9) the strainmeter data agree quite well with the regional stress data. Cases in which we needed to change the gauge orientations to get decent sinusoidal strain distributions are shown in orange, with the solid line being the direction determined using the original gauge orientations and the dashed line being the direction determined using the new gauge assignments. In wellbores B001, B012, B028, and B035 changing the gauge orientations improves the match to the regional stress data, whereas in B005, B022, and P403 it actually makes the match worse. Unfortunately, this exercise does not resolve the issue of whether or not it is truly necessary to change the gauge orientations.

Given that the majority of stress indicators, such as earthquakes and wellbore failure (Zoback and Zoback, 1980), come from depths that greatly exceed typical strainmeter installation depths of 150 to 200 meters, variation between stress directions from strainmeters and those from these other sources is expected. Near the surface, in situ stress magnitudes are relatively low and likely to be perturbed by local phenomena such as topography. However, our results show that at least in some cases, the strainmeter data seem to reflect the regional in situ stress state.

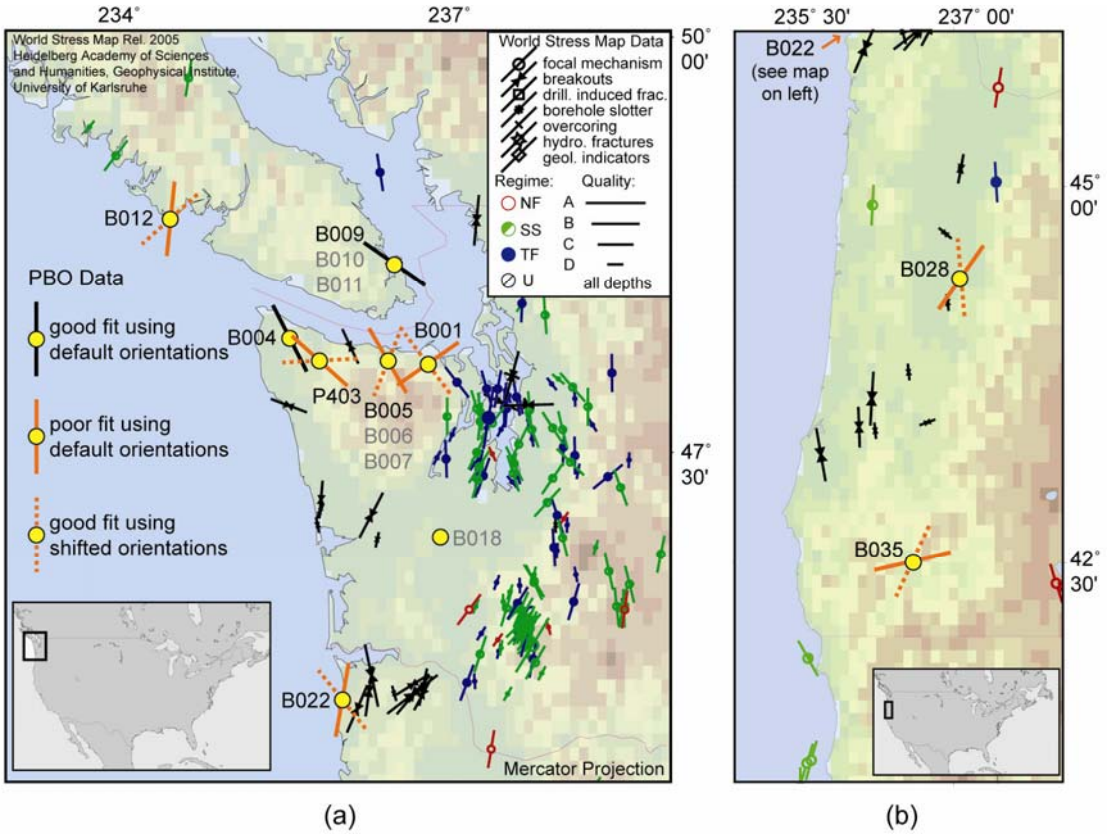

Figure 4–8. Stress maps of the Pacific Northwest region (a) and coastal Oregon (b) showing S_{Hmax} orientation data from both the World Stress Map (see legend) and our interpretation of data from PBO strainmeters (yellow and black or yellow and orange symbols).

4.6 Discussion

4.6.1 Comparison with the Traditional Detrending Approach

Our physically based expression for the long-term strain trends provides a new means of detrending the data from the individual strainmeter gauges. In Figure 4–10 we compare the results of using our approach of Eqn. E4–13 (left-hand plots) and those using the traditional, curve-fitting approach of Eqn. E4–1 (right-hand plots) to detrend data from wellbore B084. All of the steps in the detrending process are illustrated, including the determination of the residual strain on each gauge and calculation of areal strain from two different sets of gauges (the three, equally spaced gauges and the two, orthogonal gauges). We chose this wellbore despite its lack of atmospheric signal correction (see Section 4–3) because the data show some interesting, relatively large fluctuations around the long-term trends. While the mean residuals are similar using either method, there are some important differences. For example, our

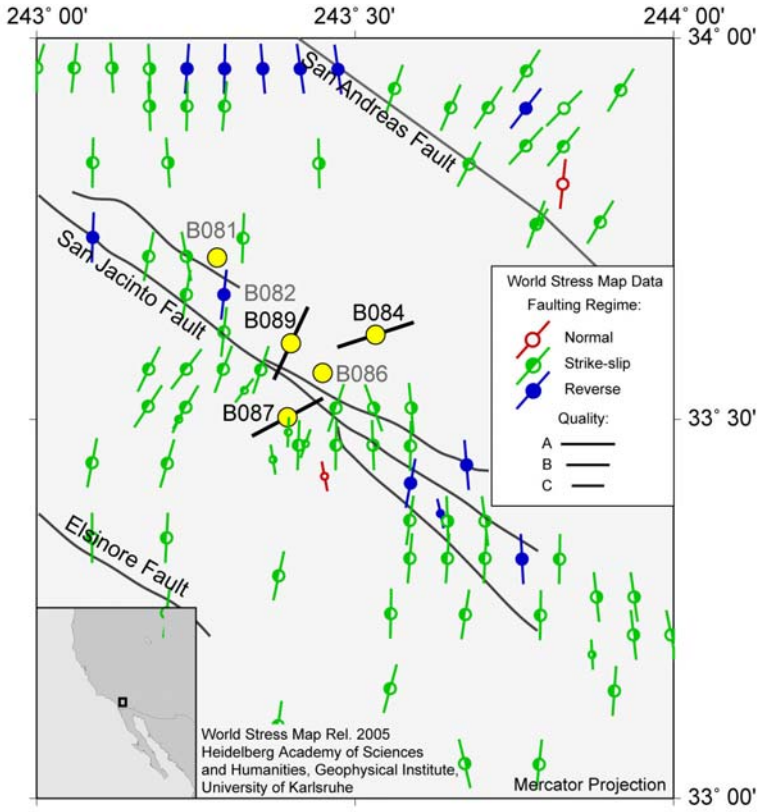

Figure 4–9. Stress map of the Anza region, southern California, showing S_{Hmax} orientation data from both the World Stress Map (see legend) and our interpretation of data from PBO strainmeters (yellow and black symbols).

approach shows a significant compression in the areal strain after about day 200, while the traditional detrending approach indicates extension. It is clear from the figure that the dominant component of the mathematical trends is the strong compressional signal seen on each gauge (top right). In contrast, by removing the uniform compression from all of the gauges prior to determining the azimuthally dependent strain, our model-based approach is better able to resolve small-scale differences between the four gauges.

It is important to remember that we address long-term strain trends only. In the first weeks after installation, many of the strainmeters experience rapid accumulation of either compressional or extensional strain on one or more gauges, and there is often quite a bit of variability in these signals. The mathematical detrending approach is able to account for these signals by assigning a unique mathematical expression to each gauge, including a short-time exponential term. In our study we sometimes needed to start our analysis a few days or weeks after installation in order to avoid artifacts caused by these short-term signals in the long-term accumulated strain amounts. Further effort is certainly called for to determine the physical

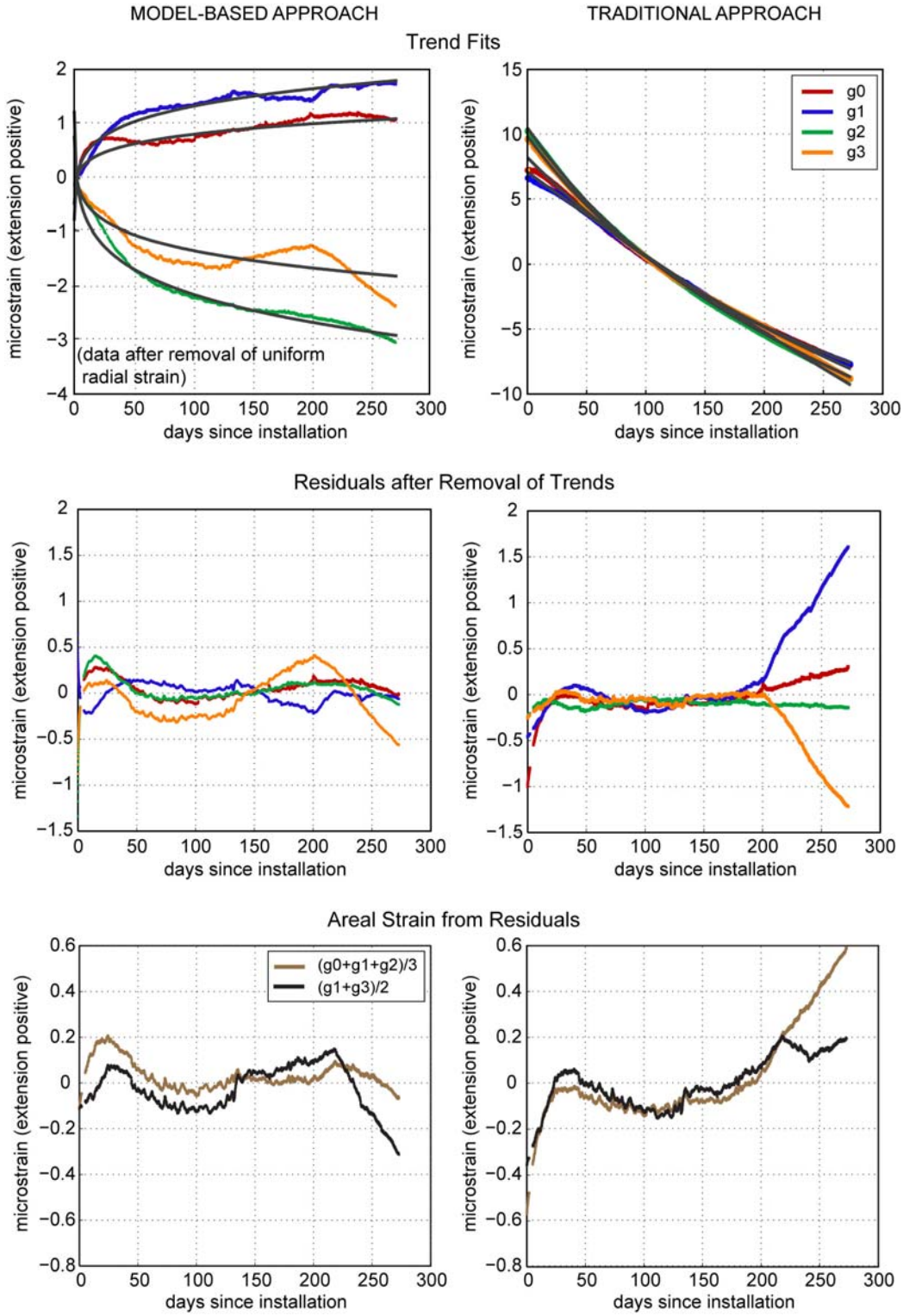

Figure 4–10. Comparison of the model-based detrending approach developed in this thesis (left panels) versus the traditional detrending technique (right panels) on data from wellbore B084. *Top*: trends fit to the data (on left, data are shown with uniform compression removed); *middle*: residual strain after trends are removed; *bottom*: areal strain calculated from the residuals.

cause(s) of the early signals so that they can be accurately removed from the data along with the long-term trend.

4.6.2 Parameter Estimation

As discussed in Section 4.4, our approach for determining long-term strain trends has the practical advantage of not requiring knowledge of any parameters except for the orientation of each gauge relative to the direction of maximum horizontal compression, which is easily determined from the azimuthal distribution of radial strain. It has the scientific disadvantage, however, of thus not providing specific information about the properties of the surrounding rock. Unfortunately, estimating the values of A and b a priori rather than finding them from a best-fit model would be extremely difficult. As with the elastic ring model described earlier, the biggest challenge in applying poroelasticity theory at a given location is constraining the many parameters and material properties needed. Analytical solutions to the poroelastic stress concentration are complicated and depend strongly on these parameters and various combinations of them (Detournay and Cheng, 1988). It is known that the effects of water table changes from pumping in nearby wells or seismic events can sometimes be seen in borehole instrument data and may reveal some information about the properties of the surrounding rock (e.g., Kümpel et al., 1999; Roeloffs and Quilty, 1997; Segall et al., 2003). These signals, however, can be complicated by factors such as nearby hydraulically conductive fractures (Evans and Wyatt, 1984). Besides, the inevitable uncertainties in any parameter estimates will introduce errors that could easily affect the very small residual strains left after detrending.

One of the outstanding issues in our analysis is the need to use a very low rock permeability in order for the pore pressure perturbation to last for a relatively long time. In our model for B004, for example (Figs. 4–3 and 4–5), we used a permeability of 10^{-9} millidarcy. This is at the extreme low end of the range for even intact laboratory specimens of crystalline rock (Clauser, 2001). Increasing this to 10^{-8} millidarcy limits the accumulation of poroelastic strain to the first 100 or so days instead of several hundred days as seen in the data. However, as mentioned in Section 4.3.2, the poroelastic solutions of Detournay and Cheng (1988) and Li et al. (1998) assume an initially empty borehole and rapid draining of fluid into it from the surrounding rock. The implementation of these solutions that we used in our analysis did not allow for an impermeable boundary at the wellbore wall. Although we tried to minimize the pressure difference between the wellbore and surrounding rock by setting the initial borehole fluid pressure equal to the formation pore pressure, some flow was still allowed into and out of

the borehole as the wellbore stress concentration increased or decreased the fluid pressure in the surrounding rock. The permeability we used, therefore, is an effective permeability, and the real permeability should be somewhat higher. It is still reasonable, however, to consider other time-dependent processes that might be contributing to the observed long-term accumulation of strain.

4.6.3 Viscoelasticity

As mentioned in the introduction, long-term deformation of strainmeter wellbores has historically been attributed to viscous relaxation of the surrounding rock (Gladwin et al., 1987; Sakata, 2005). The mathematical trend expression in Eqn. E4–1, although somewhat arbitrary, does in fact have the general form of an expression for rock creep where the constant term accounts for the instantaneous elastic strain, one of the exponential terms describes transient creep at relatively early times, the linear term accounts for steady state creep, and the other exponential describes accelerating creep at later times due primarily to damage of the material (Jaeger et al., 2007, Eqn. 9.82). It does not, however, account for the presence of the original in situ stresses and their effect on the wellbore stress concentration.

Sources of viscous behavior in rocks can include processes such as opening and closing of microscopic cracks, changes in grain contacts, or grain rearrangement via clays and other ductile minerals (Cristescu and Hunsche, 1998; Jaeger et al., 2007). Several models for viscoelastic solids have been developed to explain time-dependent deformation observed in different rock types for a variety of loading conditions. In general, however, lab experiments (Lomnitz [1956] on igneous rocks) and field-scale data (Savage et al., 2005) both support the existence of strain relaxation through creep over significantly long time periods even at low temperatures and pressures. Historically this kind of strain recovery has found widespread application in such practices as overcoring and stress-relief measurements for determining in situ stress (Barla and Wane, 1968; Engelder, 1993).

Following the general, three-loading-modes approach of Detournay and Cheng (1988) and using a generalized Kelvin model for a viscoelastic solid, Abousleiman et al. (1993) develop a solution for stress and displacement in an empty borehole drilled in rock that behaves both poroelastically and viscoelastically. Their examples illustrate that when viscoelastic effects are present in the form of a time-dependent bulk modulus, azimuthally dependent radial displacement can be significantly larger than for the poroelastic solution alone. Interestingly, the purely poroelastic solution and the poroviscoelastic solution are the

same at early times, but the poroviscoelastic solution continues to show strain accumulation for much longer than the poroelastic solution alone. In addition, they show that a time-dependent shear modulus will cause an azimuthally uniform, time-dependent radial displacement that is not present at all in the purely poroelastic solution (Detournay and Cheng, 1988). This may explain some of the large uniform compressive strains observed in a few of PBO datasets (e.g., in the Anza wellbores B084, B087, and B089), but in general we do not see evidence of this in most of the wellbores studied.

In general, we do not favor the viscoelastic solution. Even in the few cases where there may be a significant viscoelastic contribution to the measured strain, it is extremely difficult to constrain that contribution through modeling because of the large uncertainties in selecting the time-dependent parameters and creep laws controlling the viscoelastic behavior.

4.6.4 Gauge Orientations

The issue of whether or not gauge orientation reassignments are needed, which our analysis suggests they are, is currently under debate. Arrivals of Rayleigh and Love waves from distant events captured by the strainmeters do not, upon preliminary investigation, support rearranging gauges (E. Roeloffs and W. McCausland, 2007, pers. comm.). Additional work is being done to see if calibration using tidal and/or atmospheric signals in particular wells is improved by reorienting gauges (K. Hodgkinson, 2007, pers. comm.), or whether gauge assignments may get switched somewhere in the data stream or processing procedure (M. Gladwin, 2007, pers. comm.).

The general consensus among scientists working on PBO strainmeter data and installations is that there should not be errors in the gauge assignments. It is considered more likely that applying gauge weights might improve the fit of the data to our models in the wells under question. Progress on this option awaits receiving gauge weight assignments, and justification for them, from scientists handling the strainmeter data. There is too much ambiguity in using our approach to find gauge weights; several sets of applied weights could provide better fits to the model in any given wellbore.

Another possible source of inconsistencies between gauges is anisotropic elastic properties in the rock surrounding the wellbore. This could derive, for example, from layered rock or the presence of natural fractures. Wellbore B022 is the most likely candidate to experience this effect, since the strainmeter is installed in sandstone, whereas the others are installed in igneous or metamorphic rock. Two of the Anza wells, B082 and B089, are

installed in gneiss, in which foliation might cause anisotropy, but neither of these wells requires gauge reorientation. The effect of anisotropy can be modeled by modifying the existing poroelastic wellbore solutions to include direction-dependent rock properties (see Abousleiman et al., 1995). While the additional azimuthally dependent component of strain from the anisotropy will provide a sort of weight for each gauge, these will be physically meaningful adjustments rather than somewhat arbitrary scaling factors.

4.7 Conclusions

The wellbore stress concentration has long been overlooked in borehole strain measurements. Not only has this resulted in widespread use of a detrending procedure with no physical basis, it has also potentially led to erroneous interpretation of the residual strain data. In addition, meaningful information about the in situ stress state has been simply thrown out with the long-term trends.

In much of the PBO strainmeter data available so far we see an azimuthal distribution and long-term accumulation of radial strain that matches what we expect from poroelasticity theory. Using our poroelastic model, we have developed a detrending approach that has a firm physical basis, making the residual signals left after the detrending step more meaningful. By requiring no parameters except the orientation of the maximum horizontal in situ stress, which is easily determined from the data before detrending, our approach is extremely easy to use. Much room for future work remains, for example, to resolve the gauge orientation/weighting issue, characterize the very early signals in the data, and quantitatively examine the contribution of viscoelastic deformation.

4.8 Acknowledgments

Thanks to GeoMechanics International, Inc., especially Dr. Pavel Peška, for making GMI·SFIB™ available for this work. Thanks also to UNAVCO and the entire PBO borehole strainmeter team but in particular Evelyn Roeloffs (United States Geological Survey) and Kathleen Hodgkinson (UNAVCO) for their encouragement, helpful discussions and workshops, and assistance in accessing and evaluating the PBO strainmeter data. We also appreciate support from the Stanford Rock and Borehole Geophysics Project.

4.9 Explanation of Symbols

A	constant in poroelastic trend
A_1, A_2	constants in mathematical trends
B	Skempton's pore pressure coefficient
b	constant in poroelastic trend
C	constant in poroelastic trend
$D(t)$	function describing azimuthally uniform strain
F	constant in mathematical trends
G	shear modulus
K_u	undrained bulk modulus
k	permeability
P_p	unperturbed formation pore pressure
p	pore pressure
R	wellbore radius
r	radial distance from wellbore axis
S_{Hmax}	maximum in situ horizontal compressive stress
S_{hmin}	minimum in situ horizontal compressive stress
T_1, T_2	constants in mathematical trends
t	time in days
X_1, X_2	constants in $D(t)$
Y_1, Y_2	constants in $D(t)$
α	Biot effective stress coefficient
ε_{rr}	radial strain
ν	drained Poisson's ratio
ν_u	undrained Poisson's ratio
σ_{rr}	radial wellbore stress
$\sigma_{\theta\theta}$	circumferential wellbore stress
σ_{zz}	vertical wellbore stress
θ	angle from azimuth of S_{Hmax}

4.10 References

Abousleiman, Y., A. H. -D. Cheng, C. Jiang, and J. -C. Roegiers (1993), A micromechanically consistent poroviscoelasticity theory for rock mechanics applications, *Int. J. Rock Mech. Min. Sci. Geomech. Abstr.*, *30*, 1177–1180.

Abousleiman, Y., J. -C. Roegiers, L. Cui, and A. H.-D. Cheng (1995), Poroelastic solution of an inclined borehole in a transversely isotropic medium, in *Proceedings of the 35th U.S. Symposium on Rock Mechanics*, 313–318.

Agnew, D. C. (1986), Strainmeters and tiltmeters, *Rev. Geophys.*, *24*, 579–624.

Barla, G., and M. T. Wane (1968), Analysis of the borehole stress-relief method in rocks with rheological properties, *Int. J. Rock Mech. Min. Sci. Geomech. Abstr.*, *5*, 187–193.

Biot, M. A. (1941), General theory of three–dimensional consolidation, *J. Appl. Phys., 12*, 155–164.

Clauser, C. (2001), Update of the permeability of crystalline rocks, www.geophysik.rwth–aachen.de/html/perm.htm.

Cristescu, N., and U. Hunsche (1998), *Time Effects in Rock Mechanics*, 342 pp., Wiley, New York.

Cui, L., A. H.-D. Cheng, and Y. Abousleiman (1997), Poroelastic solution for an inclined borehole, *J. Appl. Mech.*, *64*, 32–38.

Detournay, E., and A. H.-D. Cheng (1988), Poroelastic response of a borehole in a non-hydrostatic stress field, *Int. J. Rock Mech. Min. Sci. Geomech. Abstr.*, *25*, 171–182.

Engelder, T. (1993), *Stress Regimes in the Lithosphere*, 457 pp., Princeton University Press, Princeton, NJ.

Evans, K., and F. Wyatt (1984), Water table effects on the measurement of Earth strain, *Tectonophysics*, *108*, 323–337.

Flesch, L. M., W. E. Holt, A. J. Haines, and B. Shen-Tu (2000), Dynamics of the Pacific–North American Plate boundary in the western United States, *Science, 287*, 834–836.

Gladwin, M. T. (1984), High precision multicomponent borehole deformation monitoring, *Rev. Sci. Instr.*, *55*, 2011–2016.

Gladwin, M. T., and R. Hart (1985), Design parameters for borehole strain instrumentation, *Pure Appl. Geophys.*, *123*, 59–80.

Gladwin, M. T., R. L. Gwyther, R. Hart, and M. Francis (1987), Borehole tensor strain measurements in California, *J. Geophys. Res., B*, *92*, 7981–7988.

Gladwin, M. T., R. L. Gwyther, R. H. G. Hart, and K. S. Breckenridge (1994), Measurements of the strain field associated with episodic creep events on the San Andreas fault at San Juan Bautista, California, *J. Geophys. Res., B*, *99*, 4559–4565.

Gwyther, R. L., M. T. Gladwin, M. Mee, and R. G. Hart (1996), Anomalous shear strain at Parkfield during 1993-94, *Geophys. Res. Lett.*, *23*, 2425–2428.

Hart, R. H. G., M. T. Gladwin, R. L. Gwyther, D. C. Agnew, and F. K. Wyatt (1996), Tidal calibration of borehole strainmeters: Removing the effects of local inhomogeneity, *J. Geophys. Res., B*, *101*, 25553–25571.

Humphreys, E. D., and D. D. Coblentz (2007), North American dynamics and western U.S. tectonics, *Rev. Geophys., 45*, doi:10.2019/2005RG000181.

Jaeger, J. C., N. G. W. Cook, and R. W. Zimmerman (2007), *Fundamentals of Rock Mechanics*, 4th ed., Blackwell Publishing, Malden, MA.

Johnston, M. J. S., A. T. Linde, and D. C. Agnew (1994), Continuous borehole strain in the San Andreas fault zone before, during, and after the 28 June 1992, M_W 7.3 Landers, California, earthquake, *Bull. Seismol. Soc. Am.*, *84*, 799–805.

Kirsch, V. (1898), Die theorie der elastizitat und die beddurfnisse der festigkeitslehre, *Zeitschrift des Vereines Deutscher Ingenieure, 29*, 797–807.

Kümpel, H. J., G. Grecksch, K. Lehmann, D. Rebscher, and K. C. Schulze (1999), Studies of in situ pore pressure fluctuations at various scales, *Oil Gas Sci.Technol.*, *54*, 679–688.

Li, X., L. Cui, and J. -C. Roegiers (1998a), Thermoporoelastic modelling of wellbore stability in non-hydrostatic stress field, *Int. J. Rock Mech. Min. Sci. Geomech. Abstr.*, *35*, 584.

Li, X., L. Cui, and J. -C. Roegiers (1998b), Thermoporoelastic analyses of inclined boreholes, paper presented at SPE/ISRM Eurock ’98, Trondheim, Norway, 8-10 July.

Lomnitz, C. (1956), Creep measurements in igneous rocks, *J. Geol.*, *64*, 473–479.

Reinecker, J., O. Heidbach, M. Tingay, B. Sperner, and B. Müller (2005), The 2005 release of the World Stress Map, www.world-stress-map.org.

Rice, J. R., and M. P. Clearly (1976), Some basic stress-diffusion solutions for fluid-saturated elastic porous medium with compressible constituents, *Rev. Geophys. Space Phys.*, *14*, 227–241.

Roeloffs, E. A. (2006), Evidence for aseismic deformation rate changes prior to earthquakes, *Ann. Rev. Earth Planet. Sci.*, *34*, 591–627.

Roeloffs, E. A., and E. Quilty (1997), Case 21: Water level and strain changes preceding and following the August 4, 1985 Kettleman Hills, California, earthquake, *Pure Appl. Geophys.*, *149*, 21–60.

Sakata, S. (2005), In situ measurement of rock viscosities by Sakata-type three-component strainmeters, in *5th U.S.-Japan Natural Resources Meeting and Parkfield, California Field Trip*, pp. 55–56, U. S. Geological Survey.

Savage, J. C., J. L. Svarc, and S.-B. Yu (2005), Postseismic relaxation and transient creep, *J. Geophys. Res., B*, *110*, doi:10.1029/2005JB003687.

Segall, P., S. Jonssón, and K. Ágústsson (2003), When is the strain in the meter the same as the strain in the rock?, *Geophys. Res. Lett.*, *30*, 1990, doi:1910.1029/2003GL017995.

Spathis, A. T. (1988), A biaxial viscoelastic analysis of hollow inclusion gauges with implications for stress monitoring, *Int. J. Rock Mech. Min. Sci. Geomech. Abstr.*, *25*, 473–477.

Wang, H. F. (2000), *Theory of Linear Poroelasticity with Applications to Geomechanics and Hydrogeology*, 287 pp., Princeton University Press, Princeton.

Wyatt, F. K., and D. C. Agnew (1998), Piñon Flat Observatory: Continuous monitoring of crustal deformation, 5 pp., in *Southern California Earthquake Center Executive Summary*.

Yoshikawa, S., T. Yamamoto, O. Kamigaichi, and H. Naito (2001), Strain measurement by double coaxial borehole strainmeters at Odawara, Japan, *14th international symposium on Earth tides*, *47*, 128–133.

Zoback, M. L. (1992), First- and second-order patterns of stress in the lithosphere: The World Stress Map project, *J. Geophys. Res., B, 97*, 11703–11728.

Zoback, M. L., and M. D. Zoback (1980), State of stress in conterminous United States, *J. Geophys. Res., B, 85*, 6,113–116,156.

Zoback, M. L., M. D. Zoback, J. Adams, M. Assumpção, S. Bell, E. A. Bergman, P. Blümling, N. R. Brereton, D. Denham, J. Ding, K. Fuchs, N. Gay, S. Gregersen, H. K. Gupta, A. Gvishiani, K. Jacob, R. Klein, P. Knoll, M. Magee, J. L. Mercier, B. Müller, C. Paquin, K. Rajendran, O. Stephansson, G. Suarez, M. Suter, A. Udias, Z. H. Xu, and M. Zhizhin (1989), Global patterns of tectonic stress, *Nature, 341*, 291–298.

4.11 Appendix

This appendix contains a summary of our analysis of all of the PBO strainmeters for which data were available at the time of our study. Table A4–1 provides a list of all of the wellbores giving location, installation depth, whether or not the data were usable for our analysis, and our success in trying to fit a poroelastic model to the data (*default* means the model fit well using the reported gauge orientations, *reoriented* means we needed to change gauge orientation assignments to achieve reasonable results, *none* means no rearrangement of gauges resulted in the expected strain distribution, and *n/a* means the data quality was so poor as to preclude analysis). Figures for each wellbore with usable data include cosine fits to the azimuthal distribution of strain as well as trends fit to the strain measured by each gauge over time. Both the default and rearranged cases are shown for wellbores in which gauge reassignments considerably improved the fits. Gauge orientations and trend parameters are given for each. The wells are presented in numerical order (P403 is last).

Wellbore	Location	Installation Depth (m)	Data Usable?	Model Fit
B001	PNW	153	yes	reoriented
B004	PNW	166	yes	default
B005	PNW	161	yes	reoriented
B006	PNW	157	no	n/a
B007	PNW	140	no	n/a
B009	PNW	225	yes	default
B010	PNW	199	no	n/a
B011	PNW	225	yes	reoriented
B012	PNW	170	yes	reoriented
B018	Oregon	226	yes	none
B022	PNW/Oregon	220	yes	reoriented
B028	Oregon	240	yes	reoriented
B035	Oregon	226	yes	reoriented
B036	Oregon	182	no	n/a
B081	Anza	243	yes	default
B082	Anza	243	no	n/a
B084	Anza	159	yes	default
B086	Anza	240	yes	none
B087	Anza	161	yes	default
B089	Anza	133	yes	default
P403	PNW	170	yes	reoriented

Table 4A–1. Summary of all of the strainmeters for which data were available for our study.

B001

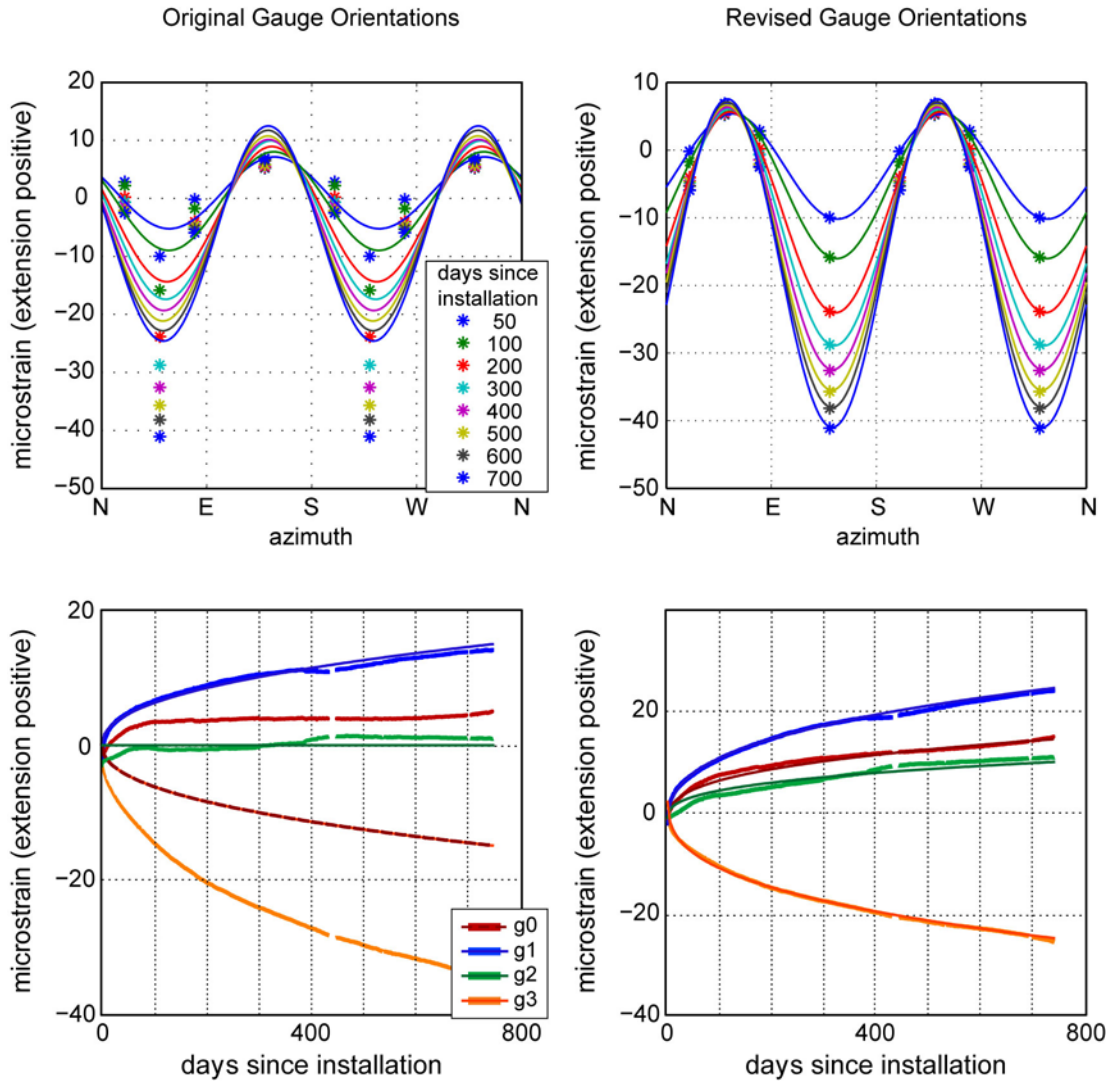

S_{Hmax} Orientation

	55°
	145°

Gauge Orientations

g0	200°	**g0**	80°
g1	140°	**g1**	50°
g2	80°	**g2**	200°
g3	50°	**g3**	140°

Trend Parameters

A	1.044	***A***	3.112
b	0.4262	***b***	0.3338
C	0.2606	***C***	3.605

B004

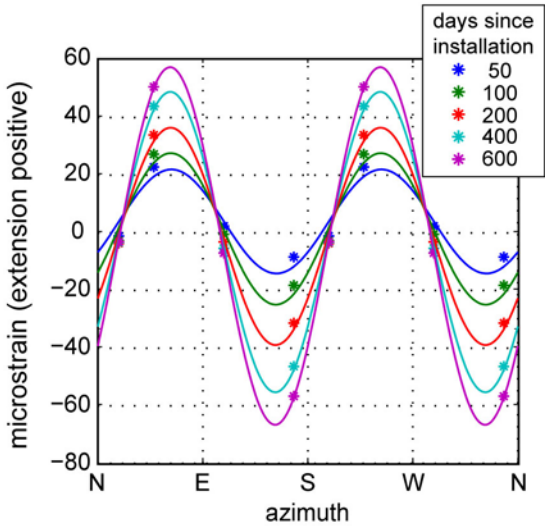

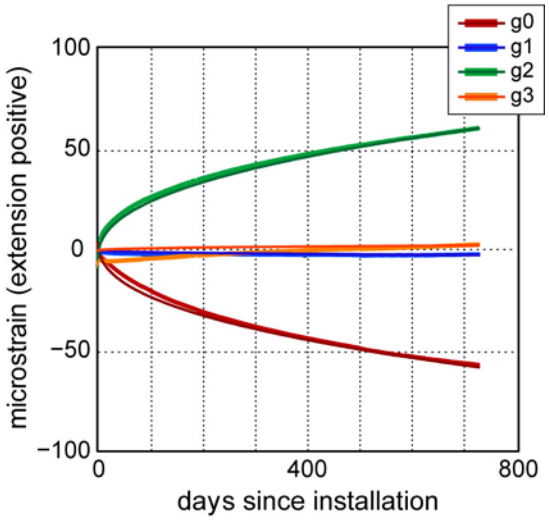

S_{Hmax} Orientation

152°

Gauge Orientations

g0	168°
g1	108°
g2	48°
g3	18°

Trend Parameters

A	5.337
b	0.3993
C	7.009

B005

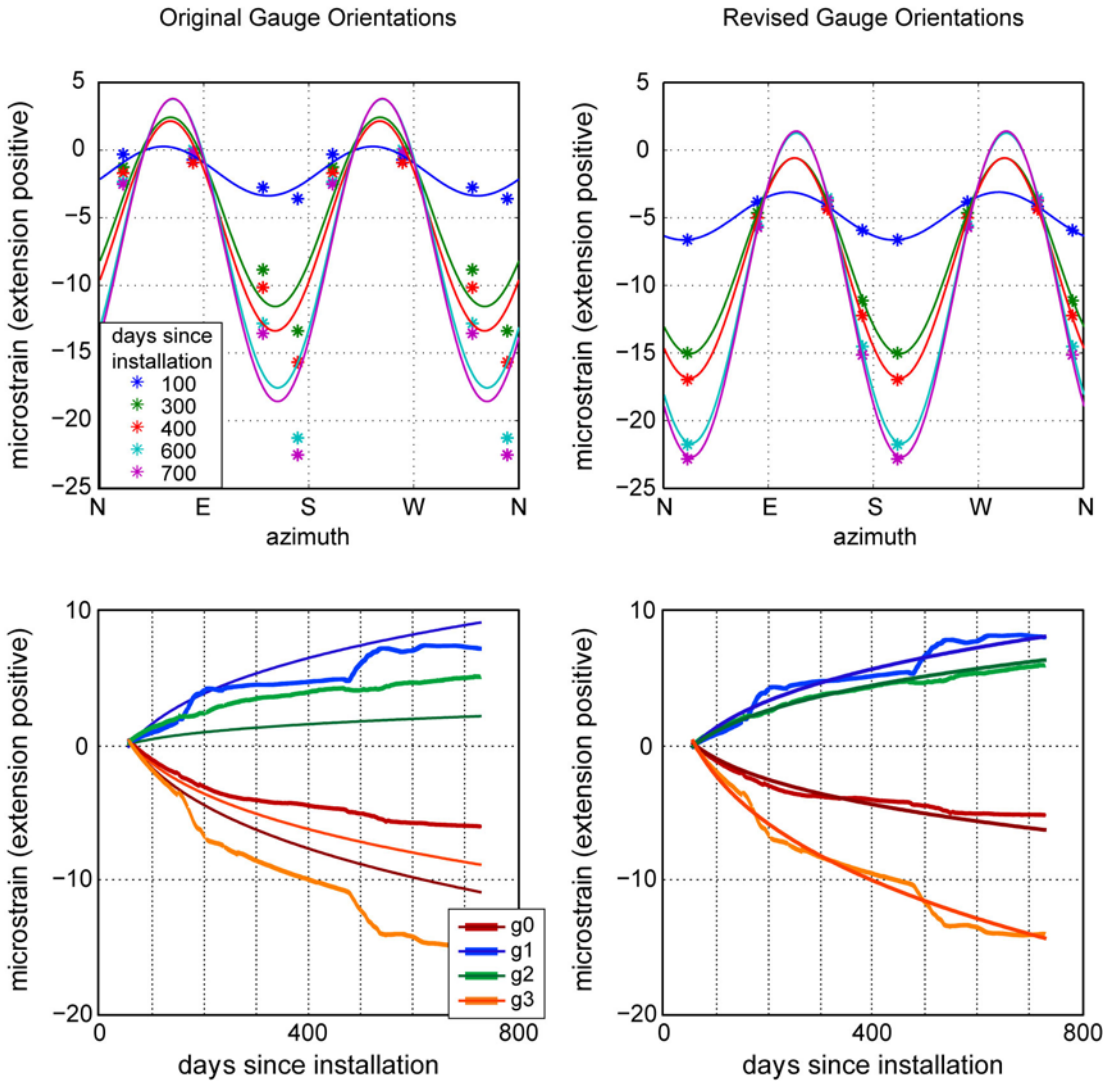

S_{Hmax} Orientation

	150°

	22°

Gauge Orientations

g0	320°
g1	260°
g2	200°
g3	170°

g0	170°
g1	320°
g2	260°
g3	200°

Trend Parameters

A	6.079
b	0.2264
C	15.30

A	5.785
b	0.2522
C	16.11

B009

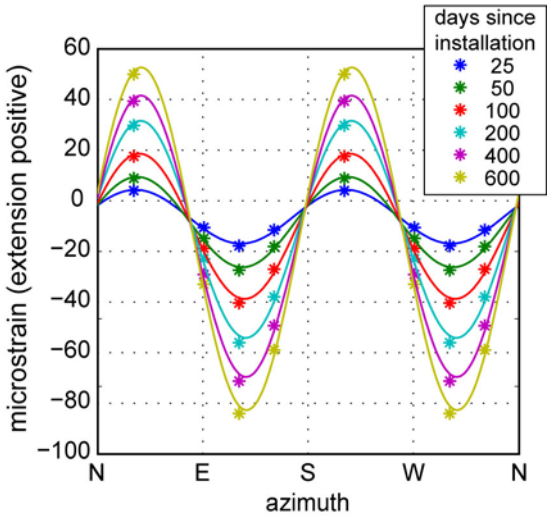

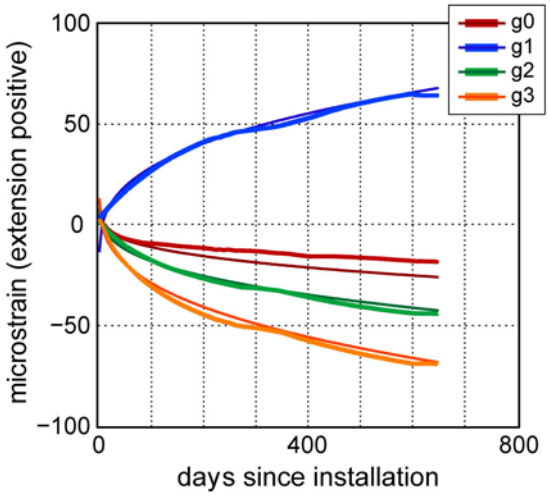

S_{Hmax} Orientation

125°

Gauge Orientations

g0	271°
g1	211°
g2	151°
g3	121°

Trend Parameters

A	10.2
b	0.3296
C	17.45

B011

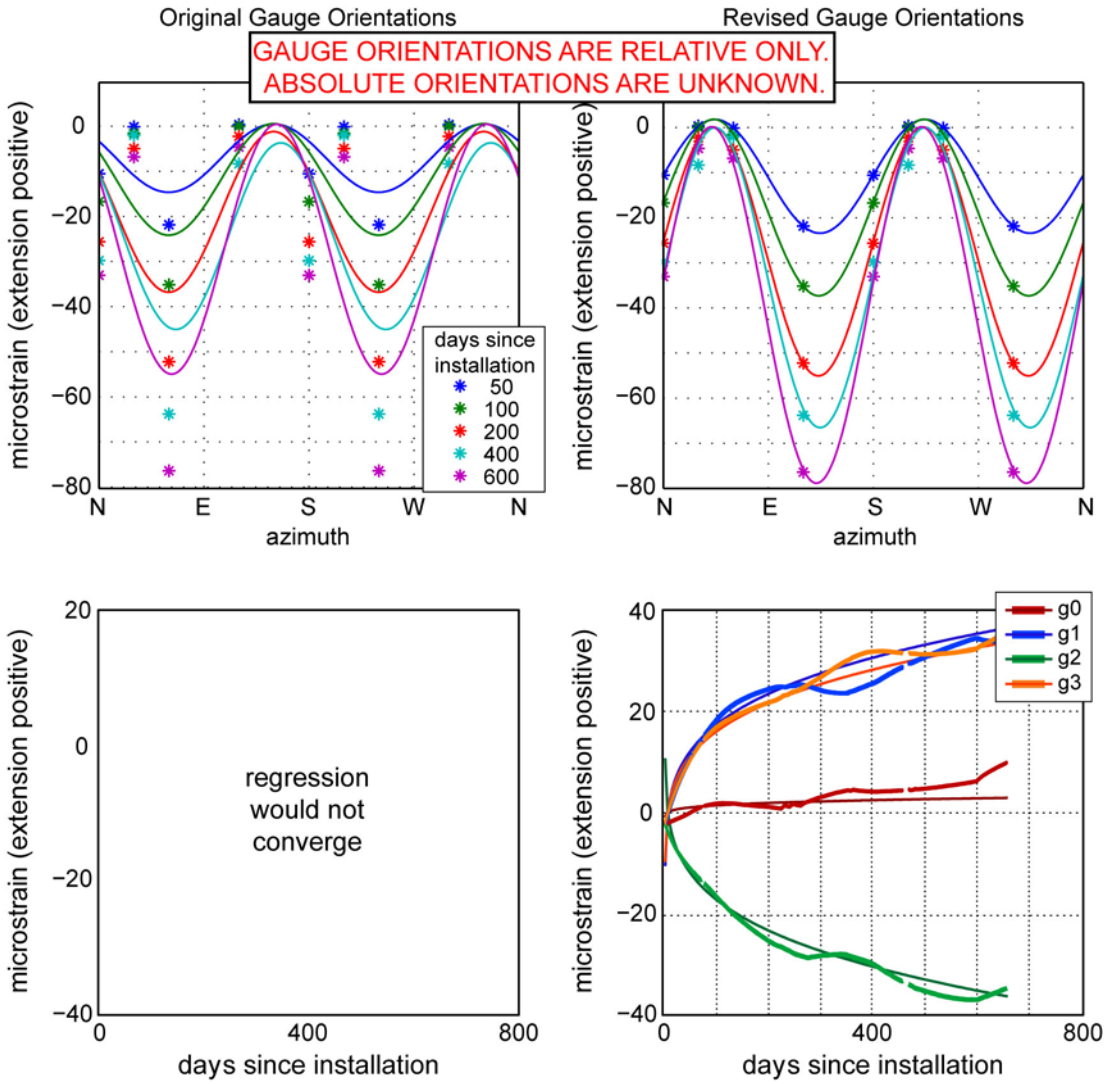

S_{Hmax} Orientation

	Original Gauge Orientations	Revised Gauge Orientations
	n/a	***n/a***

Gauge Orientations

	Original Gauge Orientations	Revised Gauge Orientations
g0	0°	0°
g1	300°	210°
g2	240°	300°
g3	210°	240°

Trend Parameters

	Original Gauge Orientations	Revised Gauge Orientations
	n/a	
A		13.19
b		0.2327
C		19.10

B012

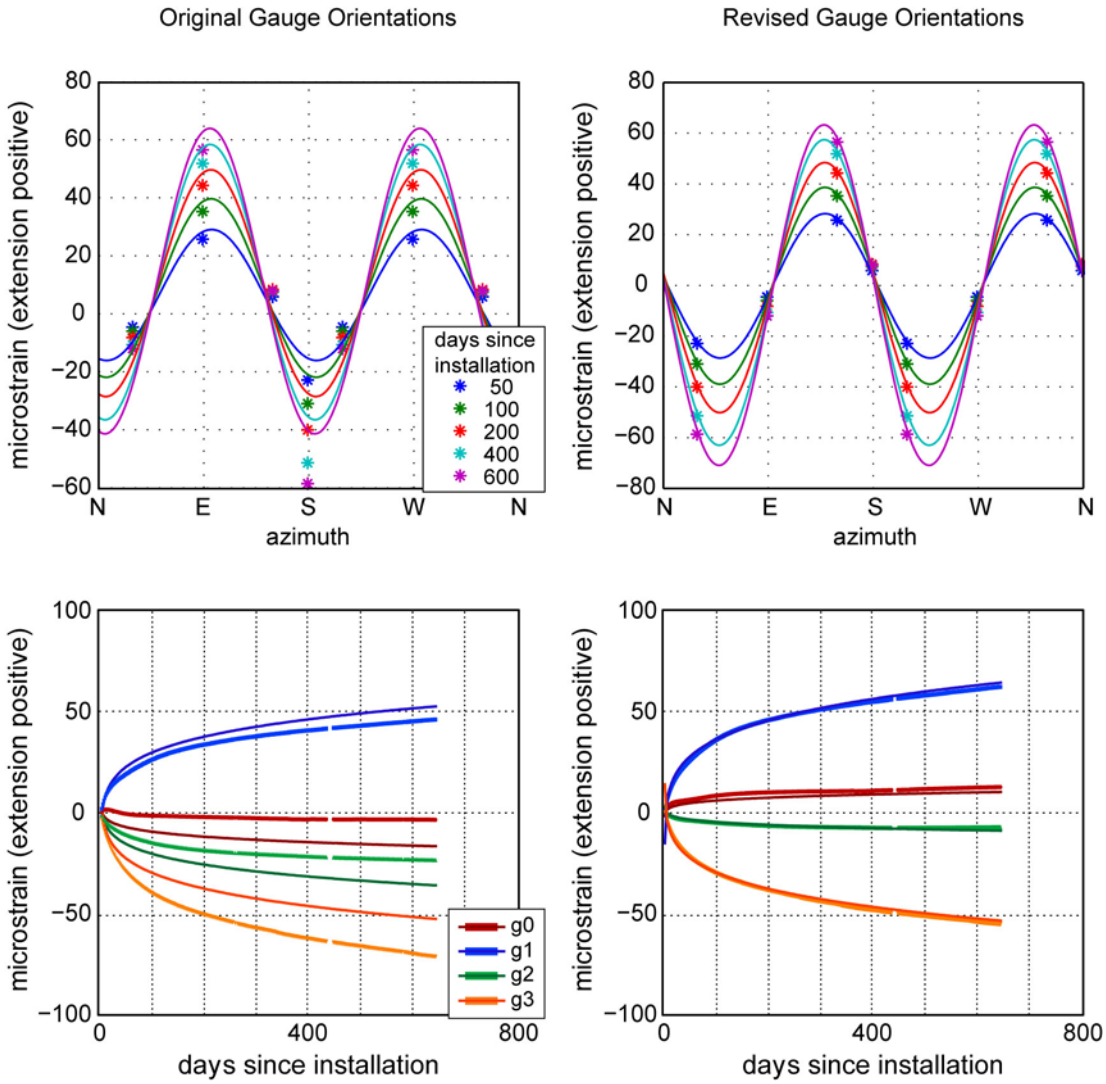

S_{Hmax} Orientation

	Original Gauge Orientations	Revised Gauge Orientations
	6°	48°

Gauge Orientations

	Original Gauge Orientations	Revised Gauge Orientations
g0	329°	179°
g1	269°	329°
g2	209°	269°
g3	179°	209°

Trend Parameters

	Original Gauge Orientations	Revised Gauge Orientations
A	41.64	35.44
b	0.1389	0.1736
C	48.37	40.18

B018

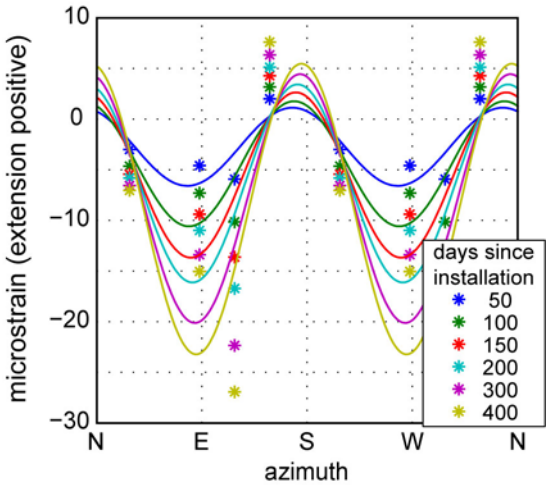

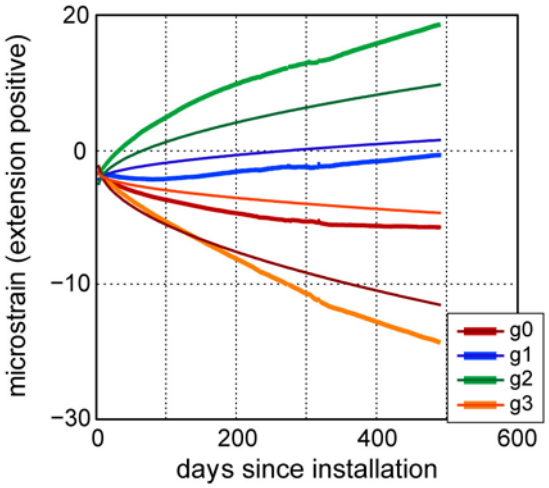

S_{Hmax} Orientation *(poor fit)*

80°

Gauge Orientations

g0	267°
g1	207°
g2	147°
g3	117°

Trend Parameters *(poor fit)*

A	0.6965
b	0.5238
C	1.490

B022

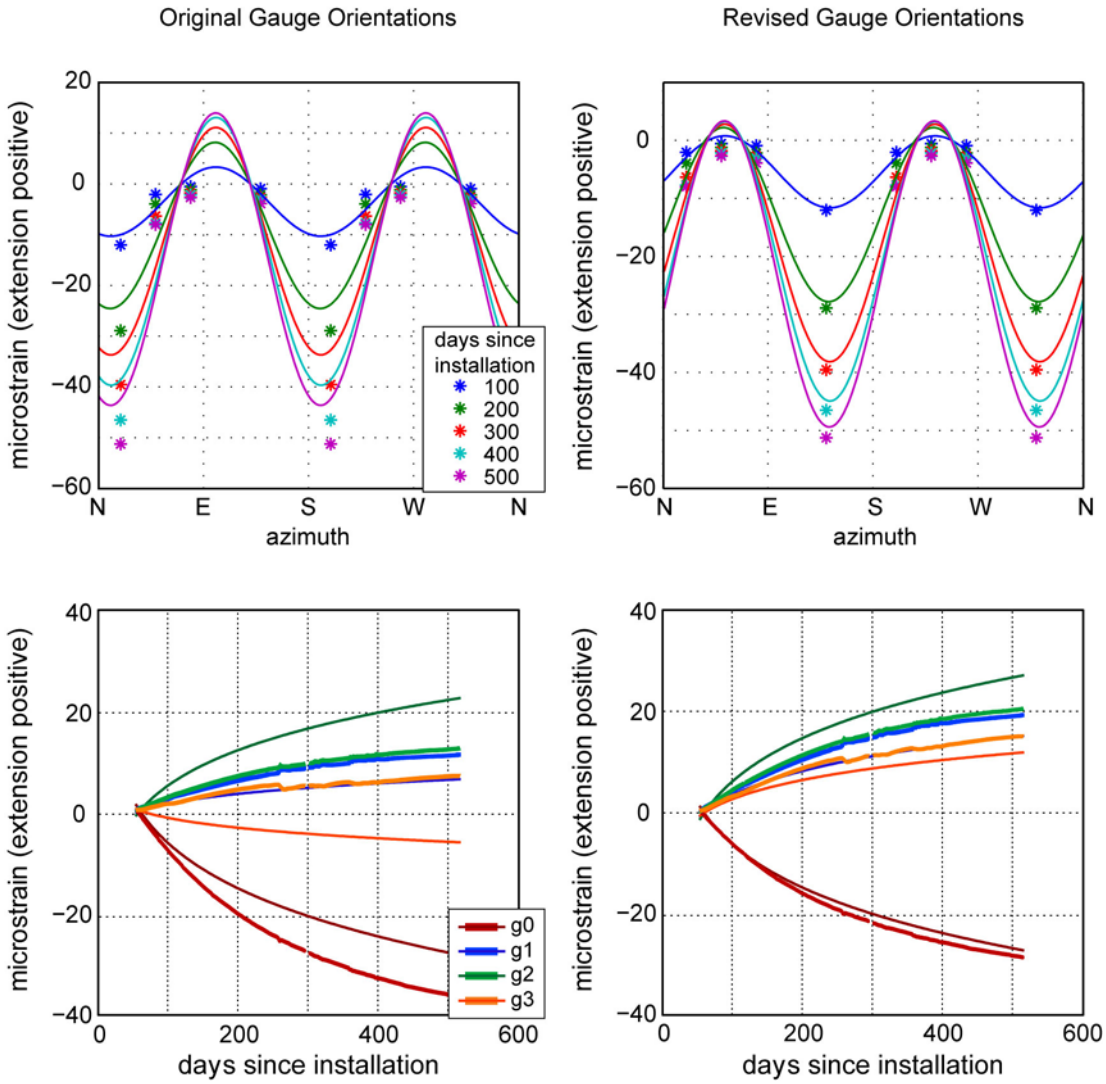

S_{Hmax} Orientation

	10°

	141°

Gauge Orientations

g0	199°
g1	139°
g2	79°
g3	49°

g0	139°
g1	79°
g2	49°
g3	199°

Trend Parameters

A	67.26
b	0.1121
C	105.5

A	82.90
b	0.09207
C	120

B028

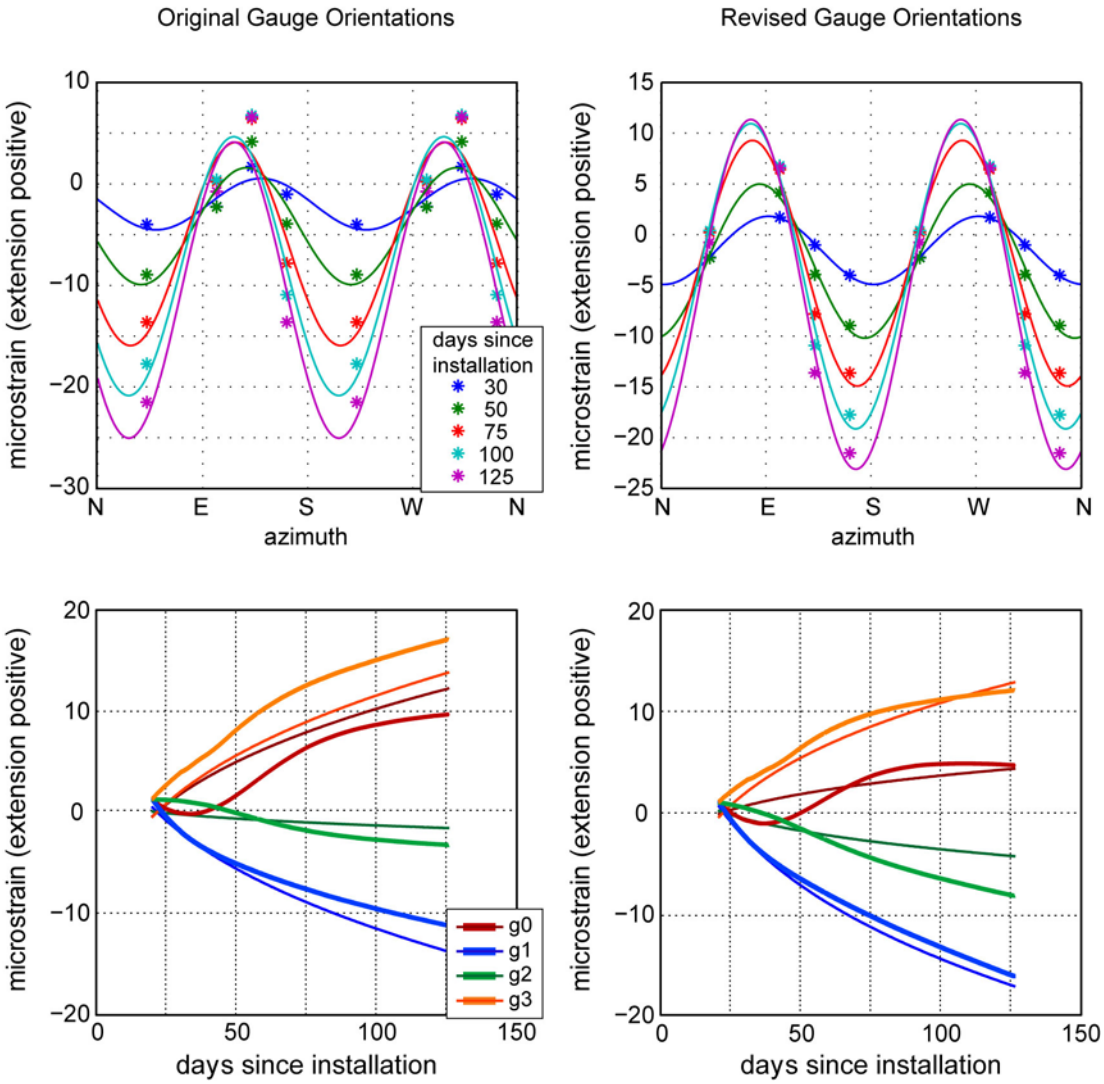

S_{Hmax} Orientation

30°

170°

Gauge Orientations

g0	282°
g1	222°
g2	162°
g3	132°

g0	222°
g1	162°
g2	132°
g3	282°

Trend Parameters

A	7.311
b	0.3224
C	19.71

A	17.86
b	0.2281
C	35.98

B035

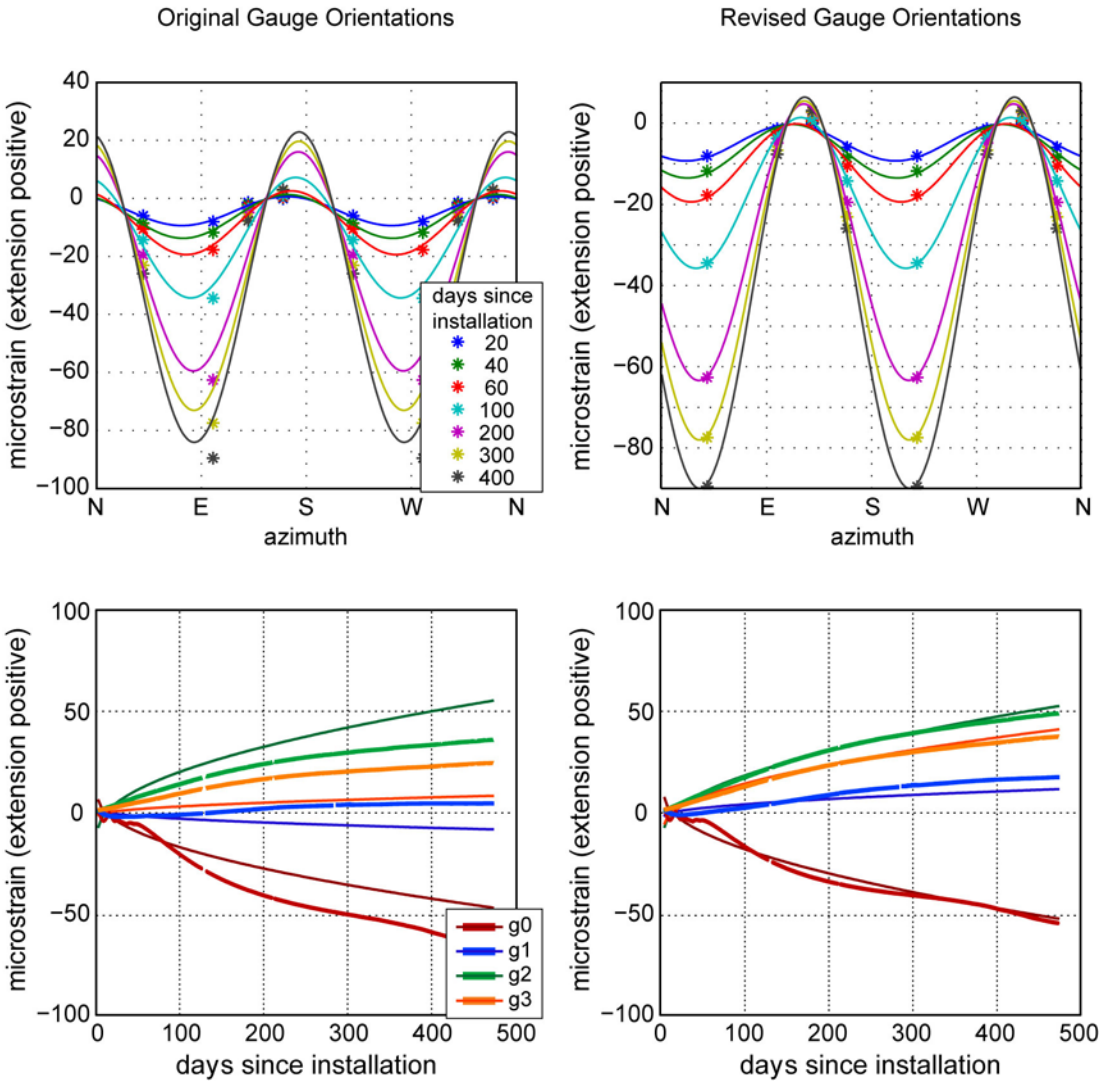

S_{Hmax} Orientation

	80°	30°

Gauge Orientations

g0	279°	219°
g1	219°	159°
g2	159°	129°
g3	129°	279°

Trend Parameters

A	3.037	2.337
b	0.5071	0.5345
C	9.329	7.774

B081

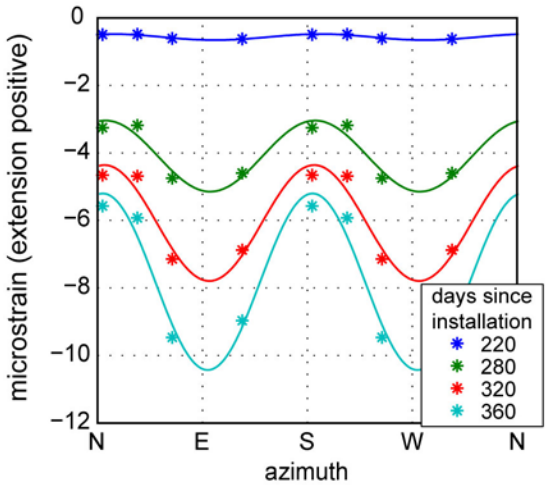

B084

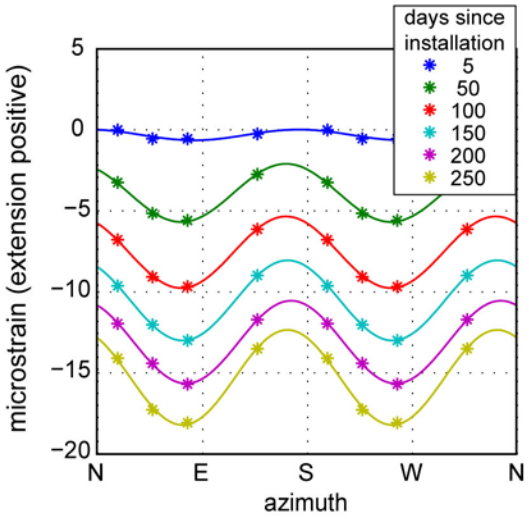

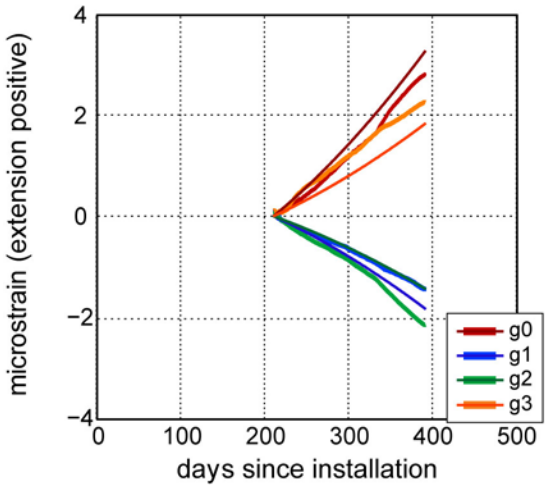

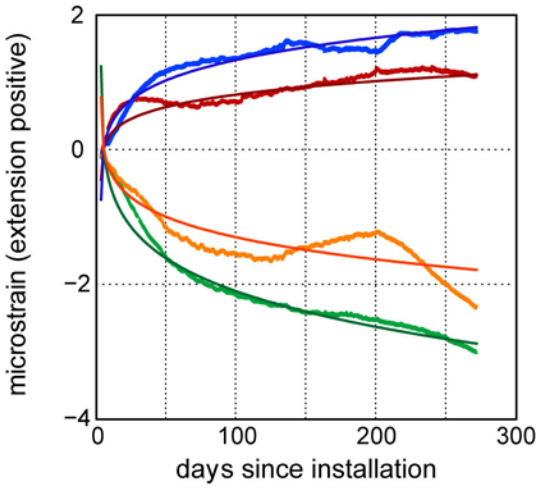

S_{Hmax} Orientation

	95°

	72°

Gauge Orientations

g0	3°
g1	303°
g2	243°
g3	213°

g0	197°
g1	137°
g2	77°
g3	47°

Trend Parameters

A	0.0001194
b	1.777
C	1.621

A	2.554
b	0.1445
C	2.807

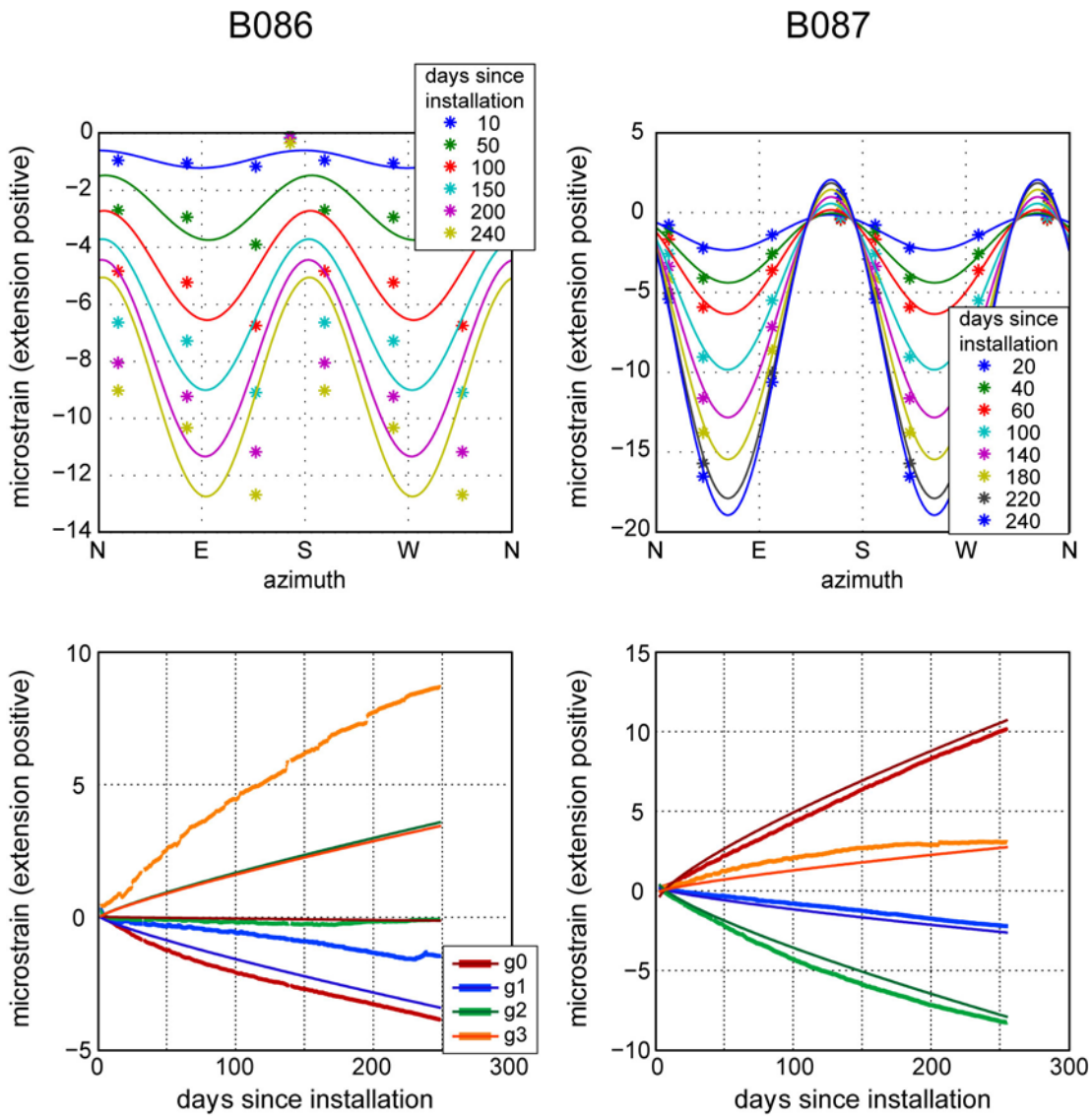

S_{Hmax} Orientation

	B086	B087
	90° (poor fit)	62°

Gauge Orientations

	B086	B087
g0	316°	341°
g1	256°	281°
g2	196°	221°
g3	166°	191°

Trend Parameters *(poor fit in B086)*

	B086	B087
A	.03997	0.1549
b	0.8356	0.7781
C	-0.02290	0.4193

B089

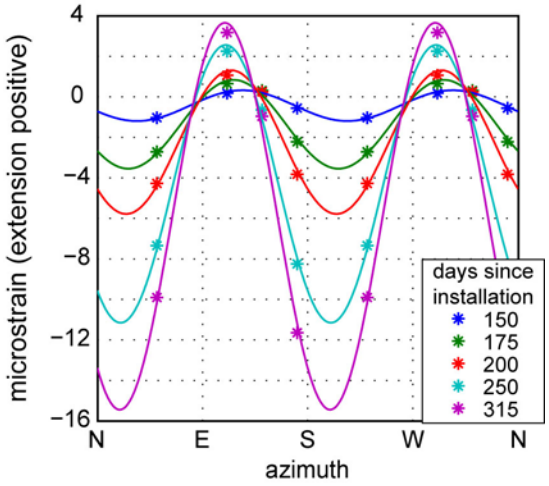

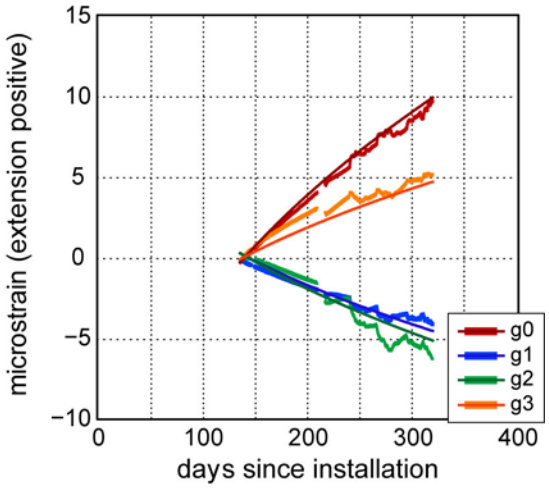

S_{Hmax} Orientation

25°

Gauge Orientations

g0	291°
g1	231°
g2	171°
g3	141°

Trend Parameters

A	3.022
b	0.4183
C	23.91

P403

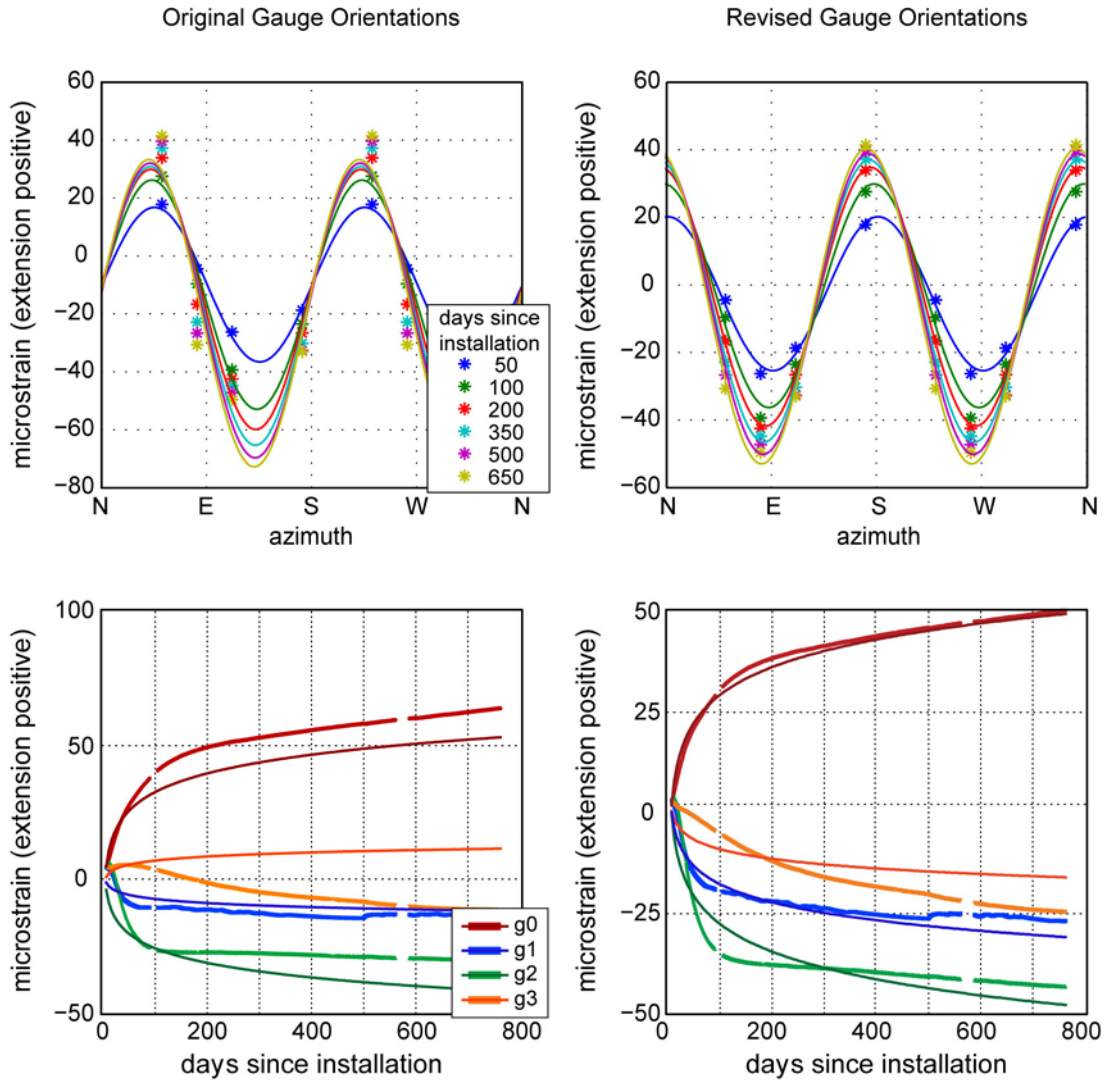

S_{Hmax} Orientation

	132°
	85°

Gauge Orientations

g0	232°
g1	172°
g2	112°
g3	82°

g0	172°
g1	112°
g2	82°
g3	232°

Trend Parameters

A	5543
b	0.001885
C	5557

A	-26690
b	0.0003755
C	716093